Combining Hydrodynamic Modeling with Nonthermal Test Particle Tracking to Improve Flare Simulations

by

Henry deGraffenried Winter III

A dissertation submitted in partial fulfillment
of the requirements for the degree

of

Doctor of Philosophy

in

Physics

MONTANA STATE UNIVERSITY
Bozeman, Montana

April 2009

©COPYRIGHT

by

Henry deGraffenried Winter III

2009

All Rights Reserved

APPROVAL

of a dissertation submitted by

Henry deGraffenried Winter III

This dissertation has been read by each member of the dissertation committee and has been found to be satisfactory regarding content, English usage, format, citations, bibliographic style, and consistency, and is ready for submission to the Division of Graduate Education.

Dr. Petrus C.H. Martens

Approved for the Department of Physics

Dr. Richard J. Smith

Approved for the Division of Graduate Education

Dr. Carl A. Fox

STATEMENT OF PERMISSION TO USE

In presenting this dissertation in partial fulfillment of the requirements for a doctoral degree at Montana State University, I agree that the Library shall make it available to borrowers under rules of the Library. I further agree that copying of this dissertation is allowable only for scholarly purpose, consistent with "fair use" as prescribed in the U.S. Copyright Law. Requests for extensive copying or reproduction of this dissertation should be referred to Bell & Howell Information and Learning, 300 North Zeeb Road, Ann Arbor, Michigan 48106, to whom I have granted "the exclusive right to reproduce and distribute my dissertation in and from microform along with the non-exclusive right to reproduce and distribute my abstract in any format in whole or in part."

Henry deGraffenried Winter III

April 2009

DEDICATION

To my wife Denlyn,

Thank you for tremendous amount of support. I know that you have sacrificed much and for many years so that I could achieve this dream and many others. Yet, through it all, you stayed with me and we worked together to build a life that makes me proud. That is amazing to me, but I've come to expect amazing from you.

To my mother, Dr. Betty Winter,

You showed me that someone could change their life to become the person they wanted to be, at any point in their life. You are a shining example of someone who can switch career paths with grace and dignity. I am sorry I that I did not emulate the grace and dignity part, but that is part of me being the person I want to be.

I could not have done this without you. To you, I dedicate this dissertation.

ACKNOWLEDGMENTS

This work would not have been possible without the support of my advisor, Dr. Petrus Martens. Patience does have some rewards.

The author would also like to thank Dr. David McKenzie. Dr. McKenzie was instrumental in providing the initial computing resources that made the testing of the code possible. Dr. McKenzie also provided time and support that aided the author in the completion of this project. Jeremy Gay and Dr. Ladean McKittrick generously provided additional computing resources that made the completion of this work possible.

A special thanks to Margaret Jarrett. Any student that matriculates through the Physics Graduate Program at Montana State University realizes what a special position she holds. Every physics student has been the recipient of her aid at one time or another, whether they realize it or not. Thank you.

Thanks to Dr. Angela C. Des Jardins. Good friends are hard to find, good office mates are even harder.

This research made extensive use of NASA's Astrophysics Data System and was supported by NASA grant NAG5-12820.

TABLE OF CONTENTS

1. INTRODUCTION TO SOLAR FLARES 1

General Properties. 1
Emission 3
Energy Release 8
Looptop X-ray Sources 12
Research Motivation 18

2. THEORY 20

Equations Describing the Thermal Distribution 21
Thermal Distribution 22
MHD Equations 24
Grids. 27
Spatial 28
Temporal 30
Radiative Losses 32
Corona. 32
Chromosphere and Transition Region 34
Radiative Loss Time Scale. 35
Notes on Radiative Losses. 36
Conduction. 37
Saturated Flux Limitation 38
Conduction Time Scale. 39
Tests. 40
Nonthermal Particle Transport. 41
Stochastic Simulation. 43
Coulomb Scattering 46
Close Collisions 48
Far Collisions 52
Collision Time Scales. 53
Effects of a Nonuniform Magnetic Field. 55
PaTC Time Scales 56
Tests. 57
Emission Calculations. 60

3. STATIC VERSUS DYNAMIC ATMOSPHERES 66

Experimental Setup. 66
Loop Geometry 67

TABLE OF CONTENTS-CONTINUED

Nonthermal Particles 72
Beam Species. 72
Beam Time and Energy Distribution 73
Pitch-Angle Cosine Distribution 76
Error Tests. 78
Grid Spacing Test 78
Monte Carlo Tests 79
The Effect of a Hydrodynamic Plasma on a Nonthermal Particle Beam 81
Effects on HXR emission. 86
Discussion 96
Apparent HXR Source Motions 101

4. THE EFFECTS OF DENSITY GRADIENTS ON NONTHERMAL PARTICLES 109

Experimental Setup. 109
Results. 111
Discussion. 116

5. THE EFFECTS OF DIFFERENT PITCH ANGLE DISTRIBUTIONS 118

Experimental Setup. 118
Thermal Evolution. 118
SXR Signatures. 122
HXR Signatures. 123

6. CONCLUSION 137

Discussion 137
Future Studies. 139
Alfvén Wave Acceleration of Particles 139
Code Improvements 141
Improved Test Particle Sampling 142
CUDA Programming. 144

APPENDICES. 146

APPENDIX A: List of Symbols. 146
APPENDIX B: Numerical Methods 149

REFERENCES. 160

LIST OF TABLES

Table Page

1.1 Mount Wilson sunspot group classification system. Sunspot groups can also be described as a mixture of the above classifications. A complete description is available at http://www.spaceweather.com/glossary/magneticclasses.html. 3

1.2 Solar flare classifications based upon the $1-8$ Å channel of the *GOES* satellites. Each classification is subdivided into 10 subsections (1-10), each with increasing energy. 7

3.1 Initial properties of the post flare loop. 71

4.1 A table showing the properties of the constant cross-section tube. 110

LIST OF FIGURES

Figure Page

1.1 Sample X-ray flare spectrum as observed by the RHESSI satellite. The SXR emission is fitted with a thermal component (green) having a temperature of 16.7 MK. The HXR emission is fitted by power laws, which appear as straight lines on a log-log plot. The power law has breaks, or "knees", at 12 keV and 50 keV. The origin of these breaks is still a matter of scientific debate. The black dashes are observed data points and associated errors (Benz, 2008). 6

1.2 A diagram of a flare from Martens and Kuin (1989). Note the lack of a concentrated looptop emission source. The frequency at which such sources occur was a surprise to theorists and remains largely unexplained. 12

1.3 The famous Masuda flare (Masuda et al., 1994) of 1992 Jan. 13. Hard X-rays are shown in contours and the results from soft X-rays are in color. From left to right, the first two columns show images from the SXT thick aluminum and beryllium filters respectively and the temperature and emission measure derived from their ratio in the last two columns. The rows represent images obtained form HXT in three hard X-ray energy bands: 13.9-22.7 keV, 22.7-32.7 keV, and 32.7-52.7 keV respectively. 16

2.1 A visual representation of the staggered grid system. The energy and electron number densities, ε , ne are defined in N volumes. Other quantities, such as velocity, v, magnetic field strength, B, area, A, and parallel component of acceleration due to gravity, g, are defined on N $-$ 1 surfaces. The first and last volume serve as static boundary conditions for the grids and are not altered by the simulation. 29

2.2 The radiative loss function as used by the MSULOOP code for the current set of experiments. The diamonds represent data points and the line shows interpolated values. 35

2.3 A plot showing the normalized temperature profile for a uniformly heated loop. The red line shows the analytic solution based on (Martens, 2008) and the green dashed line shows the result from MSULOOP. In this simulation saturated flux effects are not taken into account. The percent differences between the numerical and are less than 2%. 42

LIST OF FIGURES-CONTINUED

Figure Page

2.4 A diagram showing the interaction of two particles. The impact parameter, b, is defined as the distance of closest approach between the test and field particle. 47

2.5 A simple diagram showing the relationship between the collision frame and the loop frame. 49

2.6 A plot showing the percent differences in PATC's calculation of the change in a particle's energy in a 0.0001 second time step and an analytic approximation to the energy change. The differences are interpreted as being caused by the numerical treatment's increased accuracy, since it uses fewer approximations than the analytic expression. 58

2.7 A plot showing the ratio of the analytic change in nonthermal particle energy to PATC's calculation of the energy change in a particle's energy in a 0.0001 second time step. 59

2.8 A plot showing the percent differences between an analytical calculation of the magnetic field strength where a test particle should mirror and the numerical calculation. The red, green, and blue lines represents a particle with a pitch-angle cosine of .4, .2, and one respectively. 61

2.9 A diagram representing the calculation of instrument responses on an arbitrarily sized pixel grid. The SHOW_ LOOP software performs a path length integration through the volume emission of a segment of the loop observed by a pixel. This combined with the area of the loop observed by the pixel provides a total signal from a loop of arbitrary inclination angle observed by pixel. Once the signal for the entire grid is computed, the grid can then by convolved with a function to take effects such as point spread functions, or defocus into account. 64

2.10 An image built up using multiple, simulated loops. The image on the far left shows a system of loop strands as would be viewed by the XRT instrument on Hinode in the Al-Poly channel with a 2″ resolution. The center image shows the same system, in the same bandpass but with a 0.5″ resolution. The last image shows the system in a theoretical bandpass for the AIA mission but with an increased resolution of 0.1″ . . . 65

LIST OF FIGURES-CONTINUED

Figure		Page
3.1	A contour map of the magnetic field generated by a Green (1965) style current sheet using the formalisms of Bungey and Priest (1995). Notice the two null points which are regions of zero magnetic field. The characteristic field line for the flare loop geometry is shown at bottom. . .	69
3.2	The field lines calculated by the Green current sheet model. The blue line represents the current sheet in the half plane. The red line illustrates the field line chosen for the basis of the simulated loop's geometry. From this figure it is easy to see why this is called Y-type. The current sheet connects with the separatrix field lines, just above the red line, to form an inverted Y.	70
3.3	A log-log plot of the number of particles as a function of energy. The slope of this corresponds to the electron spectral index δ . A value of δ = 3 was input into the beam generator. The fitted value is shown as $\delta = 2.8$.	75
3.4	A plot of various pitch-angle cosine distribution functions, f (μPA), corresponding to $\gamma_{PA} = -5, -3, 0, 3, 5$. A pitch-angle cosine of 1 (−1) corresponds to the nonthermal particle's momentum being directed parallel (anti-parallel) to the loop axis. A pitch-angle cosine of zero corresponds to the nonthermal particle's momentum being directed perpendicular to the loop axis.	77
3.5	A plot of the pitch-angle cosine distribution to be used in the current experiment with $\gamma_{PA} = -4$.	78
3.6	A graph showing the percent difference between the test variables, temperature and density, at a given number of grid cells in comparison to a simulation run with 1400 grid cells. This still was taken at the beginning of the simulation.	79
3.7	Same as 3.6 but taken after 5 second s of simulated time.	80
3.8	Same as figures 3.17 and 3.7 but at 300 second s. By analyzing plots such as this for every time step it becomes apparent that increasing the number of grid cells past 700 only yields minor improvements in accuracy.	80

LIST OF FIGURES-CONTINUED

Figure		Page
3.9	This plot shows how the average of the apex density and temperature and the associated standard deviation changes as a function of the number of runs five second s into the simulation, ...	82
3.10	The same as 3.9 but 10 second s into the simulation.	82
3.11	The same as 3.9 and 3.10 but 300 second s into the simulation.	83
3.12	A plot showing how the percent standard deviation for temperature and density changes as a function of time for five runs.	83
3.13	A plot showing how the percent standard deviation for temperature and density changes as a function of time for eight runs.	84
3.14	A plot showing how the percent standard deviation for temperature and density changes as a function of time for 12 runs.	84
3.15	A plot showing how the relative standard deviation for temperature changes as a function of time.	85
3.16	A plot showing how the percent standard deviation for 3 − 6 keV and 12 − 25 kev emission as a function of time.	85
3.17	Hard X-ray emission in the 3 − 6 keV passband for a dynamic atmosphere simulation. The top row shows emission simulated in an instrument with 7″ pixels and a Gaussian point spread function with a FWHM of 3 pixels. The first column shows the total emission, the second shows the nonthermal component only, and the last column shows the thermal component only. The lower row shows the light curve of the total (black), nonthermal (green) and thermal (red) emission in the box defining the loop apex. Images are binned in 4 second increments. Contours enclose the 40%, 60%, and 80% levels.	88
3.18	Same as figure 3.17 but from 4 − 8 second time bin.	89
3.19	Same as figure 3.17 but from 296 − 300 second time bin.	90

LIST OF FIGURES-CONTINUED

Figure Page

3.20 Hard X-ray emission in the 3 − 6 keV passband for a static atmosphere simulation. This plot shows emission in the 0 − 4 second time bin. 91

3.21 Hard X-ray emission in the 3 − 6 keV passband for a static atmosphere simulation in the 4 − 8 second time bin. 92

3.22 Hard X-ray emission in the 3 − 6 keV passband for a static atmosphere simulation in the 0 − 4 second time bin. 93

3.23 A comparison of the Monte Carlo estimator value of the apex hard X-ray emission in the 3 − 6 keV passband in a dynamic (red) and static (blue) atmosphere. Error bars show the +/ − s_{N-1} value. 94

3.24 Same as figure 3.23 but plotted on a log scale. Error bars have been removed for clarity. 95

3.25 Distributions of sampled data with the dynamic case in red and the static case in blue. The means of the distribution, which comprise the value for the Monte Carlo estimator, are over plotted as a dashed line. Flux units are arbitrary. 95

3.26 Kolmogorov-Smirnov test of the differences hard X-ray emission in the 3 − 6 keV bandpass in the dynamic and static atmosphere simulations. The red line maps the evolution of the D statistic as a function of time. The blue lines shows the confidence level with which the null hypothesis can be rejected. This provides strong, quantitative evidence that the evolution of the nonthermal beam is significantly statistically different in the dynamic atmosphere than in the static atmosphere. 97

3.27 Plots of the pressure, density, average velocity, and temperature as a function of loop coordinate. This plot is at the beginning of the simulation. 99

3.28 Same as figure 3.27 but after four seconds of simulated time. 100

3.29 State variables plotted after 125 seconds of simulated time. 100

3.30 Plots of the state variables at 300 seconds. 101

LIST OF FIGURES-CONTINUED

Figure Page

3.31 A plot of the density at four seconds of simulated time. Red represents the dynamic atmosphere and blue represents the static atmosphere, which is the same as the dynamic atmosphere at t = 0 seconds. 102

3.32 A plot of the density at 15 seconds of simulated time. 103

3.33 A plot comparing the static and dynamic atmosphere density at 125 seconds. 103

3.34 Density plot at 300 seconds. 104

3.35 The initial pitch-angle cosine distribution for the dynamic atmosphere simulation. 104

3.36 The pitch-angle cosine distribution for the dynamic atmosphere after four seconds of simulated time. Note that at this time the beam pitch-angle cosine distribution is closer to a Gaussian centered around zero. Particles with large absolute values of pitch-angle cosine have already lost all of their energy in the denser loop legs. 105

3.37 The pitch-angle distribution for the dynamic atmosphere after 30 seconds of simulated time. Note that the distribution of pitch-angle cosines is steeply peaked around zero. Particles that are at the loop apex, with such a small pitch-angle cosine will scatter less due to the low density of the loop apex. With less scattering, and a pitch-angles near zero, any particle near the apex will now be effectively trapped there. 106

4.1 A plot showing the density profiles of the tubes used in this experiment. . 110

4.2 A plot showing the initial pitch-angle cosine distributions of the nonthermal particle beams injected into the center of the tube. The quantity I_{PA} is defined as the number of particles with a pitch-angle cosine between the two blue dotted lines, in the central portion of the distribution. 111

4.3 A plot showing the median values of the inner pitch-angle ratio, I_{PA}/N . Error bars were taken using a bootstrap with replacement method and represent the 95% confidence level. A completely uniform distribution would have a $\{I_{pos}/N\}$ med = 0.5. 113

LIST OF FIGURES-CONTINUED

Figure		Page
4.4	This plot shows the median values inner position ratio, I_{pos}/N, for each value of the density gradient factor as a function of time.	113
4.5	This plot is the same as figure 4.4 but zoomed in at $2 \leq t \leq 6$	114
4.6	A plot showing the nonthermal beam alive times as a function of gradient factor averaged over the ten runs.	115
4.7	A plot showing the skew of the distribution of alive times for all runs.	116
5.1	A plot showing pitch-angle cosine distributions for the three simulations to be conducted.	119
5.2	This plot shows the mean apex temperature, in kelvins, of a flaring loop for each simulation. The $\gamma_{PA} = 4$ case became almost three times as hot as the $\gamma_{PA} = -4$ case. The error bars denote one standard deviation.	120
5.3	This plot shows the mean radiative loss rates, as a function of time, for each of the simulated cases. The error bars denote one standard deviation.	121
5.4	This plot shows the mean apex thermal electron density for each simulation. The maximum density enhancement of the $\gamma_{PA} = 4$ came nearly a minute before the $\gamma_{PA} = -4$ case.	122
5.5	This plot shows the emission in XRT filter channels for the $\gamma_{PA} = -4$ pitch-angle cosine distribution case. The plot at the bottom of the figure the apex to footpoint emission ratio for each case as a function of time.	124
5.6	This plot shows the emission in XRT filter channels for the $\gamma_{PA} = 0$ pitch-angle cosine distribution case. The plot at the bottom of the figure the apex to footpoint emission ratio for each case as a function of time.	125
5.7	This plot shows the emission in XRT filter channels for the $\gamma_{PA} = 4$ pitch-angle cosine distribution case. The plot at the bottom of the figure the apex to footpoint emission ratio for each case as a function of time. NB This was the only case that showed an initial peak in apex to footpoint emission ratio.	126

LIST OF FIGURES-CONTINUED

Figure Page

5.8 This plot shows the apex to footpoint emission ratio for each filter channels. While the ratios differed slightly in magnitude from filter to filter, the obvious signal was the time profile of the ratio. 127

5.9 This plot shows the HXR emission for the $\gamma_{PA} = 0$ case in the t = 0 − 4 time bin. The bottom plot shows the total apex emission as defined by the bounding box as a function of time with the nonthermal signal in green, the thermal signal in red, and the total signal in black. 128

5.10 This plot shows the HXR emission for the $\gamma_{PA} = 0$ case in the t = 4 − 8 time bin. 129

5.11 This plot shows the HXR emission for the $\gamma_{PA} = 0$ case in the t = 52 - 56 time bin. 130

5.12 This plot shows the HXR emission for the $\gamma_{PA} = 0$ case in the t = 296 − 300 time bin. 131

5.13 This plot shows the HXR emission for the $\gamma_{PA} = 4$ case in the t = 0 − 4 time bin. 132

5.14 This plot shows the HXR emission for the $\gamma_{PA} = 4$ case in the t = 4 − 8 time bin. 133

5.15 This plot shows the HXR emission for the $\gamma_{PA} = 4$ case in the t = 40 − 44 time bin. 134

5.16 This plot shows the HXR emission for the $\gamma_{PA} = 4$ case in the t = 296 − 300 time bin. 134

6.1 This plot illustrates how the use of Sobol numbers can increase the fractional accuracy the Monte Carlo calculation of pi while using fewer pairs of random numbers. The upper dashed line represents $N^{-1/2}$ while the lower dashed line represents N^{-1}. The blue line charts the fractional accuracy as a function of number of uniformly distributed random pairs, which matches the $N^{-1/2}$ line well. The black solid line is the fractional accuracy as a function of number of Sobol pairs. While the Sobol pairs do not exactly track the N^{-1} trend they do show an orders of magnitude improvement over uniform pairs. 143

CONVENTIONS

In this work modified Gaussian units (mgu) are used. This system of units may not be familiar to scientists in other fields who commonly use the International System of Units (SI). The mgu unit system uses centimeters, grams and seconds for non-electromagnetic quantities, electrostatic units (esu) for electrical quantities and electromagnetic units for magnetic quantities (*Sturrock*, 1994). Despite the adoption of SI in most fields of science, mgu remains the most widely used system in plasma physics (*Benz*, 1993b). The mgu unit of energy is the *erg*. In all formulae dealing with the rate of change of the energy, this unit is assumed. However, due to historical reasons, the unit of energy most often used by high energy astronomers is the *electron-volt* (eV) and particle kinetic energies and photon energies are expressed in kilo-electron-volts (keV) or mega-electron-volts (meV). Temperatures are always expressed in kelvins in this work, though many other plasma physics and kinetics texts express temperatures in terms of eV as well.

There is much confusion regarding the precise definition of the kurtosis of a distribution in current literature. Properties of distributions are normally described by taking successive moments. In older and some current texts, the kurtosis is defined as the fourth moment of the distribution. However, some newer texts now label the kurtosis as being the fourth moment minus three, the kurtosis for a normal distribution. This quantity used to be known as the kurtosis excess. However, this work uses fourth moment minus three for the definition of the kurtosis, since this seems to be the modern, if not more confusing, standard.

This work deals heavily in the construction and use of software routines to simulate physical process. Individual routine names are italicized, E.g. *get_loop_mfp.pro*, and software suites containing many subroutines are written in an all capital notation, E.g. PATC.

ABSTRACT

Solar flares remain a subject of intense study in the solar physics community. These huge releases of energy on the Sun have direct consequences for humans on Earth and in space. The processes that impart tremendous amounts of energy are not well understood. In order to test theoretical models of flare formation and evolution, state of the art, numerical codes must be created that can accurately simulate the wide range of electromagnetic radiation emitted by flares. A direct comparison of simulated radiation to increasingly detailed observations will allow scientists to test the validity of theoretical models. To accomplish this task, numerical codes were developed that can simulate both the thermal and nonthermal components of a flaring plasma, their interactions, and their emissions. The HYLOOP code combines a hydrodynamic equation solver with a nonthermal particle tracking code in order to simulate the thermal and nonthermal aspects of a flare. A solar flare was simulated using this new code with a static atmosphere and with a dynamic atmosphere, to illustrate the importance of considering hydrodynamic effects on nonthermal beam evolution. The importance of density gradients in the evolution of nonthermal electron beams was investigated by studying their effects in isolation. The importance of the initial pitch-angle cosine distribution to flare dynamics was investigated. Emission in XRT filters were calculated and analyzed to see if there were soft X-ray signatures that could give clues to the nonthermal particle distributions. Finally the HXR source motions that appeared in the simulations were compared to real observations of this phenomena.

CHAPTER 1

INTRODUCTION TO SOLAR FLARES

The study of the Sun has a long and rich history, from ancient notions that it was a hot ball of iron, to utilizing it as a research laboratory in order to solve basic questions of particle physics. The interested reader is directed to *Phillips* (1995) and *Zirker* (2002) for in-depth and fascinating accounts of solar studies. Despite centuries of study and over 40 years of intense scrutiny by satellite observatories, there is still much about the Sun that is not understood. In particular, solar flares, the most powerful explosions in our solar system, remain a mysterious phenomenon. A basic overview of solar flares is provided to aid in the understanding the work as a whole.

General Properties

On September 1, 1859, Richard Carrington and R. Hodgson observed an intense brightening in the visible light emission of the Sun. This was the first recorded observation of a solar flare (*Phillips*, 1995). This was a serendipitous observation since such *white light flares* are actually quite rare with only 60 being recorded from Carrington's initial observation to 1992 (*Phillips*, 1995). Even though the Sun emits primarily in the visible wavelengths, flares typically do not. Only a fraction of the emitted energy of a flare, about 25% or so, is emitted in the visible spectrum and usually is insignificant when compared to the photospheric background (*Phillips*, 1995). Little did Carrington and Hodgson know that they had witnessed one of the largest releases of energy in the solar system.

Later measurements showed that flares could release energy up to $10^{33}\,ergs$ in time scales of tens of seconds to minutes. While this is a small amount compared to the Sun's

total luminous output, $\mathscr{L}_\odot \simeq 3.83 \times 10^{33}\, erg\, sec^{-1}$, it still easily dwarfs that of thermonuclear weapons[1] or even that of the Shoemaker-Levi 9 comet's impact with Jupiter (*Ivlev et al.*, 1995)![2] It is easy to see why the understanding of solar flares is not only of importance to solar theorists but has practical applications as well. The field of *Space Weather* studies how flares and other solar phenomena affect the Earth's local environment. Some of these effects can influence life on Earth directly. Flares are often associated with massive clouds of plasma, with their own magnetic fields, called *Coronal Mass Ejections* (CMEs). Massive rearrangements of the Earth's magnetic field can occur if the magnetic field of a CME is aligned opposite to the Earth's magnetic field (*Zirker*, 2002). This rearrangement generates electrical currents in sensitive electronics or in long wires and pipelines. In 1989 a magnetic disturbance caused a power blackout in Quebec that affected millions (*Odenwald*, 1999). Communication blackouts are also common during these "magnetic storms". In 1984 Air Force One lost communications with the United States as President Reagan flew to China (*Hilts*, 1988). Understanding flares is even more important now that low Earth orbit is "permanently" inhabited. During solar flares astronauts can be exposed to high levels of ionizing radiation that can cause long-term illnesses, such as an increased risk for cancer, or even death. A solar storm in 1990 gave *Mir* cosmonauts a year's radiation dosage in just a few days (*Odenwald*, 1999). Due to the relativistic speed of these particles there is very little warning time before the damage is done.

Flares can occur over many different spatial scales including, theoretically, those too small to detect with current instrumentation. A very large flare can cover an area up to 3×10^9 square kilometers or 1% of the visible solar surface (*Phillips*, 1995). The location of solar flares, however, is not uniformly distributed across the solar disk. Ninety percent

[1] A *Megatonne* equivalent of TNT has an energy output of $\sim 4.2 \times 10^{23}\, ergs$ (*Thompson and Taylor*, 2008). The largest fusion warhead developed by the United States of America, the B-41, had an estimated yield of 25 *Megatonnes* (*Sublette*, 2007). If true, then it would take 10^7 weapons of this type to release the same energy of an X class solar flare.

[2] The largest fragment of the Shoemaker-Levy 9 comet was estimated to have a kinetic energy of $10^{30}\, erg$.

Table 1.1: Mount Wilson sunspot group classification system. Sunspot groups can also be described as a mixture of the above classifications. A complete description is available at http://www.spaceweather.com/glossary/magneticclasses.html.

Type	Description
α	Unipolar sunspot group
β	A sunspot group having distinct positive and negative magnetic polarities
γ	A complex active region with irregular grouping of positive and negative polarities
δ	A qualifier to the other sunspot groups that indicates that the umbrae of sunspots of different polarities are separated by less than 2 degrees within one penumbra have opposite polarity

of flares occur in *active regions* (*Strong et al.*, 1999). In the *corona*, the hot, tenuous, outer solar atmosphere, active regions are areas that contain large loop structures emitting in the extreme ultraviolet and X-ray portions of the electromagnetic spectrum. In the solar photosphere, the visible surface of the Sun, these active regions are associated with dark sunspot groups (*Zirker*, 2002). These sunspot regions are areas of intense magnetic fields with strengths of about 4×10^3 *Gauss* on average (*Phillips*, 1995). Sunspot groups can have many different configurations. The configurations most associated with flares are $\beta\gamma$ sunspot regions as defined by the Mount Wilson Classification system (Phillips, 1992). In this classification scheme, a $\beta\gamma$ region is defined as a region of bipolar positive and negative magnetic field with irregular groupings of flux that give rise to complex magnetic field configurations (see table 1). This association of flares with regions of strong and complex magnetic fields gives strong clues about the origin of these events. The Sun has shown a surprisingly regular, 11 year cycle of magnetic activity (*Phillips*, 1995) which also correlates well to flare activity. At the peak of solar magnetic activity, the lower solar latitudes have high occurrences of sunspots and flares are more frequent (*Zirker*, 2002).

Emission

The exact definition of hard X-rays (HXR) tends to vary slightly depending upon the bandpasses of a particular instrument but are usually defined as photons having energies of $10\,keV$ to $120\,keV$ ($1.03 \times 10^{-1} \leq \lambda \leq 1.24$ Å). HXR emission is strongly associated with the impulsive onset of solar flares. HXR events are usually impulsive, short-lived events with fluctuations on the order of 0.02 seconds and lifetimes on the order of minutes. Some, very rare, features have started as soft X-ray sources and increased steadily in energy to become HXR features. These events can have lifetimes on the order of hours. If the emissions from the more commonly seen impulsive HXR flare events are from thermal electrons that would imply a plasma temperature on the order of $10^9\,K$ (*Phillips*, 1995). However, high-energy, nonthermal electrons being deflected by slow protons in a free-free, *Bremsstrahlung* radiation mechanism can also explain the emission and many theories of flare evolution predict the emission of nonthermal electron beams (*Zirker*, 2002). While newer instruments have aided in determining whether HXR emission is thermal or nonthermal, many events remain hard to interpret.

The HXR spectra of flares tend to be dominated by power law distributions in photon energy (*Benz*, 2008) expressed as

$$I\left(\varepsilon_\gamma\right) = a\varepsilon_\gamma^{-\gamma_p}, \tag{1.1}$$

where $I\left(\varepsilon_\gamma\right)$ is the HXR Bremsstrahlung flux $\left(photons\,cm^{-2}\,s^{-1}\,keV^{-1}\right)$, a is a constant, ε_γ is the photon energy and γ_p is the photon spectral index. Such distributions are described as having a *hard spectrum* if γ_p is small $(\gamma_p \lesssim 4)$ and having a *soft spectrum* if γ_p is large $(\gamma_p \gtrsim 5)$. *Brown* (1971) showed that one could infer a power law distribution of the injected electron energy spectrum from the HXR photon spectrum. The power law distribution of

the electron energies is expressed by

$$F = F_0 E^{-\delta_E}, \tag{1.2}$$

where F is in units of $electrons\,cm^{-2}\,s^{-1}\,keV^{-1}$ and δ_E is the electron energy spectral index. In the simplified case this relationship takes two simple forms; $\gamma_p = \delta_E + 1$ when the observation time is much shorter than the energy loss time of the electrons or a *thin-target* model, and $\gamma_p = \delta_E - 1$ for a *thick-target* model where the nonthermal particle loses enough energy to become thermalized (*Brown*, 1971; *Tandberg-Hanssen and Emslie*, 1988). The observations of a power law distribution in emitted HXR photon energy in flares strongly suggest the presence of a nonthermal distribution of electrons. However, it should be noted that this simplistic relationship has recently come under increased scrutiny and may not hold to be true under more rigorous analysis (*Brown et al.*, 2007). Determining the true distributions of the nonthermal particles and the mechanisms responsible for their acceleration is a matter of intense research.

Flare regions emit strongly in soft X-rays (SXR), photons having energies between 0.1 and $10\,keV$ ($1.24 \leq \lambda \leq 124$ Å), after their initial impulsive onset. Solar soft X-rays consist of both continuum and spectral soft X-ray emission produced by thermal plasma and possibly a difficult to detect nonthermal component. Measurements of SXR spectral lines by the Bent Crystal Spectrometer (BCS*)* on board the *Solar Maximum Mission* (*SMM*) show flare plasma can have temperatures up to $2 \times 10^7\,K$ (*Strong et al.*, 1999). An interesting fact discovered by SXR observations is that cooler plasma with temperatures of $\sim 2 \times 10^6\,K$ can be observed in a flare region co-existing with the hotter plasma. The only way that this can be possible is if the two plasmas are contained within separate magnetic field flux tubes. This means that some flaring regions consist of several loop features at different characteristic temperatures (*Phillips*, 1995).

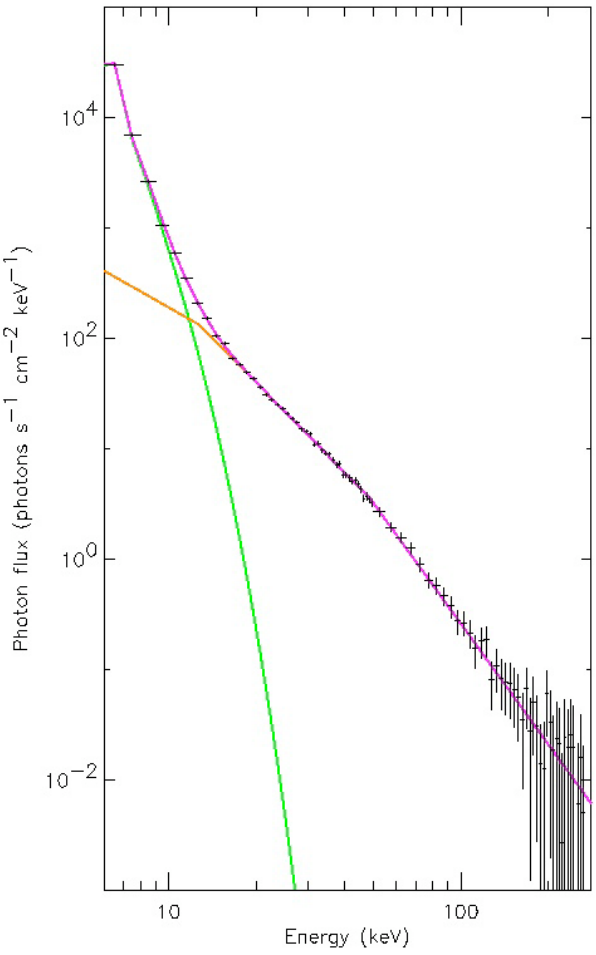

Figure 1.1: Sample X-ray flare spectrum as observed by the *RHESSI* satellite. The SXR emission is fitted with a thermal component (green) having a temperature of 16.7 MK. The HXR emission is fitted by power laws, which appear as straight lines on a log-log plot. The power law has breaks, or "knees", at 12 keV and 50 keV. The origin of these breaks is still a matter of scientific debate. The black dashes are observed data points and associated errors (*Benz*, 2008).

Table 1.2: Solar flare classifications based upon the $1-8$ Å channel of the *GOES* satellites. Each classification is subdivided into 10 subsections (1-10), each with increasing energy.

Class	Flux range measured in $W\,m^{-2}$	Description
B	$F \leq 10^{-6}$	Common during times of high magnetic activity
C	$10^{-6} \leq F \leq 10^{-5}$	Few noticeable effects at Earth
M	$10^{-5} \leq F \leq 10^{-4}$	Can cause radio blackouts in the polar regions and aurora
X	$F \geq 10^{-4}$	Can cause world-wide blackouts, major magnetic storms and aurorae, major threat to astronauts

The strength of a flare's SXR emission provides an important measure of the flare strength and the potential impact it can have on the Earth-space environment. For this reason the current flare classification system is based on the intensity of the flare between $1-8$ Å. This system was established by the National Oceanic and Atmospheric Administration (NOAA), which is charged with monitoring the Earth-space environment by the U.S. government. X-ray flux is measured by a series of *Geostationary Operational Environmental Satellites* (*GOES*) and flares are given a rating of B, C, M, or X with X flares producing the most powerful emission (see table 1 for details). The data from the *GOES* satellites are freely available on the Internet[3].

Very intense flares can produce *gamma rays* whose energies are measured in mega-electron volts (MeV) . These high energy photons were first detected by balloon borne instrumentation and later studied more in-depth by the Gamma Ray Spectrometer (GRS) on board the *SMM* satellite (*Strong et al.*, 1999). Many different gamma ray spectral lines were detected, each with different causes. A line at 2.2 MeV is produced when high-energy free neutrons, formed from proton collisions, are slowed down by further collisional

[3]Data can be obtained from NOAA's Space Weather Prediction Center (http://www.swpc.noaa.gov/) or from N3KL.ORG (http://www.n3kl.org/sun/noaa.html).

process until they are captured by a proton to produce an alpha particle. Particles in flares are raised to such high energies that proton collisions with a nucleus can raise the nucleus' energy state. A strong line at 4.4 MeV is produced by the de-excitation of carbon nuclei that were excited by the above process. Another strong line is observed in flares at 0.511 MeV. This line is caused by the annihilation of electrons and their positron anti-particles. The anti-particles are produced by the decay of radioactive isotopes, which are produced by the high-speed proton collisions with atomic nuclei (*Strong et al.*, 1999).

Energy Release

Science is lacking a complete model for flare formation. It is generally agreed that the energy for flares comes from stressed magnetic fields. In a near perfectly conducting plasma, magnetic field lines are tied to plasma motions in regions where the gas pressure exceeds the magnetic pressure. The turbulent motions of the photospheric plasma can twist magnetic fields in the upper corona and stress them into highly non-potential states. Energy is stored in these non-potential states until a critical point is reached. In a process called reconnection, the magnetic topology of the region changes to a more relaxed, or potential, state. The energy liberated in this process is available for thermal heating of the plasma and for the acceleration of particles out of the thermal distribution. One model for reconnection consists of magnetic field lines, that are oppositely aligned, being pushed together in a reconnection region where they recombine to form two new loops, one moving downward and one moving upward. The problem lies in the time scales for reconnection. In order for field lines to reconnect they must diffuse through the plasma to form new connections. The change in a magnetic field in a plasma is governed by Faraday's law, which in a plasma can

be combined with Ampére's and Ohm's laws to write the *induction equation*

$$\frac{\partial \mathbf{B}}{\partial t} = \nabla \times (\mathbf{v} \times \mathbf{B}) + \eta_B \nabla^2 \mathbf{B}. \tag{1.3}$$

The first term on the right is how the magnetic field is advected with the plasma and the second term defines the rate that the magnetic field can diffuse through a plasma and is dependent upon the magnetic diffusivity as defined by

$$\eta_B = \frac{c^2}{4\pi\sigma}, \tag{1.4}$$

where c is the speed of light and σ is the electrical conductivity of the plasma. For most applications in the solar corona the plasma is considered to be in the *ideal MHD limit* with $\sigma = \infty$, making $n_B = 0$ and reconnection impossible. In order to study non-ideal processes a ratio of the first right hand side term of equation 1.3 to the second term is defined to give the relative importance of each in a given situation. This *Magnetic Reynolds Number*, also known as the *Lundquist Number*, R_M, is defined by replacing derivatives with l_0^{-1} where l_0 is a characteristic length scale of the system and replacing the velocity with a characteristic velocity scale of the system, v_0, to give the following expression

$$R_M = \frac{l_0 v_0}{\eta_B}. \tag{1.5}$$

Typical coronal values for the corona give $R_M \approx 10^8 - 10^{12}$ (*Priest and Forbes*, 2000a), which is an indicator of how difficult it is for magnetic fields to diffuse and reconnect in the corona.

Via some mechanism, the nature of which is still a matter of intense debate and study, the above limitations are overcome and reconnection occurs. The change in magnetic field implies the generation of an electric field via Faraday's law. This electric field is a potential

acceleration mechanism for the nonthermal electron populations that cause the aforementioned HXR power law spectrum. Numerous works have investigated the direct acceleration of electrons by electric fields caused by reconnection. *Wood and Neukirch* (2005) investigated the acceleration of test particles in a current sheet around a localized reconnection region. In the presence of a strong guide field in the ignorable direction, it was found that an initially thermal population of particles could be accelerated to a nonthermal beam, with energies comparable to those seen in flares and with a power law energy spectrum. The hardness of this spectrum was strongly determined by the maximum value of the electric field parallel to the magnetic field. This "simple" model for particle acceleration is attractive though there are numerous unresolved issues (See *Fletcher et al.*, 2007a; *Fletcher and Hudson*, 2008). However, the work described in this thesis is based on the assumption that nonthermal electrons are directly accelerated by electric fields in the region of the reconnection site and not secondary electric fields that may arise from waves, turbulence, etc.

While the exact method of particle acceleration may not be fully understood, it is known that the tenuous solar corona is not dense enough to produce the observed emission either in soft or hard X-rays. Material must be coming from some source and then heated to the point of emitting high energy radiation. The most popular theory for this transport of material is *chromospheric evaporation*. In this model a flare event in the corona heats the underlying layer in the solar atmosphere called the *chromosphere* either via a thermal conduction front or by superthermal electron beams colliding with the dense target provided by the chromosphere . The chromospheric plasma is heated to coronal temperatures and then expands and moves upward along magnetic field lines into the corona. There it emits the observed soft X-rays and drains back down into the chromosphere as it cools. This theory matches well with the observations of the Russian *Intercosmos-4* satellite that observed upward and downward Doppler shifts of flare plasma with velocities of up to 100 kilome-

ters per second. Years later *Skylab* detected similar motions during flares with velocities of $50\,km\,s^{-1}$ (*Strong et al.*, 1999). The instruments aboard *Skylab* allowed researchers to make crude electron density estimates of flaring regions. The densities observed were on the order of 10^{12} particles per cubic centimeter (*Strong et al.*, 1999). These densities were far too high for the corona but were similar to chromospheric densities, which added weight to the chromospheric evaporation theory. However, this theory does not perfectly match observations either. The improved instruments on *SMM* allowed the measurements of Doppler shifts and SXR emission. It was found that high velocity material started moving long before the HXR signature for high-speed electrons encountering the denser chromospheric plasma and continued after the HXR signal ended. If this was the case then the heating of the chromospheric material could not be a result of a flare event in the corona and the chromosphere was somehow independently heated (*Strong et al.*, 1999).

Fisher et al. (1985c) modeled two regimes in which chromospheric evaporation could occur. These regions are differentiated by the nonthermal energy flux by electrons with energies over $20\,keV$, F_{20}. *Explosive evaporation* occurred when energy fluxes $F_{20} \geq 5 \times 10^9 ergs\,cm^{-2}\,sec^{-1}$. In this regime chromospheric material is pushed downward into the lower chromosphere due to the overpressure relative to the denser underlying chromosphere as well as upward. This form of chromospheric evaporation was observed by *Milligan et al.* (2006a) with the *Coronal Diagnostic Spectrometer* (CDS; *Harrison et al.*, 1995) onboard the *SOHO* satellite with measured upward velocities of $\sim 2.70 \times 10^7\,cm\,s^{-1}$ and downflows of $3.5 \times 10^6 - 4.5 \times 10^6\,cm\,s^{-1}$. In *gentle evaporation*, which occurs when $F_{20} \leq 10^9 ergs\,cm^{-2}\,sec^{-1}$, a quasi-steady equilibrium between radiative losses and the nonthermal energy input develops allowing the heated material to expand upward in response to temperature increases. *Milligan et al.* (2006b) observed an example of gentle chromospheric evaporation, which showed no downflows and with upward velocities of $\sim 1.10 \times 10^7\,cm\,s^{-1}$. Both events were also observed by the *Reuven Ramaty High-Energy*

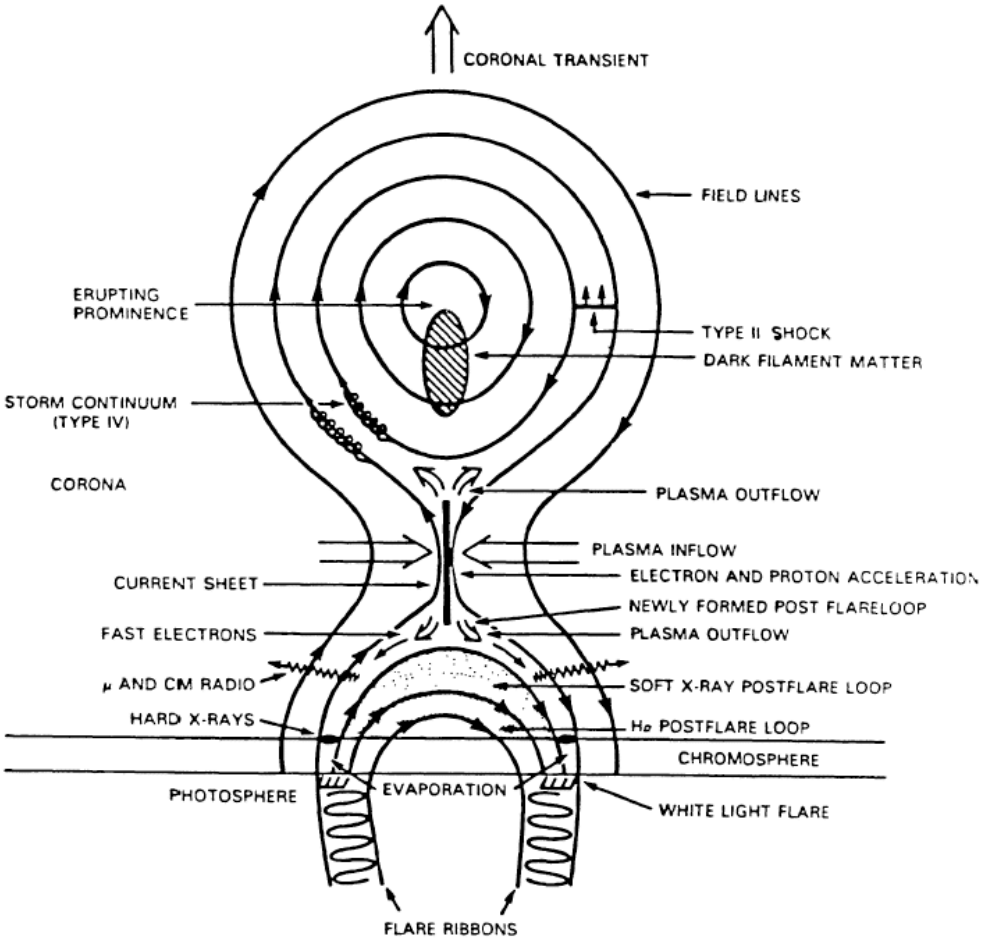

Figure 1.2: A diagram of a flare from *Martens and Kuin* (1989). Note the lack of a concentrated looptop emission source. The frequency at which such sources occur was a surprise to theorists and remains largely unexplained.

Solar Spectroscopic Imager (RHESSI; *Lin et al.*, 2002) with its unprecedented spectral range and resolution in both the SXR and HXR ranges. Using *RHESSI* it was possible to determine nonthermal electron flux penetrating the chromosphere for the first time for evaporative events. It was found that the explosive case had an order of magnitude larger electron flux than the gentle case, which was predicted twenty-one years prior by *Fisher et al.* (1985a; 1985b; 1985c).

Looptop X-ray Sources

The first evidence of an emission source at the apex of flaring loops was provided by observations of the 1973 June 15 flare by the NRL slit-less objective grating spectrograph onboard *Skylab*. These observations showed a $1.7 \times 10^7\,K$ region at the loop apex with the temperature decreasing down the loop length (*Cheng*, 1977). Unfortunately, *Skylab* was launched during a time of low solar activity and high resolution images of flares were rare (*Acton et al.*, 1992). The fact that such an emission source existed was a surprise due to the low densities in the corona. Even more surprising was that a majority of flares had looptop emission sources.

The *Hinotori* (*Tanaka*, 1983) and *Solar Maximum Mission* (*SMM*) (*Strong et al.*, 1999) satellites observed numerous flares in concert. *Hinotori* was able to make images of flares in the $6-12\,keV$ and the $15-40\,keV$ bandpasses. *Hinotori* observations showed that extended HXR sources are a common feature of two types of flares: *impulsive*, showing an HXR burst with rapidly varying spikes; and *gradual-hard* with long ($>30\,min$) HXR emission with a broad, slowly varying peak and a hard photon spectrum ($\gamma = 5-8$) (*Tanaka*, 1987). In impulsive flares small kernels of HXR emission were seen between the flare ribbons. Observations of limb flares of this type reinforced the interpretation that these kernels where actually located at the loop apex. Looptop sources were found to be the major contributor of emission in the $20-30\,keV$ bandpass in the majority of examples (*Tanaka*, 1987). This seems to contradict the thick-target model of HXR emission which would indicate that higher plasma densities are needed for significant HXR emission (*Brown*, 1971). Whether the emission was thermal or nonthermal in nature remained an open question (*Tanaka*, 1987). Gradual-hard flares showed an extended source at the top of flare loop arcades throughout the flare. In later phases of the flare, co-spatial SXR sources appeared, with only a few showing a small displacement ($\leq 10''$) from the centroid of the HXR emis-

sion (*Tanaka*, 1987). The HXR emission was interpreted as Bremsstrahlung radiation from a nonthermal population of electrons trapped in the coronal portion of the post-flare loops. HXR spectral information for the 1981 May 13 flare was available from *SMM*'s *Hard X-ray Burst Spectrometer* (HXRBS; *Orwig et al.*, 1980) and showed a hard HXR photon spectral index of $\gamma_p \sim 3.6$. Attempts to model the HXR photon emission using a perfect magnetic trap model (*Bai and Dennis*, 1985) yielded a target plasma density that was two orders of magnitude smaller than the density needed to explain the SXR emission seen by *Hinotori* (*Tanaka*, 1987). At the higher density, nonthermal electrons with an energy of $< 30\,keV$ would be thermalized quickly, necessitating a continuous replenishment of nonthermal particles at the loop apex over the life of the flare (*Tanaka*, 1987). Resolving this discrepancy remains a central topic in solar flare research.

Acton et al. (1992) compiled a survey of ten flares observed with Soft X-ray Telescope (SXT; *Tsuneta et al.*, 1991) on board the *Yohkoh* satellite (*Ogawara et al.*, 1991). These flares all showed a compact (often only seen in one $2''$ square pixel) emission source at the flare loop apex with a temperature of $\sim 2 \times 10^7\,K$. These sources appeared almost at the onset of the flare and continued well into the decay phase. The sources also remained compact throughout the flare and did not spread down the loop legs. The compactness of the source, its long life and the early onset, made it difficult to explain the increased emission as a density enhancement caused by chromospheric evaporation (*Acton et al.*, 1992).

The best known observation of a looptop emission source is the famous *Masuda flare* of 1992 January 13 (*Masuda et al.*, 1994). This flare was observed simultaneously by SXT and the Hard X-ray Telescope (HXT; *Kosugi et al.*, 1991). The observations clearly showed a SXR (thermal) loop in the SXT thick aluminum and beryllium channels. It also showed three HXR sources, two at the footpoints and one *above* the SXR loop apex, in the HXT L $(14-23\,keV)$, M$(23-33\,keV)$, and M1$(33-53\,keV)$ bands. This was the first observation

of a source above the SXR loop and was thought to be an indication of the reconnection site. The original interpretation of the emission was that the source was a thermal plasma whose temperature was raised to $2 \times 10^8 K$ by an unknown mechanism, most likely shock heating (*Masuda et al.*, 1994). This high temperature was an order of magnitude larger than previously seen in flares. The thermal interpretation was initially questioned on the grounds that the source varied on a time scale shorter than the local thermalization time scale (*Hudson and Ryan*, 1995). It was later determined that a thermal description of the emission was not consistent with the observations when ratios of multiple HXT filters were taken into account (*Alexander and Metcalf*, 1997). *Alexander and Metcalf* (1997) also found that HXR emission at both the footpoints and the loop apex could be explained by a single source of nonthermal particles. In this scenario, the loop apex acted as a thick target for electrons with an energy $\leq 20 keV$ and a thin-target to electrons with a higher energy. The HXR emission source then became entirely thermal after the impulsive phase of the flare with a temperature of $2 \times 10^7 K$.

Further observations seemingly invalidated the theory that looptop sources are solely the product of chromospheric evaporation. The thermal emission scales as the square of the density increase caused by chormospheric evaporation ($I_{th} \propto n_e^2 V$, where V is the volume of the emitting region). The increased density also provides a thicker target for nonthermal Bremsstrahlung, which linearly increases the nonthermal emission. The expected morphology of a flare loop would then be a strong brightening of footpoint sources, in both HXR and SXR which would then be followed by a somewhat weaker emission at the loop apex. However, a survey of flares that were observed by *HXT* and *SXT* found that this morphology was a rarity, occurring only eight times in the thirty-six flares studied (*Nitta et al.*, 2001). *Fletcher and Martens* (1998a) numerically modeled the HXR emission of nonthermal electron beams in a converging magnetic trap model. It was found that in a magnetic field geometry of a Syrovatskii current sheet (*Syrovatskii*, 1971) the apex HXR

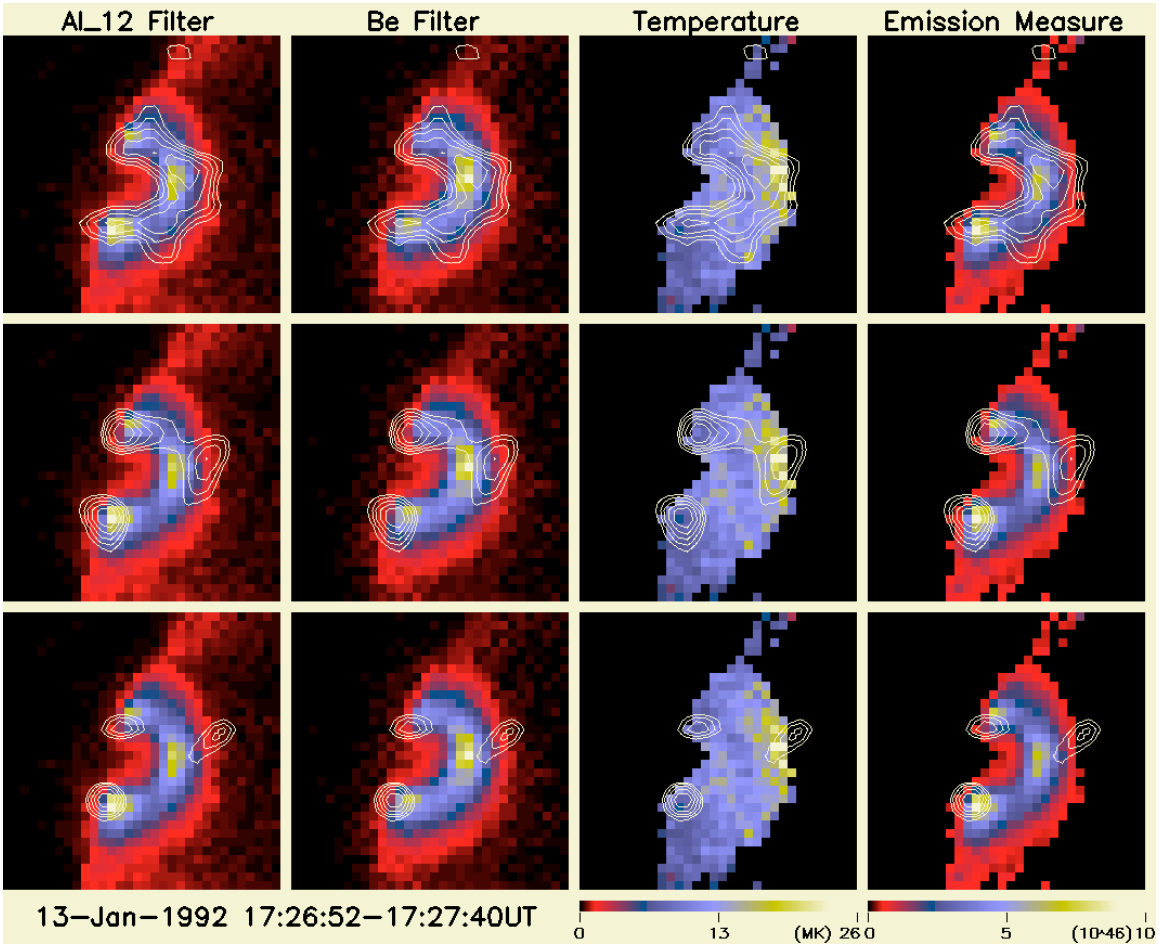

Figure 1.3: The famous Masuda flare (*Masuda et al.*, 1994) of 1992 Jan. 13. Hard X-rays are shown in contours and the results from soft X-rays are in color. From left to right, the first two columns show images from the SXT thick aluminum and beryllium filters respectively and the temperature and emission measure derived from their ratio in the last two columns. The rows represent images obtained form HXT in three hard X-ray energy bands: 13.9-22.7 keV, 22.7-32.7 keV, and 32.7-52.7 keV respectively.

emission was larger and more compact than in previous models which used semi-circular geometries for flare loops. However, this model only applied to the HXR emission. The source of the SXR emission at the loop apex remained unexplained.

Sui et al. (2006) made a serendipitous *RHESSI* observation of X-ray sources moving along the legs of a flare loop. A survey was performed of *early impulsive flares*, where impulsive hard X-ray emission is seen before a significant rise in soft X-ray emission. This would allow for a spectral analysis of the nonthermal spectrum down to energies of $< 10\,keV$ without contamination from thermal spectra. This is important for determining the low energy cutoffs in the nonthermal electron energy spectrum. *RHESSI* made observations of a C1.1 early impulsive flare on 2002 November 28, near the southwest solar limb, starting at 04:35:30 UT. This was a rare observation since none of the attenuators were in front of the germanium detectors. This allowed *RHESSI* to make observations at energies as low as $3\,keV$. These low energy observations showed a $3-6\,keV$ X-ray source that started at the loop apex, bifurcated, moved down the flare legs at speeds of ~ 500 and $700\,km\,s^{-1}$, then moved back upward at an average speed of $\sim 340\,km\,s^{-1}$ (*Sui et al.*, 2006).

The initial interpretation of this newly observed motion was that it was an effect of the soft-hard-soft (SHS) spectral evolution of the nonthermal particle beam (*Sui et al.*, 2006). A large number of flares have been observed to have a power law photon spectrum that goes from a large γ (soft), to a small γ (hard), then back to a small γ (*Grigis and Benz*, 2004; *Benz*, 2008). If the relationship between γ and δ is assumed to be linear, as the thick and thin target models suggest, then the SHS pattern is suggestive of a nonthermal particle accelerator that shows a similar evolution in time. *Sui et al.* (2006) proposed that as the nonthermal electron energy spectrum hardens in time, there is a larger population of high energy particles, which can then penetrate more deeply into the loop plasma. This gives rise to an apparent downward motion. Likewise, as the spectrum softens again, the lack of higher energy particles in the distribution restricts the depth that the nonthermal particles

can penetrate, giving rise to an apparent upward motion (*Sui et al.*, 2006). However, spectral observations of this flare have yet to be published and the ratio of thermal to nonthermal energy contained within these sources remains unknown.

Research Motivation

While observations from ever more sophisticated instruments have revealed many new aspects of solar flares, these new observations have the annoying habit of raising as many new questions as they answer. Clearly, a true understanding of solar flare processes and features will only be gained by combining observations with models of flares based on theoretical considerations. Many attempts have been made to simulate solar flares numerically. For the most part these can be separated into two groups: Those that model the hydrodynamic aspects of a flare (See *Mariska et al.*, 1989; *Reeves et al.*, 2007) while using an analytic expression for heating due to nonthermal electrons, and those that model the evolution of the nonthermal particle beam (See *Leach and Petrosian*, 1981; *Fletcher and Martens*, 1998a; *McClements and Alexander*, 2005) while using a static thermal atmosphere.

In this work a hybrid loop model is devised that combines models of a hydrodynamic plasma contained within a solar loop and models of nonthermal particle evolution in a self-consistent way. There have been other attempts to achieve this (*Miller and Mariska*, 2005; *Liu*, 2006). This work is unique in the way that it treats the nonthermal particles. Previous works treat nonthermal particle evolution via a numerical scheme to solve the Fokker-Planck equation. In this work, nonthermal particles are directly modeled as test particles which undergo stochastic processes as they evolve. This allows the use of measurements of statistical error in the simulations that are not present in previous works.

In this work the basic equations involved in the evolution of the thermal plasma and the

nonthermal particles are outlined, and the ways in which they are treated numerically are explained. An experiment is then conducted where the effects of including a hydrodynamic plasma model and a nonthermal particle model are compared to a nonthermal model with a static atmosphere in the generation of HXR looptop emission sources.

CHAPTER 2

THEORY

When dealing with plasmas it is often useful to describe the distribution of a species of particles in a 7 dimensional phase space, $f(\mathbf{r},\mathbf{v},t)$ where $\mathbf{r}$ is the position vector, $\mathbf{v}$ is the velocity vector. and t is time. The evolution in time of this *distribution function* is given by taking the total time derivative of f to yield

$$\frac{df}{dt} = \frac{\partial f}{\partial t} + \begin{array}{l} \frac{\partial f}{\partial x}\frac{dx}{dt} + \frac{\partial f}{\partial y}\frac{dy}{dt} + \frac{\partial f}{\partial z}\frac{dz}{dt} + \\ \frac{\partial f}{\partial v_x}\frac{dv_x}{dt} + \frac{\partial f}{\partial v_y}\frac{dv_y}{dt} + \frac{\partial f}{\partial v_z}\frac{dv_z}{dt} \end{array} . \tag{2.1}$$

When $\frac{df}{dt}$ represents the effects of two-body, large angle collisions, Eq. (2.1) is known as *Boltzmann's Equation* first derived by Ludwig Boltzmann in 1872 (*Lifshitz and Pitaevskii*, 1981; *Parks*, 2004; *Sturrock*, 1994). By recognizing velocity and acceleration terms in Eq. (2.1) it can be simplified to

$$\frac{df}{dt} = \frac{\partial f}{\partial t} + \mathbf{v}\cdot\frac{\partial f}{\partial \mathbf{r}} + \mathbf{a}\cdot\frac{\partial f}{\partial \mathbf{v}} . \tag{2.2}$$

In the study of astrophysical plasmas, often only electromagnetic forces are considered. Applying *Newton's Second Law* and the *Lorentz Force Law* to Eq. (2.2) yields

$$\frac{df}{dt} = \frac{\partial f}{\partial t} + \mathbf{v}\cdot\frac{\partial f}{\partial \mathbf{r}} + \frac{q}{m}\left(\mathbf{E} + \frac{\mathbf{v}}{c}\times\mathbf{B}\right)\cdot\frac{\partial f}{\partial \mathbf{v}} , \tag{2.3}$$

where m and q are the particles' mass and charge, respectively and $\mathbf{E}$ and $\mathbf{B}$ are the electric and magnetic fields. In the absence of close or binary collisions, Eq. (2.3) becomes the *Vlasov Equation* first studied by A.A. Vlasov in 1945 (*Parks*, 2004). An accurate picture

of space plasmas can be gained by coupling Eq. (2.3) with *Maxwell's Equations.* However, the non-linearity of these coupled equations makes finding solutions a challenging endeavor.

One of the difficulties in modeling solar flares is the distribution of particles often consists of two distinct components, one thermal and one nonthermal. These two components interact, exchanging energy and momentum, but have drastically different characteristic scale lengths that govern their evolution. Not surprisingly, there are also two broadly different statistical approaches in plasma physics. The *magnetohydrodynamic* (MHD) approach assumes that the plasma can be treated as a thermal gas and represented by properties averaged over the velocity distribution. The *kinematic* approach makes no such assumptions and expresses the evolution of the distribution of particles directly instead of by averages. In this work the MHD approach is applied to the thermal component of the distribution plasma while the kinematic approach is applied to the nonthermal component.

This chapter is devoted to the description of the new hybrid loop modeling software suite, HYLOOP. HYLOOP is composed of two main components that treat the thermal component and the nonthermal component as separate but interacting distributions of particles. MSULOOP uses the MHD approach in one dimension to calculate the evolution of a thermal plasma. It is the successor to the code used to model X-ray bright points by *Kankelborg and Longcope* (1999), with modifications made to aid in the study of highly dynamic phenomena such as flares. The *Particle Tracking Codes*, PATC, is a completely new set of programs designed to use the kinematic approach and track the evolution of nonthermal particle beams.

Equations Describing the Thermal Distribution

Many numerical modeling codes have been written for coronal loop studies (*Dmitruk*

and Gómez, 1999 & *Aschwanden and Schrijver*, 2002 are a couple of examples). A recent survey of loop modeling codes (*Mulu-Moore et al.*, 2007) showed that not every code could reproduce the RTV scaling laws that have been a cornerstone in the study non-flaring loops for decades (*Rosner et al.*, 1978). These differences emphasize the fact that numerical loop models are not to be treated as black boxes. The underlying equations and assumptions that comprise any code must be understood in order to determine the regimes where the code's results have validity. With this fact in mind, the equations and assumptions that go into the hydrodynamic equation solver MSULOOP, will be examined.

Thermal Distribution

First, a characteristic scale length is derived that will aid in the discussion of a plasma. Consider the electrostatic potential, ϕ, of a charge surrounded by freely moving particles with an equal number of either charge. The particles will align themselves in a way to minimize the energy of the potential, $q\phi$. Thus the effective potential will be screened and have the form

$$\phi = \frac{q}{r}\exp\left[\frac{-r}{\lambda_{Debye}}\right], \tag{2.4}$$

where the *Debye length*, λ_{Debye}, has been defined as the *e*-folding distance, i.e. distance required to reduce the potential by e^{-1} (*Parks*, 2004). If a point charge is placed in a neutral distribution of particles, its potential is effectively screened out at distances larger than the Debye length. For a plasma of temperature T and particle density of n the Debye length is given by

$$\lambda_{Debye} = \left(\frac{k_B T}{8\pi n e^2}\right)^{1/2} [cm] \tag{2.5}$$

where k_B is the ubiquitous *Boltzmann's constant* in cgs units and e is the basic unit of charge in esu units. Assuming a flare plasma with a temperature of $T = 10^7 K$ and an

electron density of $n_e = 10^9\,cm^{-3}$ which is assumed to be half of the total number density, the Debye length is $\lambda_{Debye} \simeq 0.2\,cm$. This is an important length scale that will be used in numerous other definitions and only for scales larger than this length can the plasma be considered to be a neutral fluid.

Another useful quantity when determining which equations are applicable to a given distribution of particles is the plasma parameter, g_p, which is defined as

$$g_p \equiv \frac{1}{N_D}, \tag{2.6}$$

where $N_D \equiv \frac{4\pi n \lambda_{Debye}^3}{3}$ and is the number of particles contained within a sphere with a radius equal to the Debye length. If $g_p \ll 1$ then there are a large enough number of particles to apply statistical arguments and treat the system as a fluid plasma instead of individual particles. A small value of g_p also ensures that the number of binary collisions will be low and an individual particle will interact with the plasma via long range collective effects (*Parks*, 2004; *Choudhuri*, 1998).

After just a few collisions, an initial distribution of particles will eventually evolve into a *Maxwell-Boltzmann distribution* which has the form in velocity space of

$$f_{MB}(\mathbf{v}) \equiv \left(\frac{m}{2\pi k_B T}\right)^{3/2} exp\left[\frac{-mv^2}{2k_B T}\right], \tag{2.7}$$

The definition of the thermal plasma then becomes a system of particles where deviations from the thermal, Maxwell-Boltzmann distribution are considered to be small and therefore ignored. This occurs in time scales defined by the *thermal electron and proton relaxation time*s. These are the time scales under which slightly non-Maxwellian distributions of electrons and protons exchange energy and momentum and relax to a Maxwellian distribution of velocities. The thermal electron and proton relaxation times are estimated numerically

by *Sturrock* (1994) as

$$\tau_{Me} \approx 10^{-1.49} \frac{T^{3/2}}{2n_e} [s], \tag{2.8}$$

$$\tau_{Mp} \approx 10^{-0.12} \frac{T^{3/2}}{2n_e} [s], \tag{2.9}$$

where an assumption of a fully ionized hydrogen plasma has been made and the *Coulomb logarithm* is assumed to be $\ln\Lambda \approx 20$ in the solar corona. Again, using $T = 10^7 K$ and $n_e = 10^9 cm^{-3}$ gives a value of the thermal electron relaxation time of $\tau_{Me} \approx 0.5 seconds$ and a thermal proton relaxation time a $\tau_{Mp} \approx 12 seconds$. The use of a Maxwellian distribution function is a good approximation for effects that have characteristic time sclaes larger than these relaxation times. A mean free path for an electron can be defined as

$$\lambda_{mfp} \equiv \tau_{Me} v_{rmse} [cm] \tag{2.10}$$

where v_{rmse} is the thermal electron speed given by

$$v_{rmse} = \left(\frac{3k_B T}{m_e} \right)^{1/2} \left[cm\, s^{-1} \right],$$

where m_e is the electron mass. Again, using the typical flare values defined previously $v_{rmse} \approx 2.13 \times 10^9 cm\, s^{-1}$. Using this yields a mean free path of $\lambda_{mfp} \approx 8.6 \times 10^8 cm$. As long as the characteristic scale lengths of the density, $L_{n_e} \equiv \left(\frac{dn_e}{dx} \right)^{-1}$ and the temperature, $L_T \equiv \left(\frac{dT}{dx} \right)^{-1}$, are larger than λ_{mfp} then an assumption of local thermal equilibrium is a good one and the approximation that the distribution is Maxwellian can be used (*Choudhuri*, 1998).

MHD Equations

With a suitably small value of g_p the macroscopic properties of plasma are adequate

to describe the state of the system. The macroscopic properties can be found by taking averages over the distribution. These averages are defined by

$$\langle Q \rangle \equiv \int_{-\infty}^{\infty} Q f(\mathbf{v}) \, d^3\mathbf{v}, \tag{2.11}$$

where Q is the variable of interest. The state of a thermal plasma can be determined by three velocity averaged variables; density, n, the mean or bulk velocity, $\mathbf{V}$, and internal energy density, ε as defined by

$$n(\mathbf{x},t) \equiv \int f(\mathbf{x},\mathbf{v},t) \, d^3\mathbf{v} \tag{2.12}$$

$$\mathbf{V}(\mathbf{x},t) \equiv \frac{1}{n} \int \mathbf{v} f(\mathbf{x},\mathbf{v},t) \, d^3\mathbf{v} \tag{2.13}$$

$$\varepsilon(\mathbf{x},\mathbf{t}) \equiv \frac{m}{2n} \int (\mathbf{v}-\mathbf{V})^2 f(\mathbf{x},\mathbf{v},t) \, d^3\mathbf{v}. \tag{2.14}$$

Just as the state variables were defined by taking moments of the distribution function, the equations that govern their evolution are derived by taking successive moments of Boltzmann's equation to yield,

$$\frac{\partial \rho}{\partial t} + \nabla \cdot (\rho \mathbf{V}) = 0 \tag{2.15}$$

$$\frac{\partial \mathbf{V}}{\partial t} + (\mathbf{V} \cdot \nabla)\mathbf{V} = \mathbf{F} - \frac{1}{\rho}\nabla P + \frac{1}{4\pi\rho}(\nabla \times \mathbf{B}) \times \mathbf{B} + \frac{1}{\rho}\nabla \cdot (\mu_v \nabla \cdot \mathbf{V}) \tag{2.16}$$

$$\frac{\partial \varepsilon}{\partial t} + \nabla \cdot (\varepsilon \mathbf{V}) = -P\nabla \cdot \mathbf{V} + \nabla \cdot (\kappa \nabla T) - n_e^2 \Lambda_{rad}(T) + E_H + \mu_v (\nabla \cdot \mathbf{V})^2. \tag{2.17}$$

These equations are the continuity equation, Eq. (2.15), the momentum equation, Eq. (2.16), and the energy equation, Eq. 2.17. The evolution of the magnetic field must also be

taken into account and is given by the induction equation,

$$\frac{\partial \mathbf{B}}{\partial t} = \nabla \times (\mathbf{V} \times \mathbf{B}) + \lambda \nabla^2 \mathbf{B}. \tag{2.18}$$

In order to make the MHD equations more tractable, a variety of simplifications are used in the MSULOOP code. Firstly, the effects of viscosity are ignored in the experiments described here and the *kinematic viscosity*, $\nu = \mu_v/\rho$, has been set to zero. It is acknowledged that viscosity can play an important role in the evolution of flares (*Peres and Reale*, 1993) and this role will be investigated in subsequent work. Also, the ideal MHD limit is taken which states that the conductivity of the coronal plasma is so high that the diffusivity, λ, can be essentially set to zero. This along with the additional assumption that the magnetic field is reasonably static within the time frame of the simulation, allows for the removal of the induction equation, Eq. (2.18) (*McMullen*, 2002). The magnetic field, however, is not ignored as the plasma is constrained to flow along the magnetic field lines and defines the coordinate s along the loop length. The MHD equations have now been reduced to 1D hydrodynamic equations with the magnetic field providing the geometry of the coronal loop.

In this work any cross-field diffusion effects are ignored and particles are constrained to a characteristic field line for the duration of the simulation. With the magnetic field providing a convenient axis of symmetry, the three dimensional properties of a coronal loop are mapped onto a one dimensional grid. The coronal loop is specified by the coordinate along the loop length, s, the component of acceleration due to gravity along the magnetic field, $g_{\parallel}(s)$, the non-uniform cross-sectional area of the loop, $A(s)$ and the three plasma state variables: the electron density $n_e(s,t)$, bulk velocity $\mathbf{V}(s,t)$, and the internal energy

density $\varepsilon(s,t)$, without any loss of generality. The equations used by MSULOOP are

$$\frac{\partial n_e}{\partial t} = -\frac{1}{A}\frac{\partial}{\partial s}(An_eV) \tag{2.19}$$

$$\frac{\partial V}{\partial t} = \frac{-1}{n_e m_p}\frac{\partial P}{\partial s} + g_{\parallel} - V\partial V \tag{2.20}$$

$$\frac{\partial \varepsilon}{\partial t} = -\frac{1}{A}\frac{\partial}{\partial s}(A\varepsilon V) - \frac{P}{A}\frac{\partial}{\partial s}(AV) - E_{Rad} + \frac{1}{A}\frac{\partial}{\partial s}(AF_c) + E_H \tag{2.21}$$

In the above equations the divergence operator ($\nabla\cdot$) has been replaced with $\frac{1}{A}\frac{\partial}{\partial s}A$ in order to ensure that flux conservation laws are strictly obeyed on a nonuniform grid. The conductive flux (F_C) and the radiative losses (E_{Rad}) are discussed in detail in later sections. The heating term (E_H) is not well known in the corona and is usually a free parameter to be tested under simulation. Another assumption being made in the simulations is that the ratio of gas pressure to magnetic pressure is small, $\beta \ll 1$, throughout the loop length. Along with an equation of state, $P = \frac{2}{3}\varepsilon = 2n_e k_B T$, where P denotes the gas pressure, the evolution of the thermal plasma in a loop is completely described with the three predefined state variables.

These equations are then solved on a staggered spatial grid (defined below) by using a second order Runge-Kutta Modified Midpoint Method (*McMullen*, 2002; *Press*, 2002). This method is not the most computationally efficient. However, Runge-Kutta methods are self-starting, which means that only the initial conditions for the equations need to be known in order to perform the calculation *ad infinitum* and small errors are not amplified as the calculations progress (*Arfken and Weber*, 1995). Considering the current trend towards inexpensive computational time and power, the ease of use and stability of the Runge-Kutta method seems to far outweigh its computational efficiency shortcomings.

Grids

On the Sun, the plasma contained within coronal loops evolves in a continuum of space and time. However, numerical methods cannot deal with continua. The volume that the plasma occupies and the time over which it evolves have to be broken down to discrete chunks to form grids. The definition and size of the grids is a non-trivial matter.

Spatial MSULOOP solves Eqs. (2.19)-(2.21) on a one-dimensional, staggered grid that consists of a series of volumes and cross-sectional surfaces that bound those volumes on either side. Since any processes that would allow for particles to diffuse across field lines are not currently included in the simulations, the surfaces perpendicular to the loop axis, as defined by a magnetic field line, are ignored. The volumetric state variables ε and n_e are defined within volumes. The bulk velocity, V, the cross-sectional areas, A, parallel components of the gravitational acceleration, $g_{\parallel}$, and the magnetic field strength, B are defined on surface grids parallel to the magnetic field.

To understand why the effort is spent on defining a staggered grid, which makes book keeping more difficult, one has to look at the numerical methods chosen to deal with the advective portions of the Eqs. (2.19)-(2.21). The simplest stable method for solving an advection type equation is an *upwind differencing scheme,* which uses different expressions of the differential equation depending upon the sign of the velocity (*Morton and Mayers*, 1994). When all variables are defined the same grid this is only a first order accurate scheme in space and time. See Appendix B for a discussion on order accuracy. The stability criterion for upwind differencing is the Courant, Friedricks, Lewy (CFL) condition,

$$\Delta t \leq \frac{\Delta s}{v}, \tag{2.22}$$

which is the condition for convergence for a surprising number of numerical schemes (*Mor-*

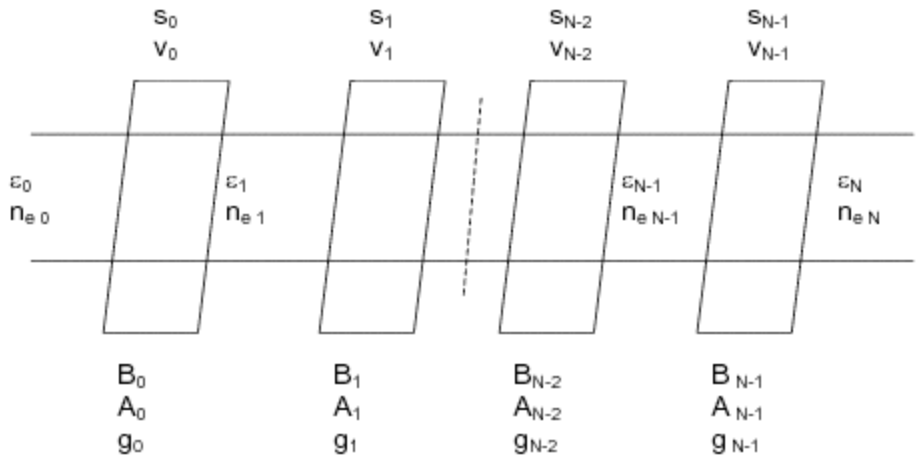

Figure 2.1: A visual representation of the staggered grid system. The energy and electron number densities, ε, n_e are defined in N volumes. Other quantities, such as velocity, v, magnetic field strength, B, area, A, and parallel component of acceleration due to gravity, g, are defined on $N-1$ surfaces. The first and last volume serve as static boundary conditions for the grids and are not altered by the simulation.

ton and Mayers, 1994). Making smaller step sizes in time, which increases the stability, decreases the spatial accuracy of the result. The accuracy of this calculation can be improved by using values interpolated between the volume grids (*Press*, 2002). By having certain quantities defined on the surface grid and others defined in the volumes bounded by that grid, the upwind differencing is second order accurate with a minimum amount of additional interpolations.

It is not possible to have the spatial grids be arbitrarily small and have a simulation finish within a graduate student's lifetime. Decisions must be made on how to distribute grid spacings in order to yield a physically meaningful simulation within the constraints of the current computing resources. Thin transition region like layers may form in simulations and move with time. These layers might not be resolved with grids set for the corona and lead to numerical inconsistencies (*Antiochos et al.*, 1999). How to define the resolution of a grid is not straightforward and currently there has not been a definitive criterion to base grid size upon. *Antiochos et al.* (1999) found that defining grids based on the local density

worked well due to the density's strong spatial dependence in both the transition region and the chromosphere. In accordance with this finding, grid spacings are distributed as a Gaussian function ensuring that the smallest grids are at the base of the loop where the density is the largest and the largest grid steps are at the loop apex where the density is at a minimum.

The choice of grid spacing can alter the outcome of a simulation. If grids are chosen too coarsely then the local truncation error increases to the point where the errors overwhelm the state variables and the simulation is invalid. If grid spaces are chosen to be too fine then computation time unnecessarily increases. Adaptive mesh refinement techniques exist to calculate grid spacings that minimize both truncation error and run time (See *khattri*, 2006; *Dreher and Grauer*, 2006, for examples). Since plasma parameters rapidly vary in solar flares *adaptive mesh refinement* (AMR) schemes for changing the spatial grid spacing during a simulation were studied. However, it was decided to use a simpler method of determining grid size for the initial use of this new code. Each simulation is initially run on a coarse, static grid with the spacing distributed as a Gaussian function with the maximum percent difference between the step size of one grid point to the next being set to 10%. Successive simulations were run, each having a greater number of cells than the last. State variables are monitored for each run and percent differences are taken of these quantities, comparing each run to a reference grid of arbitrarily small grid spacing. This procedure is repeated until the percent difference fell below a tolerance level defined for each run. The results for these tests are reported in Chapter 3.

Temporal It is easy to see how changing a characteristic time scale can alter the fidelity of a simulation. However, just as it was the case with spatial grids, temporal grids cannot be arbitrarily small or the real time of simulation will be longer than is tolerable. The HYLOOP codes have four characteristic time scales, each of which must be properly calculated for

a simulation to finish and have some bearing on reality. The time step that governs the nonthermal particles' evolution, $\Delta_P t$ is defined in the section describing nonthermal particle transport.

The CFL condition, Eq. (2.22), requires that shocks do not propagate through a grid to another cell before the calculation in the next grid finishes. If this condition is not met then one side of a grid would not be "aware" of what is happening on the other side, and the solution would quickly became unstable (*Press*, 2002). HYLOOP uses a modified form of the CFL condition and forces the hydrodynamic equations to be iterated forward in time by a step proportional to the following formula

$$\Delta_g t \leq min\left[\frac{\Delta_g s(i)}{c_s(i)+|v(i)|}\right] \tag{2.23}$$

where i is the cell index, $\Delta_g s(i)$ is the length of the ith spatial grid cell, $c_s(i)$ is the local sound speed, and $|v(i)|$ is the absolute value of the velocity of the thermal plasma. Equation (2.23) is an upper bound for a stable simulation. The time step derived in Eq. (2.23) is divided by a user defined safety factor, S_0, usually set to 5 in order to increase the stability and fidelity of the upwind differenced quantities (*Press*, 2002). It is easy to see from Eq. (2.23) how refining the spatial grid can quickly lead to an inordinate increase in run time. When the spatial grid scale is reduced, either locally or globally, not only must the code solve the hydrodynamic equations on more spatial grids but the time step is also reduced, leading to even more calculations per reporting time step.

The next time step defines the rate at which information is passed between MSULOOP and PATC. This communication time step, $\Delta_C t$, is user defined. Ideally this time step would be the same as $\Delta_g t$. However, due to the large number of test particles used in each simulation and the number of calculations that have to be performed per particle, the run times for $\Delta_C t = \Delta_g t$ became prohibitively large on the current computing resources even with mod-

est improvements in parallel processing capability and efficient code writing techniques. In general practice $\Delta_C t \sim 10^{-3}\, sec$. Particles are allowed to propagate along a static plasma during this time. The energy and momentum loss of the particles then become input terms for the hydrodynamic plasma. The plasma is allowed to evolve until it catches up in time with the particle simulation. The particles then have an updated target plasma and the process repeats. It should be noted that the value of $\Delta_C t$ used in HyLoop represents an improvement of three orders of magnitude from the previous state of the art codes (*Liu*, 2008).

The next time step to be defined is the reporting time step, $\Delta_R t$. This is the largest of the time scales and is user defined. It would strain the capacity of the available storage disk infrastructure to maintain records of all state and particle variables on the smallest time scales used to solve the myriad of equations contained within HYLOOP. Instead, all of the information calculated by the codes is written to disk every $\Delta_R t$ of simulated time. While having this time scale be larger than the other characteristic time scales does entail a loss of information, it is deemed a necessary loss. Not only would many gigabytes of data be compiled by the codes if the reporting time step is not orders of magnitude larger than the other time scales, but since the writing of information to disk still involves the moving of physical parts for most systems, the run time would also increase significantly. While this time scale does not affect the fidelity of the simulation, it can affect the estimation of thermal emission, which is calculated post simulation.

Radiative Losses

Corona In the corona, ions are excited primarily by collisions and de-excited by via dielectronic recombination and the emission of photons (*Aschwanden*, 2005). For the most part, the simulations are dealing with an optically thin plasma and the photons are free to

radiate into free space without re-absorption. This results in a net loss of energy from the corona. The description of the radiative losses of an optically thin plasma is given by

$$E_{Rad} = n_e^2 \Lambda_{Rad}(T). \tag{2.24}$$

To determine radiative losses a radiative loss curve, $\Lambda_{Rad}(T)$, has to be computed in a manner that is both numerically efficient and yields a good approximation to the true radiative losses in the solar corona. A piecewise-continuous function expressing the radiative losses of an optically thin plasma is calculated using the CHIANTI spectral database package (*Dere et al.*, 1997) in the SOLARSOFT software distribution. CHIANTI calculates spectral and continuum photon emission with a given set of elemental abundances.

It is well known that the abundances of elements in the corona differ significantly than their photospheric values and that this variation is strongly dependent upon the first ionization potential (FIP) of each element. Since hydrogen is fully ionized in the corona, it is usually not possible to determine the absolute abundances, i.e., abundances with respect to hydrogen (see *White et al.*, 2000 for a counter example). Instead, only measurements of relative elemental abundances are possible. Relative abundances are calculated as a ratio between the fraction of a given element and another element, whose abundance is also in doubt. This leads to much debate on whether the abundances of high FIP elements are being depleted by a factor of ~ 4, low FIP elements are being enhanced by a factor of ~ 4, or a combination of enhancement and depletion (see *Feldman and Widing*, 2003 for a review). Recently, a mechanism that explains the observed coronal abundance variations has been proposed that has been very successful in matching observed values (*Laming*, 2004). This model supports the view that, on average, high FIP elements are depleted by a factor of ~ 4 in the corona as suggested by *Meyer* (1985). The current set of simulations use a radiative loss curve calculated with Meyer abundances under an assumption of constant pressure as

described by *Martens et al.* (2000). Even though abundances vary in time and from place to place (*Feldman and Widing*, 2003) it is asserted that this average treatment is suitable for modeling the radiative loss curve and it should be noted that this treatment is consistent with other state of the art coronal loop models (*Klimchuk et al.*, 2007).

Chromosphere and Transition Region It was shown by *McClymont and Canfield* (1983) that optical depth effects in the transition region play an important role in determining the stability of coronal loops. This complicates things greatly from the optically thin case since the nonlocal nature of the opacity means that a full treatment of radiative losses in the lower transition region and chromosphere requires a full 3D radiative hydrodynamics code (*Allred et al.*, 2005). There are other effects that conspire to make radiation loss calculations more difficult in lower temperature regions. The assumption of a fully ionized plasma, which is implicit in the calculation of Eq. (2.24), is not valid for solar plasmas with temperatures $\leq 20,000\,K$, which can be composed of 10% neutral hydrogen and thus drastically increase the radiative losses (*Fontenla et al.*, 1991). In the *ambipolar diffusion* process, electric fields are set up in weakly ionized plasma that counteract charge separation and ensure that ions and electrons diffuse from regions of high density to low density at the same rate (*Choudhuri*, 1998). In gravitationally stratified atmospheres this has the curious effect of setting up an electric field that "buoys up" heavier ions and "weighs down" electrons. One effect of this is that the plasma scale height is twice that expected by a non-ionized gas made up of the same ions (*Kivelson and Russell*, 1995). Also, neutral species can be found at a temperature higher than could be predicted by local ionization rates (*Fontenla et al.*, 1991).

A proper treatment of the radiative loss curve requires delicate energy balance calculations that include the effects of radiative transfer that include opacity, ambipolar diffusion and mass motions. Fortunately, this daunting task is tackled by Fontela, Avrett, and Loeser

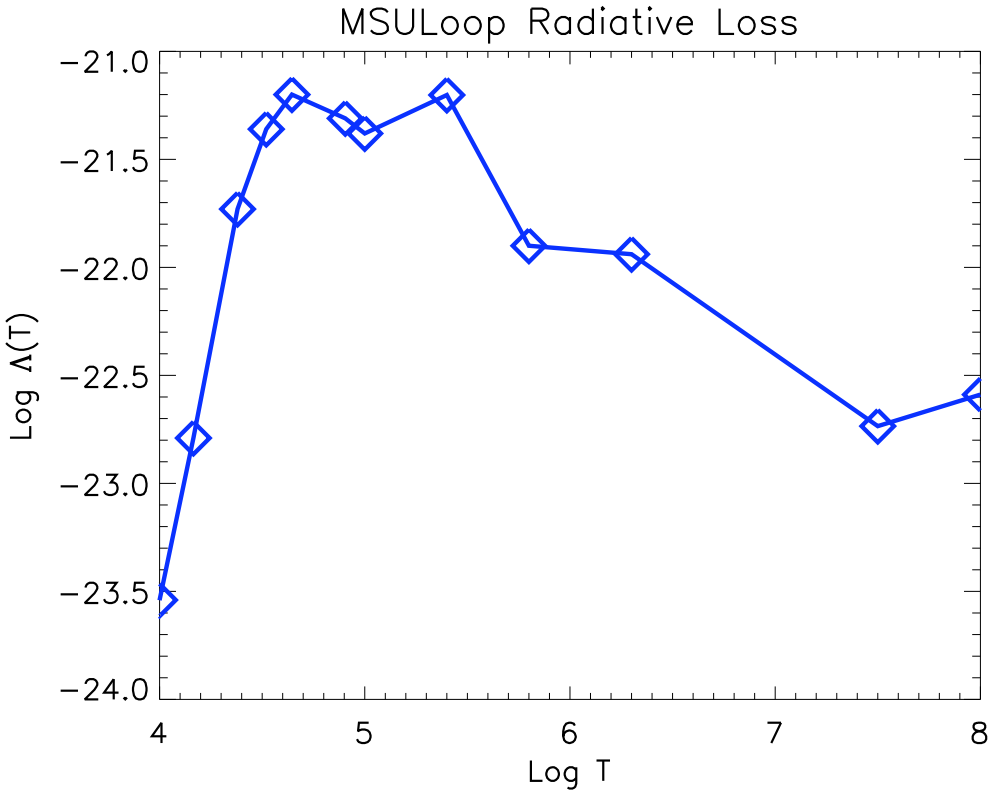

Figure 2.2: The radiative loss function as used by the MSULOOP code for the current set of experiments. The diamonds represent data points and the line shows interpolated values.

(1991, hereafter FAL) who published the radiative loss rates and conductive fluxes for a solar plasma that includes the previously mentioned effects. The first use of these improved radiative loss rates in a numerical loop model was by HYLOOP's predecessor as described in *Kankelborg and Longcope* (1999). The results from Eq. (2.24) and the corrections from FAL are tabulated as a piecewise continuous function of temperature and saved as a system variable that all programs can access and then interpolated for each temperature calculated on the volume grid. The total radiative loss curve for the experiments conducted in this work is shown in figure 2.2.

Radiative Loss Time Scale In order to choose the most effective method of dealing with equations numerically, it is often instructive to examine their characteristic time scales. To do this, the energy equation, Eq. (2.21) is rewritten using the equation of state to put the right hand side in terms of temperature instead of internal energy. All left hand side terms are set to zero except for the radiative loss term, in the form of Eq. (2.24) yielding

$$\frac{\partial T}{\partial t} \approx \frac{n_e \Lambda_{Rad}(T)}{3k_B}. \tag{2.25}$$

Rearranging Eq. (2.25) produces the following estimation of the radiative cooling time, in seconds at a given temperature, T_0,

$$\tau_{Rad} \approx T_0 \frac{3k_B}{n_e \Lambda_{Rad}(T_0)}. \tag{2.26}$$

A flare plasma with $n_e = 10^9\, cm^{-3}$, and $T_0 = 10^7\, K$ yields a radiative cooling time of $\tau_{Rad} \approx 1.1 \times 10^5\, s$. Since this time scale is orders of magnitude larger that any of the temporal grid scales, $\Delta_P t, \Delta_R t, \Delta_g t, \Delta_C t$, it is determined that this term could be handled by a single step Euler's method which is only first order accurate but computationally inexpensive (*Press*, 2002).

Notes on Radiative Losses For more complete treatments on the calculation Eq. (2.24) the interested reader is encouraged to review *Jefferies et al.* (1972), *Rybicki and Lightman* (1986), and *Landi and Landini* (1999). It should also be mentioned that all of the radiative loss equations for the corona are calculated under the assumption of *local thermal equilibrium* (LTE), where matter is in thermal equilibrium with itself if not adjacent cells or the radiation it emits and in a state of *ionization equilibrium*. For the corona, ionization equilibrium means that collisional ionization rates have come to equilibrium with radiative

and dielectric recombination rates *Aschwanden* (2005). However, it has been shown that in cases of rapid heating, such as flares, or rapid cooling, the ionization equilibrium assumption is not a good one (*Bradshaw and Mason*, 2003). Since these non-equilibrium effects have a minimal impact on spectrum averaged radiative loss rates and therefore the evolution of the thermal plasma (*Klimchuk*, 2006), they are ignored for now. This does limit the current study to only using spectrally averaged quantities as observable outputs.

Conduction

Many loop simulation models use the the pioneering works of *Cohen et al.* (1950) and *Spitzer and Härm* (1953) to calculate the transport of heat in a plasma due to conduction. The classical expression for heat flux, referred to as the Sptizer-Härm heat flux is given by

$$\mathbf{F_{SH}} = -\beta_{SH}\mathbf{E} - K_{SH}\nabla T \tag{2.27}$$

where β_{SH} and K_{SH} are diffusion coefficients (*Spitzer and Härm*, 1953). These coefficients were calculated by numerically solving Bolzmann's equation, Eq. (2.2), using the following definition of the distribution function

$$f_a = f_a^{(0)} + f_a^{(1)} \tag{2.28}$$

where $f_a^{(0)}$ is the Maxwellian distribution of species a and $f_a^{(1)}$ is a small perturbation. In order to make the solution tractable, it is assumed that the plasma is in a steady state, with no systematic flows and that terms of order $(\Delta v)^2$ and above could be neglected (*Cohen et al.*, 1950).

The magnitude of K_{SH} depends strongly on the maximum distance at which particles can interact (*Cohen et al.*, 1950). The magnetic field of the plasma under investigation

imposes two drastically different length scales for particle interaction. Along the magnetic field the length scale is the mean free path of the particle. Perpendicular to the magnetic field particles are constrained to interact on spatial scales smaller than the gyro-radius of the particle, which is orders of magnitude less that the mean free path. For this reason, the perpendicular component of conductive heat transport is neglected. The assumptions of an ideal plasma means that any electric fields are quickly quenched by the free movement of electrons. Therefore, the first term of Eq. (2.27) is also eliminated from consideration here. This gives the following familiar form of the conductive flux parallel to the guiding magnetic field

$$F_0 = -\kappa_{\|} \bigtriangledown_{\|} T \; erg\, cm^{-2}\, s^{-1}, \tag{2.29}$$

where $\kappa_{\|}$ is the Sptizer-Härm conductivity for electrons which account for almost all of the field aligned heat flux due to their much higher mobility (*Rosner et al.*, 1986) and is found to be

$$\kappa_{\|} = 10^{-6} T^{\frac{5}{2}}. \tag{2.30}$$

Saturated Flux Limitation Equation (2.29) can grow without bounds as $\bigtriangledown_{\|} T$ becomes large. This is obviously unphysical since at some point the energy carrying electrons will be depleted and the conductive flux will be saturated. Equation (2.29) is a first order approximation whose validity critically depends upon the assumption that the local distribution is only slightly skewed from a Maxwellian. As stated on page 22, this is equivalent to $\lambda_{mfp} \ll \min[L_T, L_{n_e}]$, where L_T and L_{n_e} are the characteristic scale lengths of temperature and density respectively as described in section 2 (*Rosner et al.*, 1986). For flares this is usually not a good assumption. The heating in flares can be highly localized and transient. High temperature tails from hot distributions stream into colder cells skewing them from

their Maxwellian distribution before they have the chance to collide and thermalize.

The work of *Matte and Virmont* (1982) accounted for deviations from Sptizer-Härm conductivity. In this work the authors constructed a plasma slab divided into two regions at T_1 & T_2 and the walls bounding the slab are held at a constant temperature. Heat flow between the two regions is determined by solving the Vlasov Equation with Fokker-Planck collision operators. The distribution function was expanded into spherical harmonics and each term was integrated separately. They found that if the length of the slab is large, $l_0 \sim 165\,\overline{\lambda}_{mfp}$ where $\overline{\lambda}_{mfp}$ is the mean free path of an electron of energy $\frac{3}{2}k_b\frac{T_1+T_2}{2}$, that the results agreed with *Spitzer and Härm* (1953) to within 3%. However, as the length of the slab shrank in relation to $\overline{\lambda}_{mfp}$ the *Spitzer and Härm* (1953) formulation overestimated the amount of thermal conduction. The percent difference between *Matte and Virmont* (1982) and *Spitzer and Härm* (1953) grew past 20% at $l_0 \sim 0.6\,\overline{\lambda}_{mfp}$. *Rosner et al.* (1986) fitted these results to a simple power law expression of the form

$$F_C \approx 0.11 \left(\frac{\lambda_{mfp}}{L_T}\right)^{-0.36} F_0. \tag{2.31}$$

In order to integrate these findings into the hydrodynamic codes the minimum value of the conductive flux, $\min[F_C, F_0]$, is used to describe the heat transfer between each volume cell. This correction is only applied where $T > 10^5\,K$. As in section 2 the effects of optical depth and ambipolar diffusion at $T \leq 10^5\,K$ are tabulated as a function of temperature from *Fontenla et al.* (1990) and used as corrections for Eq. (2.30) in that regime.

Conduction Time Scale As in section 2 the equation for the change of internal energy in a single grid cell due to thermal conduction is examined by defining a characteristic time scale using

$$\frac{\partial T}{\partial t} \approx \left(3 n_e k_B\right)^{-1} \frac{\partial}{\partial s}\left(\kappa \frac{\partial T}{\partial s}\right), \tag{2.32}$$

where the additional simplification of $\partial A/\partial s \approx 0$ is made. It is assumed that the temperature gradient can be expressed as $\partial T/\partial s \approx T_0/L_0$, where T_0 is the temperature in a cell and L_0 is a length scale, taken to be the size of the cell in this case. Using the numerical values of $\kappa_{\|}$ and k_B the conductive cooling time can be estimated as

$$\tau_{cond} \approx 4.14 \times 10^{-10} \frac{n_e L_0^2}{T_0^{5/2}} \left[sec\right]. \tag{2.33}$$

Considering the average grid length used in the current simulations of $\sim 80\,km$, and assuming a density of $n_e \sim 10^9\,cm^{-3}$ and a flare temperature of $T = 10^7\,K$ produces a conductive cooling time of $\tau_{cond} = 8.38 \times 10^{-5}\,sec$. The criterion for stability of an explicit solution for a diffusion equation gives a time step of $0.5\tau_{cond}$ (*Press*, 2002). Such a small time scale makes a stable, explicit scheme too computationally expensive. Therefore, MSULOOP uses an *implicit scheme* to solve for thermal conduction. Implicit schemes evaluate functions, either wholly or partially, at the end of the time step instead of the beginning. These schemes have the advantage of being stable for any time step at the price of some accuracy. See Appendix B for a full derivation of the numerical scheme used to calculate conduction effects.

Tests

Ensuring that MSULOOP could handle the highly dynamic plasma that occurs in flares necessitated extensive modifications from the previous version used in *Kankelborg and Longcope* (1999). These modifications required that the new code be re-tested in order to prove that the new simulations have a measure of validity. In order to test the code

the numerical results were compared to the analytical results. *Martens* (2008) derives the analytical temperature and pressure profile solutions for a power law heating function of the form

$$E_H(s) = HP^{\beta_H}(s)\,T^{\alpha_H}(s), \tag{2.34}$$

where H is a flux dependent constant and α_H and β_H are free parameters. *Martens* (2008) also derives the normalized temperature profile of a loop heated with arbitrary values of α_H and β_H. A simulation of a semi-circular loop of constant cross-section is run with Eq. (2.34) inserted into MSULOOP's energy equation, with $\alpha_H = \beta_H = 0$, corresponding to a uniform heating case. The simulation is allowed to continue until the system comes to equilibrium which is defined by $\max[\mathbf{V}(s)] \leq 1\,km\,s^{-1}$. Figure 2.3 shows the comparison of the normalized, analytical and numerical temperature profiles with a simulation that does not take into account the effect of saturated conductive flux. The fit is quite good throughout the loop with a percent difference $\leq 2\%$ for most of the length of the loop. Differences were higher at the footpoints of the loop. This is expected due to the modifications in the chromospheric radiation model and conductive flux. Also, since the temperatures are normalized, the divisor in the percent difference approaches zero, magnifying small differences.

Nonthermal Particle Transport

This section describes the modeling of the nonthermal particles' collisions upon the thermal plasma. There are many phenomena that can affect a particle's trajectory and energy as it travels through a plasma. Wave-particle interactions can be responsible for accelerating particles to super-thermal velocities in astrophysical plasmas under certain conditions (*Park and Petrosian*, 1996; *Fletcher and Hudson*, 2008). If the injected beam of electrons generates a significant current then a reverse current must form to neutralize it

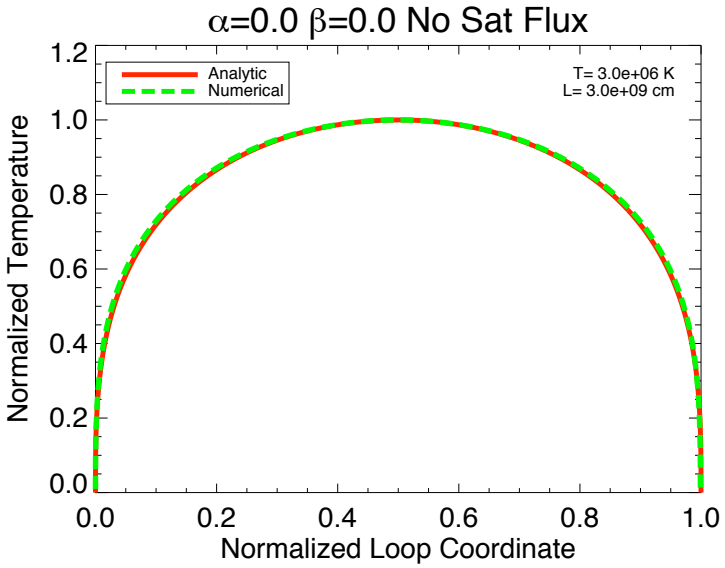

Figure 2.3: A plot showing the normalized temperature profile for a uniformly heated loop. The red line shows the analytic solution based on (*Martens*, 2008) and the green dashed line shows the result from MSULOOP. In this simulation saturated flux effects are not taken into account. The percent differences between the numerical and are less than 2%.

(*Tandberg-Hanssen and Emslie*, 1988). This reverse current will not only serve to decelerate the electrons in the beam but can also change their pitch-angle distribution, where the pitch-angle is defined by

$$\alpha_{PA} \equiv \arccos\left(\frac{v_z}{v_\perp}\right), \tag{2.35}$$

where v_z is the component of the particle's velocity parallel to the magnetic field and $v_\perp$ is the perpendicular component. It is beyond the scope of this work to model all effects on particle transport and other state of the art codes also neglect these effects (*Klimchuk et al.*, 2007). The codes developed will only deal with Coulomb scattering and the effects of non-uniform magnetic fields. The modeling of other processes that affect nonthermal particle evolution are left to further iterations of the code.

Stochastic Simulation

Much time was spent in determining the appropriate way to numerically treat the evolution of the nonthermal particle distribution. The method had to be highly adaptable, allowing for any conceivable initial distribution of particles and for the inclusion of additional terms in the evolution equations as additional physical operators were tested. Any code was also constrained to run on modest computer resources as large scale computing facilities were unavailable at a typical university setting. Lastly, if the code was to be used in testing the effects of different particle accelerators, then a meaningful measurement of error on each simulation would be needed. Describing the distribution in terms of macroscopic state variables is obviously inappropriate. This can be easily understood by considering a nonthermal beam being injected into a flaring loop. If each particle had an equal probability of streaming parallel or anti-parallel to the loop axis, then Eq. (2.13) would yield a bulk velocity of zero, which is clearly not descriptive.

Fokker-Planck (FP) methods were initially investigated. FP methods integrate the dis-

tribution function over a function, $P(\mathbf{v},\Delta\mathbf{v})$ that describes the probability that a particle will change its velocity $\mathbf{v}$ to $\mathbf{v}+\Delta\mathbf{v}$ to yield

$$f(\mathbf{x},\mathbf{v},t) = \int f(\mathbf{x},\mathbf{v}-\Delta\mathbf{v},t)\,P(\mathbf{v}-\Delta\mathbf{v})\,d^3\Delta v. \tag{2.36}$$

The product of fP is expanded into a power series with each term integrated separately. Fokker-Planck equations are notorious difficult to solve, and require the use of approximation schemes that average over individual particle effects and thus have the same difficulty as using macroscopic variables (*MacKinnon and Craig*, 1991). Therefore, this method was rejected.

It was decided to use a *Monte Carlo method* to treat the evolution of the nonthermal distribution. Some authors make a sharp devision between the definitions of *stochastic simulation* and Monte Carlo methods, reserving Monte Carlo (MC) to only refer to MC integration and MC Tests, and leaving stochastic simulation to describe the wide range of techniques that approximate average values by taking repeated sampling of functions of random variables (*Ripley*, 1987). The differences between these two definitions seem minor and the techniques used in both are similar if not identical. However, the term stochastic simulation will be used throughout this work to describe the methods of determining the evolution of the nonthermal particles since there are random (stochastic) terms in the equations. This method has the advantage of being able to treat the evolution of any arbitrary set of particles as long as the initial distribution is known (*MacKinnon and Craig*, 1991). The weakness of this approach is that stochastic simulations can become computationally expensive as will be shown later.

In PATC the nonthermal distribution is treated as a series of test particles. The evolution of these particles are tracked as they propagate through a thermal plasma. The test particles are randomly drawn from probability distributions designed to represent the physics of a

particular type of nonthermal beam. Since the test particles are drawn randomly and there are stochastic terms in the governing equations, each run of the code is expected to vary somewhat from every other run. Therefore, the value of some experimental quantity Q is estimated over multiple runs. Formally, this *Monte Carlo estimator* is defined as

$$\langle Q \rangle_{MC} \equiv \frac{1}{N_R} \sum_{i=1}^{N_R} Q_i \tag{2.37}$$

where Q_i is the value determined on the i^{th} run and N_R is the number of runs carried out, each time with nonthermal test particles redrawn from their random probability distributions. The *Law of Large Numbers* guarantees that the Monte Carlo estimator, which is essentially a sample mean, will approach the true value as $N_R \rightarrow \infty$ (*Krauth*, 1996; *Murthy*, 2001a; *Riley et al.*, 2002a). The use of a Monte Carlo estimator leads to a simple definition of the statistical error. The standard deviation is defined as the square root of the bias-corrected variance as given by

$$s_{QN-1} = \sqrt{\frac{1}{N_R - 1} \sum_{i=1}^{N_R} \left(Q_i - \langle Q \rangle_{MC}\right)^2}, \tag{2.38}$$

(*Riley et al.*, 2002b; *Murthy*, 2001a). It is clear from equations (2.37) and (2.38) that the true variable value can be approximated to chosen, finite accuracy by using a finite number of runs, N_R. The standard deviation of this sample average can be determined as a function of space and time and used as a lower bound estimate of the error in a simulation. Throughout this work the number of repeated trials used to reduce the standard deviation of an MC estimator is referred to as a *run*. A collection of runs gathered together to make an MC estimate is called a *simulation*.

The standard deviation of a stochastic simulation scales as $\propto N_{TP}^{-1/2}$ where N_{TP} is the number of test particles used in the simulation, or $\propto N_{TP}^{-1}$ through the use of specifically de-

signed semi-random sequences or importance sampling techniques (*Murthy*, 2001a; *Press*, 2002). Therefore, it is possible to reduce the absolute error to some arbitrarily small value by increasing the value of N_{TP} either by increasing the number of test particles per run or by increasing the number of runs (N_R). In order to keep computer time to a minimum $\sim 2 \times 10^4$ test particles are used per run. Since each individual run is independent, a *grid computing* parallelization technique is used. Grid computing initiates runs on multiple computers simultaneously, and combines the results of each run at the end of the simulation. This allowed for increased accuracy using multiple, moderate computing systems instead of a single super computing system.

Coulomb Scattering.

Coulomb or *Rutherford scattering* is a special case of a two particle collision that is elastic in the center of mass reference frame. The equations governing the kinematics of such collisions are well known and treated in depth in many textbooks and articles (Eg. *Cohen et al.*, 1950; *Tandberg-Hanssen and Emslie*, 1988; *Thornton and Marion*, 1995). This work exclusively deals with only mildly relativistic particles ($1 \leq \gamma \leq 1.39$) so relativistic effects will be ignored for the time being.

Consider a test particle of mass m, charge ze, where esu units are used to describe the electric charge and velocity v along the x-axis, incident upon a target particle with mass M, charge Ze, shown in figure 2.4. The *Rutherford scattering formula* shows that the particle will be scattered by an angle ψ_{com} in the center of mass frame equal to

$$\psi_{com} = 2 \cdot \arctan\left(\frac{Zze^2}{\mu_{rm} b v^2}\right) \tag{2.39}$$

where $\mu_{rm} = \frac{Mm}{M+m}$ is the reduced mass of the system, and b is the impact parameter which is the perpendicular distance of closest approach from the test particle's original path from

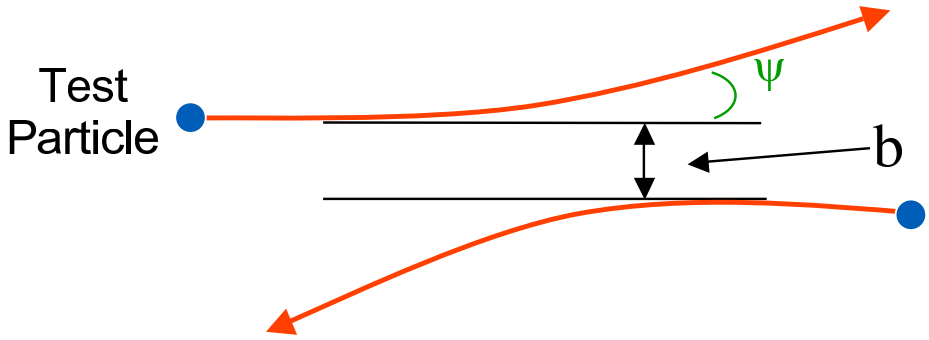

Figure 2.4: A diagram showing the interaction of two particles. The impact parameter, b, is defined as the distance of closest approach between the test and field particle.

the target particle if no forces were present (*Emslie*, 1978; *Bai*, 1982; *Tandberg-Hanssen and Emslie*, 1988).

Equation (2.39) is used to derive a change of energy and parallel velocity of the test particle. In the center of mass frame the initial and final velocity vectors are

$$\begin{aligned} v_{com\,i} &= \tfrac{M v_{total}}{m+M}\left(1\widehat{\parallel}+0\widehat{\perp}\right) \\ v_{com\,f} &= \tfrac{M v_{total}}{m+M}\left(\cos(\psi)\,\widehat{\parallel}+\sin(\psi)\,\widehat{\perp}\right) \end{aligned} \tag{2.40}$$

where $\hat{\parallel}$ and $\hat{\perp}$denote the directions parallel and perpendicular to the test particle's initial velocity vector. These equations are transformed to the collision frame to yield

$$\begin{aligned} v_{coll\,i} &= v_{total}\left(1\widehat{\parallel}+0\widehat{\perp}\right) \\ v_{coll\,f} &= \tfrac{v_{total}}{m+M}\left(M\cos(\psi)+m\,\widehat{\parallel}+M\sin(\psi)\,\widehat{\perp}\right). \end{aligned} \tag{2.41}$$

Now it is possible to derive equations for the change in energy and the velocity parallel to the test particle's initial path by noting that $\Delta E = \frac{1}{2}m\left(v_f^2 - v_i^2\right)$ and $\Delta v_{coll\parallel} = v_{coll\,f} - v_{coll\,i}$ and inserting Eqs. (2.41) to yield,

$$\Delta E = \frac{-m^2 M}{(M+m)^2} v_{total}^2 \left[1-\cos(\psi)\right] \tag{2.42}$$

$$\Delta v_{coll\,\|} = \frac{-M}{M+m} v_{total}^2 \left[1 - \cos\left(\psi\right)\right]. \tag{2.43}$$

Note that equation (2.43) is in the collision frame and requires another transformation to the loop frame in order to determine how a collision will affect the pitch-angle of the particle in the loop's frame of reference. This is a simple coordinate transformation that is carried out via a rotation matrix. Since, in the collision frame, all of the test particle's velocity is in the parallel direction, the angle between $v_{\|}$ in the loop frame and $v_{coll\,\|}$ in the collision frame is simply the pitch-angle, α_{PA}. This makes the non-relativistic matrix to rotate from the collision frame to the loop frame

$$\begin{pmatrix} cos\left(-\alpha_{PA}\right) & sin\left(-\alpha_{PA}\right) \\ -sin\left(-\alpha_{PA}\right) & cos\left(-\alpha_{PA}\right) \end{pmatrix}. \tag{2.44}$$

There is a 90^o ambiguity in 2.43 corresponding to whether or not the test particle approaching the field particle from "above" or "below". This allows for the introduction of a normally distributed random variable to resolve the ambiguity.

Close Collisions Only collisions with a small impact parameter will change a nonthermal particle's velocity appreciably in a single collision. Remembering the equation for the deflection angle Eq. (2.39), it can be shown that as the value of the impact parameter rises it will eventually reaches a value so that ψ_{com} becomes small enough for the computer to assign $\cos\left(\psi_{com}\right) = 1$ even though analytically it is close to, but not equal to one. This means that the computer would assign $\Delta E = \Delta v_{\|} = 0$ in accordance to Eqs. (2.42) and (2.43) even though a collision occurred. Collisions with an impact parameter smaller than this limiting impact parameter, b_{limit}, were labeled *close collisions*.

In order determine the value of b_{limit} the program *get_b_limit.pro* was written. This program uses an iterative method to determine the maximum value of ψ_{com}. This angle is

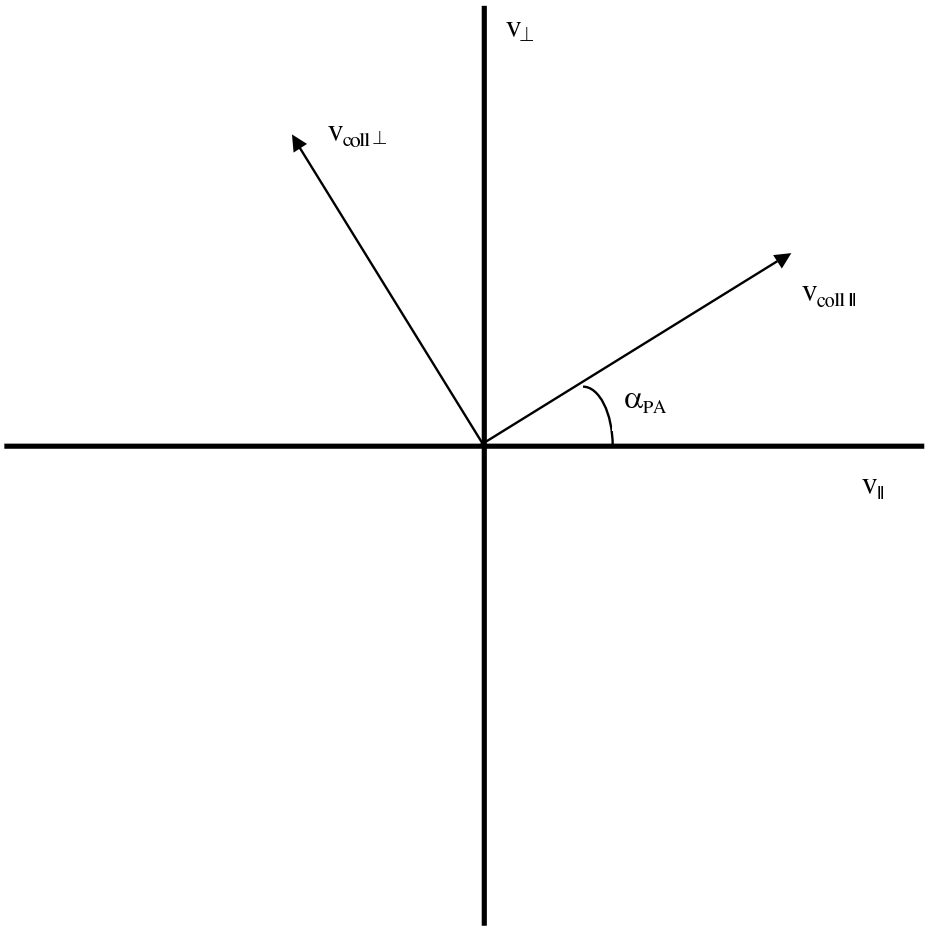

Figure 2.5: A simple diagram showing the relationship between the collision frame and the loop frame.

then related to b_{limit} by rearranging Eq. (2.39), using the assumption that $\arctan(\theta) \approx \theta$. This gives

$$b_{limit} = \frac{2Zze^2}{\mu_{rm}\psi_{max}v^2}. \tag{2.45}$$

For an electron-electron encounter the values of b_{limit} were tabulated for an array of electron energies. The values for a $15\,keV$ and $200\,keV$ particle were $b_{limit,15} = 1.87 \times 10^{-3}\,cm$ and $b_{limit,200} = 2.18 \times 10^{-4}\,cm$, respectively.

Now that an upper bound for close collision impact parameters has been set a lower bound needs to be decided upon. The validity of Eq. (2.39) breaks down as ψ_{coll} approaches $90°$. This critical impact parameter, b_{crit}, occurs when the energy of the Coulomb potential, $\frac{Zze^2}{r}$ in esu, with r being the distance between the two charges, is twice the kinetic energy of the particle (*Benz*, 1993a). This is written as

$$b_{crit} = \frac{Zze^2}{mv^2}. \tag{2.46}$$

The critical impact parameter for a $15\,keV$ and $200\,keV$ particle are $b_{crit,15} = 9.60 \times 10^{-12}\,cm$ and $b_{crit,200} = 7.20 \times 10^{-13}\,cm$, respectively

The impact parameter for each collision would seem a natural choice for a random variable. A probability distribution for b must be defined in order to create a random sample. Following the works of *Tandberg-Hanssen and Emslie* (1988) and *Parks* (2004) an impact parameter distribution function that is uniform in area is chosen, which is written as

$$f(b)\,db = 2\pi b db. \tag{2.47}$$

Using the condition that the integral over all possible probabilities has to be one, the distribution function is integrated from zero to b_{max} in order to get the normalization factor, $A_c = (\pi b_{max}^2)^{-1}$ which converts the distribution function into a normalized probability den-

sity $p(b)$. It is possible to create a distribution of random numbers based upon the probability density using the *transformational method of uniform deviates (Press, 2002)* also known as the *direct inversion technique (Murthy, 2001b).* This method involves calculating the *cumulative probability distribution* of the probability density in question, Eq. 2.47. For an arbitrary probability density function the cumulative distribution function is given by

$$F(x) = \int_{-\infty}^{x} p\left(x'\right) dx', \tag{2.48}$$

where x' is the dummy variable of integration. The function $F(x)$ provides a map from the original probability function to a uniform deviate space. Inverting Eq. (2.48) maps a set of uniform deviates back to the original probability density function,

$$x = F^{-1}\left(\mathscr{N}_{\mathscr{U}}\right) \tag{2.49}$$

where $\mathscr{N}_U$ is a random number picked from a uniform distribution of deviates and F^{-1} is the inverse of the function F. Using the above prescription, a set of impact parameters is randomly drawn using the formula

$$b = b_{max}\sqrt{\mathscr{N}_{\mathscr{U}}}. \tag{2.50}$$

Using Eq. (2.47) and the typical values for a flare , $n_e = 10^9\, cm^{-3}$, $T = 10^7\, K$, and setting $b_{max} = b_{Debye}$ it is found that the probability of a $15\, keV$ particle undergoing a close collision is $\approx 8.78 \times 10^{-5}$ and $\approx 1.19 \times 10^{-6}$ for a $200\, keV$ particle. Due to these extremely low probabilities and the computational power required to handle single particle collisions, PATC's close collision model for the experiments in this study is turned off and $b_{limit} = b_{crit}$ for future integrals. Thus, all collisions are treated as far collisions for this experiment. This has the effect of averaging over any possible extreme changes in the test particles' energy

and pitch-angle. This module is included in PATC for future use in the investigation of plasmas where they may play a more important factor.

Far Collisions The effect of an individual collision with an impact parameter greater than b_{limit} is negligible by itself. However, the cumulative effect of numerous far collisions can produce a measurable effect. For these collisions PATC calculates the average rate of change of a quantity Q by using Eq. (2.11) over the distribution function defined by Eq. (2.47) over a flux of target particles nv. For any given quantity, Q, the formula for calculating the average rate of change is then

$$\left\langle \frac{\partial Q}{\partial t} \right\rangle = 2\pi nv \int \triangle Q \cdot bdb \tag{2.51}$$

where ΔQ is the change in Q as a function of b. Using the equation for the change in energy, Eq. (2.42), and for ψ_{com}, Eq. (2.39) yields

$$\left\langle \frac{\partial E}{\partial t} \right\rangle = 2\pi n \frac{-m^2 M}{(M+m)^2} v^3 \int_{b_{limit}}^{b_{Debye}} \left[1 - \cos\left(2 \cdot \arctan\left(\frac{Zze^2}{\mu_{rm} b v^2} \right) \right) \right] \cdot bdb \tag{2.52}$$

and

$$\left\langle \frac{\partial v}{\partial t} \right\rangle = 2\pi n \frac{-M}{M+m} v^2 \int_{b_{limit}}^{b_{Debye}} \left[1 - \cos\left(2 \cdot \arctan\left(\frac{Zze^2}{\mu_{rm} b v^2} \right) \right) \right] \cdot bdb. \tag{2.53}$$

It is noted that the integrands of Eqs. (2.52) and (2.53) are identical and is given by

$$\begin{aligned} \int_{b_{limit}}^{b_{Debye}} \left[1 - \cos\left(2 \cdot arctan\left(\frac{Zze^2}{\mu_{rm} b v^2} \right) \right) \right] \cdot bdb = \frac{1}{2} \left[\frac{Zze^2}{\mu_{rm} b v} \right]^2 \left[\ln\left(1 + \left[\frac{\mu_{rm} b_{Debye} v^2}{Zze^2} \right]^2 \right) \right. \\ \left. - \ln\left(1 + \left[\frac{\mu_{rm} b_{limit} v^2}{Zze^2} \right]^2 \right) \right] \end{aligned} . \tag{2.54}$$

Since b_{limit} has been previously defined so that $b_{limit} \equiv b_{crit} \simeq Zze^2/\mu v^2$, the last logarithmic expression on the right hand side of Eq. (2.54) is ~ 0.69 which is small compared to the other logarithmic term and is ignored. In order to make the equations more readable, the following definitions are made

$$\begin{aligned} \mu_{rmf} &\equiv \tfrac{mM_f}{m+M_f} \\ \zeta_f &\equiv \tfrac{zZ_f e^2}{\mu_{rmf} v^2} \\ \Xi_f &\equiv \mu_{rmf}\zeta_f^2 \ln\left(1+\left[\tfrac{b_{Debye}}{\zeta_f}\right]^2\right) \end{aligned}, \tag{2.55}$$

where the subscript f denotes values calculated for a general field particle that provides a target for a collision. Using the above definitions, the change of test particles' energy and parallel component of velocity is calculated as

$$\left\langle \tfrac{dE}{dt} \right\rangle = -4\pi n_e v^3 \left[\varsigma_1 \tfrac{\mu_{rme}}{m_e}\Xi_e + \varsigma_2 \tfrac{\mu_{rmp}}{m_p}\Xi_p\right] \tag{2.56}$$

$$\left\langle \frac{dv}{dt} \right\rangle = -\frac{4\pi n_e v^2}{m}\left[\varsigma_1\Xi_e + \varsigma_2\Xi_p\right], \tag{2.57}$$

Where a random variable ς_x has been introduced so that for a fully ionized target plasma consisting of electrons and protons, $\varsigma_1 = 1 + 0.0333\Re_N$ and $\varsigma_2 = 2 - \varsigma_1$, where $\Re_N$ is a random number drawn from a normal distribution. Since the plasma is neutral the number of proton collisions should, on average, equal the number of electron collisions and the definition of ς_1 assures this is true. The variation from this average should be very small and a numerical choice was made to have a 10% variation at the 3σ level. Note that this notation allows us to use a target plasma with as many constituent species as desired as long as $n_1\varsigma_1 + n_2\varsigma_2 + \ldots + n_N\varsigma_N = n$.

Collision Time Scales Again, to decide the appropriate numerical technique to handle these equations characteristic time scales of the equations are looked for. If electrons are chosen as test particles they will elastically collide off of the much more massive protons with a large deflection angle but a small exchange of overall kinetic energy. Likewise, electron-electron collisions will have a large kinetic energy exchange due to the equal masses. Therefore, definitions of an electron-proton deflection time, $\tau_{d(e-p)}$, and an electron-electron energy exchange time, $\tau_{\varepsilon(e-e)}$, are needed to characterize the time scales for collisions. The time scales are set by algebraically rearranging Eqs. (2.56) and (2.57) and using $E = \frac{1}{2}mv^2$ to yield

$$dt = -dE\left[\frac{m_e}{4\pi n_e v^3 \mu_{rme}\Xi_e}\right] \tag{2.58}$$

$$dt = -dv\left[\frac{m}{4\pi n_e v^2 \Xi_p}\right], \tag{2.59}$$

where the stochastic elements have been removed. The natural choice to make for dE and dv is to set them so that the initial values are reduced by a factor of e^{-1}. Since Eqs. (2.56) and (2.57) are only valid for small changes, a more conservative value is chosen so that the energy and velocity only change by a factor of 10%. With this definition chosen, the characteristic collisional time scales become

$$\tau_{\varepsilon(e-e)} \approx E_0\left[\frac{.1m_e}{4\pi n_e v^3 \mu_{rme}\Xi_e}\right] \tag{2.60}$$

$$\tau_{d(e-p)} \approx v_0\left[\frac{.1m}{4\pi n_e v^2 \Xi_p}\right] \tag{2.61}$$

where 0 subscripts denote initial values and the equal signs have been replaced since the infinitisimals are being treated as $\Delta's$. Again using typical values for the thermal plasma

density and temperature and calculating for a $15 keV$ particle, which will provide a lower bound, it is found that $\tau_{d(e-p)} \approx 0.6 sec$ and $\tau_{\varepsilon(e-e)} \approx 1.0 sec$. Since these time scales are comparable an explicit time stepping will be an adequate strategy.

The fact that there can be strong gradients in the target plasma's state variables in both space and time must also be taken into account. In order to account for the rapid spatial variations, the time step for collisions is set so that each particle samples the state variables within a grid cell before being allowed to move to the next. This time scale is represented by

$$\tau_{Sample} = \frac{\Delta_g s(i)}{v_{0\|} S_1} \tag{2.62}$$

where $v_{0\|}$ is the particle's parallel velocity at the beginning of the step, $\Delta_g s(i)$ is the length of the grid that the particle is in at the beginning of the step, and S_1 is a user set safety factor. Setting S_1 to 10 ensures that the particle adequately samples the cell and only moves into the next adjacent cell if the percent difference in cell sizes is kept to $< 10\%$.

Effects of a Nonuniform Magnetic Field

Consider a converging magnetic field in cylindrical coordinates with no ϕ component. Using the fact that $\bigtriangledown \cdot \mathbf{B} = 0$, a general expression for this field can be written as

$$\begin{array}{ll} \frac{1}{r}\frac{\partial}{\partial r}\left(rB(r)\right) & = -\frac{\partial B(z)}{\partial z} \\ B(r) & \approx \frac{-r}{2}\frac{\partial B(z)}{\partial z} \end{array}, \tag{2.63}$$

where the condition $\left(\frac{1}{B}\frac{\partial B(z)}{\partial z}\right)^{-1} \ll r$ has been used. The Lorentz force corresponding to the perpendicular component of the particle's velocity is

$$F_z = \frac{q}{c}\left(v_\perp \times B_r\right). \tag{2.64}$$

Now substituting (2.63) into (2.64) and substituting the gyro-radius, $r_B = mcv_\perp/qB$, for r gives

$$F_z = \frac{\partial m v_\parallel}{\partial t} = \frac{1}{2} m v_\perp \left(\frac{-1}{B} \frac{\partial B(z)}{\partial z} \right). \tag{2.65}$$

Equation (2.65) gives the rate of change of the particle's parallel momentum. The subsequent change in the particle's perpendicular momentum is given by the fact the magnetic field does no work upon the particle and by the relation $v_\perp = \sqrt{v_{total}^2 - v_\parallel^2}$.

PaTC Time Scales

Bai (1982) proposed a method of operator splitting that allowed for the partial differential equations as expressed by Eqs. (2.56), (2.57) and (2.65) to be treated as separate, ordinary differential equations in the limit of $d \ll L_B$, where d is the distance a particle is allowed to travel and L_B is the characteristic scale length of the magnetic field,

$$L_B = \left(\frac{1}{B} \frac{\partial B(z)}{\partial z} \right)^{-1}. \tag{2.66}$$

This condition is used to calculate a time scale for Eq. (2.65), so that

$$\tau_{F_z} = \frac{L_B}{v_{0\parallel} S_2}, \tag{2.67}$$

where $v_{0\parallel}$ is the particle's parallel velocity at the beginning of the step and S_2 is a user defined safety factor > 1 that is often set as a compromise between computing time and conservation of the magnetic moment. For runs in this study S_2 is set so that the magnetic moment is conserved to within $\ll 1\%$. Combining Eqs. (2.62), (2.67) yields the PATC time step

$$\Delta_P t = \min \left[\tau_{\varepsilon(e-e)}, \tau_{d(e-p)}, \tau_{Sample}, \tau_{F_z}, \frac{\Delta_C t}{2} \right]. \tag{2.68}$$

Now that the derivatives that describe the evolution of the nonthermal particles have been derived and the relevant time scales have been defined, a method of solving these equations must be decided upon. In order to conserve the particles' magnetic moments using an equation that does not explicitly do so, accuracy was favored over computing time. Equations (2.56), (2.57) and (2.65) are solved in tandem using an RK5 method. For details on the RK5 method used see Appendix 6.

Tests

Since PATC is a new code, it is necessary to perform a series of tests to determine if it is acting as expected. In order to do this the numerical results are compared to analytical approximations. In the first test, an approximation for the change of energy of a nonthermal particle is taken from *Tandberg-Hanssen and Emslie* (1988) of the form

$$\left\langle \frac{dE}{dt} \right\rangle = -\frac{C}{E} nv, \tag{2.69}$$

where n is the number of incident target particles and C is defined as

$$C \equiv 2\pi e^4 \ln \Lambda$$

with the Coulomb logarithm, $\ln \Lambda$, defined as the logarithm of the ratio of b_{Debye}/b_{crit}. Since the Coulomb logarithm is a weakly varying function, it is held at a constant value of 20 which is considered appropriate for the solar corona but is known to introduce a possible error of $\sim 10\%$ (*Tandberg-Hanssen and Emslie*, 1988). In order to test the numerical expression of the energy loss, PATC tracks test particles as they propagate through a cylindrical tube held at constant density and temperature. The change in the particle's energy as calculated by the analytical expression is compared to PATC's calculation at each

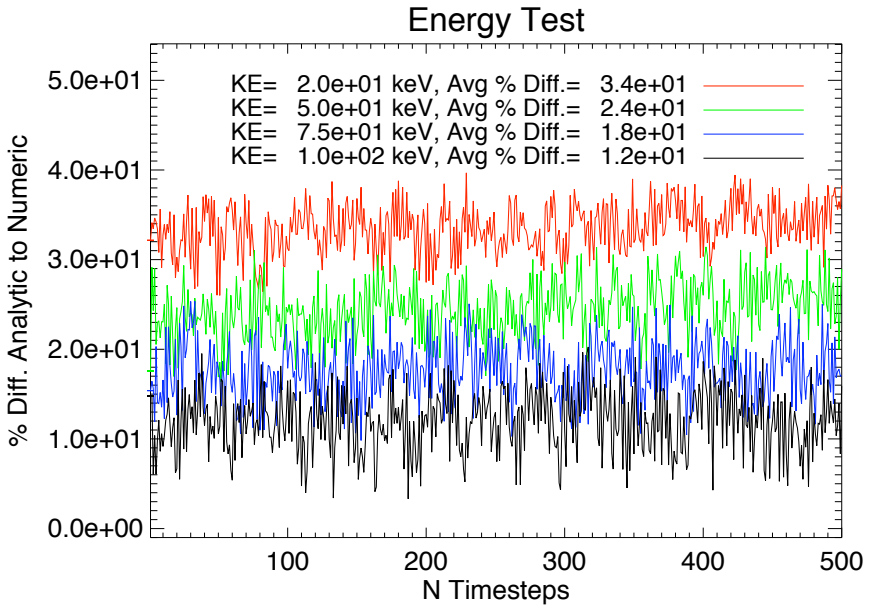

Figure 2.6: A plot showing the percent differences in PATC's calculation of the change in a particle's energy in a 0.0001 *second* time step and an analytic approximation to the energy change. The differences are interpreted as being caused by the numerical treatment's increased accuracy, since it uses fewer approximations than the analytic expression.

0.0001 *sec* time step. The percent difference between the analytical and numerical results are plotted in figure 2.6. Figure 2.7 plots the ratio between the analytic change in nonthermal particle energy to PATC's calculation of the energy change. The two methods differ by less than a factor of two for all times, which is considered to be a good agreement. The energy dependence in the percent difference and the ratio is due to the fact that at lower energies the test particle loses energy more rapidly making Eq. (2.69) less of an adequate approximation for a time step. PATC automatically determines the proper time step to integrate Eq. (2.56) via Eq. (2.68) yielding a more accurate result than a simple Eulerian step.

In the calculation of Eq. (2.65) no use is made of adiabatic invariants. However, if the formulations and numerical methods used to solve the equations are correct, in the absence

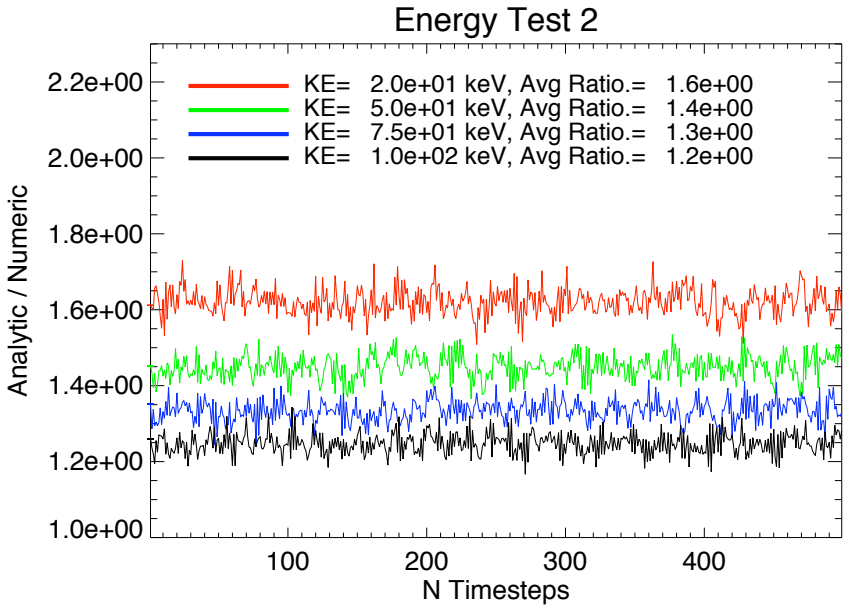

Figure 2.7: A plot showing the ratio of the analytic change in nonthermal particle energy to PATC's calculation of the energy change in a particle's energy in a 0.0001 *second* time step.

of collisions, these invariants should naturally be conserved. The magnetic moment is such an invariant and is given by

$$\mu_m = \frac{m^2 v_\perp^2}{B}, \tag{2.70}$$

where $v_\perp$ is the component of a particle's velocity perpendicular to the magnetic field. The mirror point of a particle is defined as the point in a magnetic trap where the all of the particle's momentum along the magnetic field is converted to perpendicular momentum. This is expressed as

$$\frac{m^2 v_{0\perp}^2}{B_0} = \frac{m^2 v_T^2}{B_{mp}}, \tag{2.71}$$

where the zero subscripts denote the values at the injection point and B_{mp} is the magnetic field at the mirror point. Equation (2.71) can be rearranged to solve for the mirror point to

yield

$$\begin{aligned} B_{mp} &= B_0 \frac{v_T^2}{v_{0\perp}^2} \\ &= B_0 \frac{1}{1-\cos^2(\alpha_{PA})} \end{aligned} \tag{2.72}$$

where α_{PA} is the pitch-angle as described in Eq. (2.35) and use of the identity $1-\cos^2\theta = \sin^2\theta$ has been used.

In order to test the conservation of the magnetic moment, a test loop with $n_e = 0$ is made with a magnetic field that decreases as an exponential function of height. Particles with varying pitch-angles are injected into the loop and tracked. The magnetic field in the location where the particles' parallel momentum changed sign B_{CS} is recorded and compared to Eq. (2.72). A percent difference is taken between B_{mp} and B_{CS} and plotted. The process is repeated for multiple energies. The results of this test is shown in figure 2.8. While there is some variation in the conservation of the magnetic moment, the percent difference is less that 0.02% for all times and pitch-angles and the average difference is $\leq 5.8 \times 10^{-17}$. Similar results are gained for particles of different energies. This test shows that PaTC can accurately simulate the effects of magnetic mirroring.

Emission Calculations

In order to compare numerical experiments with actual flares, the simulations provide synthesized images of the flaring loop in a wide range of the electromagnetic spectrum. In these experiments photon emissions are taken into account by calculating thermal and non-thermal bremsstrahlung radiation and the contribution of spectral line emission. Cyclotron radiation is ignored for now, but can be calculated for future experiments.

The thermal component of a flare's emission is calculated after the simulation of a flare. Using the CHIANTI database(*Dere et al.*, 1997; *Landi and Phillips*, 2006), synthetic spectra, in units of $photons\,cm^{-3}s^{-1}$, are calculated that include thermal bremsstrahlung

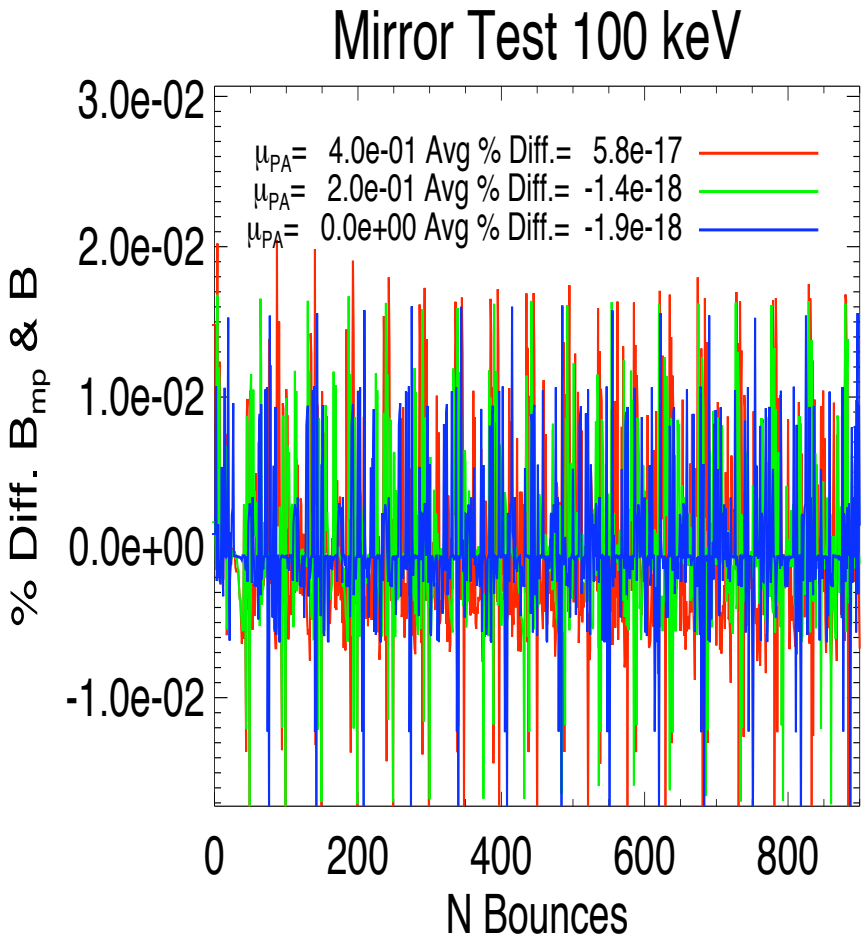

Figure 2.8: A plot showing the percent differences between an analytical calculation of the magnetic field strength where a test particle should mirror and the numerical calculation. The red, green, and blue lines represents a particle with a pitch-angle cosine of .4, .2, and one respectively.

and spectral lines for a wide range of electron densities and temperatures. After calculation, the spectra are stored in a database where they can be accessed as a function of temperature and density. After the simulation, the imaging software searches the database for the spectra corresponding to the temperature and density for each cell of the loop.

The nonthermal bremsstrahlung emission is calculated during the simulation by PATC as follows. At each $\Delta_P t$ the number of photons emitted per each grid cell is calculated via the following formula

$$I\left(\varepsilon_\gamma s,t\right)_B = n\left(s,t\right)\int_{\varepsilon_\gamma}^{\infty} f\left(s,t,E\right)v\left(E\right)\sigma_B\left(\varepsilon_\gamma,E\right)dE\ photons\,cm^{-2}s^{-1}keV^{-1}, \qquad (2.73)$$

where f is the distribution of nonthermal particles which is discretized in PATC, and ε_γ is the energy of the photon of interest. Relativistic effects have been ignored until now. Since the non-relativistic bremsstrahlung cross-section introduces a discrepancy of $\sim 20\%$ when compared to the relativistic form, the relativistic cross-section, $\sigma_B\left(\varepsilon_\gamma,E\right)$, is used in the calculation of nonthermal bremsstrahlung (*Haug*, 1997). The spectra are summed at every $\Delta_P t$ and output at every $\Delta_R t$.

Despite the use of a relativistic bremsstrahlung cross-section, relativistic beaming effects are ignored and the nonthermal bremsstrahlung emission is assumed to be isotropic. Even though the nonthermal particles are only mildly relativistic, this simplification requires some explanation. Relativistic beaming effects can strongly affect footpoint flare emission due to the Sun's albedo in hard X-rays. The solar photospheric reflectivity to x-rays has a broad hump from $10-100\,keV$ with a peak at $30-40\,keV$. At some viewing angles and energies the Sun's reflectivity can approach 100% (*Kontar et al.*, 2006). A beam of charged, relativistic particles preferentially emits bremsstrahlung radiation in the direction of its velocity vector (*Rybicki and Lightman*, 1986). This directed emission enhances the amount of HXR emission reflected from the photosphere. To minimize the error in-

volved in not considering the directivity of nonthermal bremsstrahlung emission and solar HXR albedo, the modeled flare loop is oriented 90° from the observer. This has the effect of making the scattered light due to reflection perpendicular to the observer's line of sight. Also, the analysis in this work will be restricted to loop top emission further avoiding the confusion of albedo effects. Directivity effects also affect the emission at the loop top. *Petrosian* (1973) calculated the emission per steradian of a beam of nonthermal particles, with and without directivity effects. He found that the ratio of the directed emission to the isotropic emission as seen by an observer perpendicular to the beam's velocity vector is ~ 1 for photon energies $< 21.5 keV$. With this in mind, the isotropic approximation is a good one for an on limb loop if the simulated emission of photons is kept to energies $\leq 20 keV$. These approximations have also been used with success in other flare modeling work (Eg. *Fletcher and Martens*, 1998a).

A suite of imaging software was devised to create realistic synthetic images from the HYLOOP simulations. For a given instrument and/or bandpass, a response as a function of wavelength is obtained using the SOLARSOFT database. The thermal spectra and nonthermal bremsstrahlung spectra are combined and convolved with the instrument response function to calculate a response per volume for each grid cell. The SHOW_LOOP imaging software, independently developed by the Montana State University Solar Group, determines the inclination angle of the loop relative to the observer and performs a path length integral along the line of sight in order to calculate a signal per unit area. The viewing area of each synthetic pixel on the Sun is then calculated to determine the total signal per pixel. If desired, the grid of synthetic pixels can then be convolved with a function (Eg. Gaussian, elliptical Gaussian, Airy, etc.) in order to simulate a position dependent point spread function of an instrument. This process can be repeated for a multitude of loops, called strands when they are sub-resolution, to build up a very realistic image.

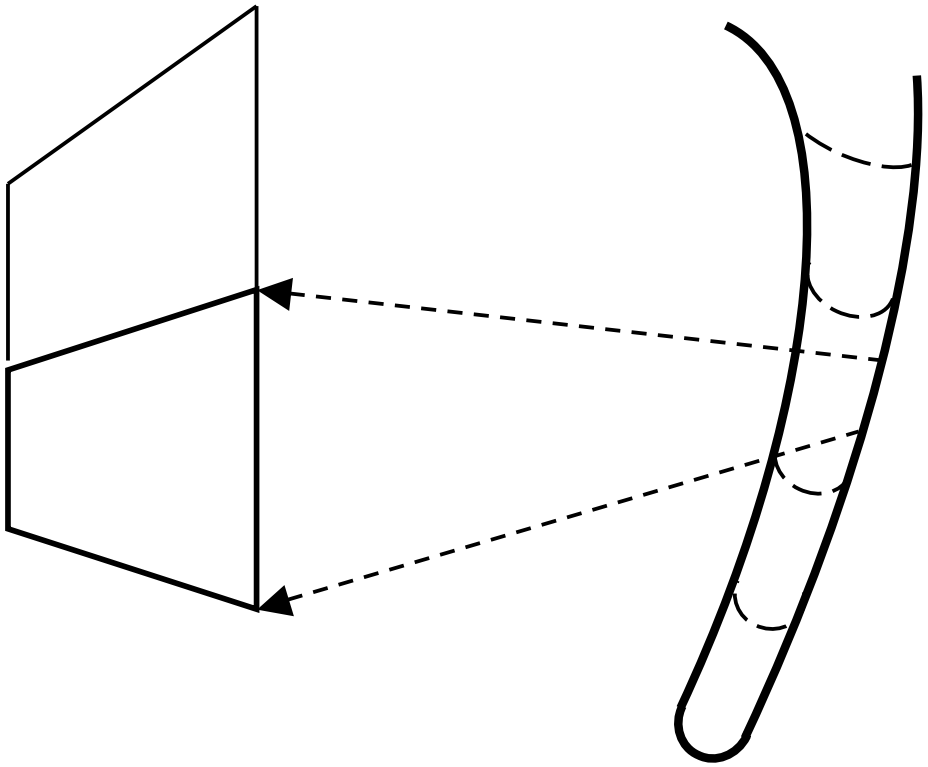

Figure 2.9: A diagram representing the calculation of instrument responses on an arbitrarily sized pixel grid. The SHOW_LOOP software performs a path length integration through the volume emission of a segment of the loop observed by a pixel. This combined with the area of the loop observed by the pixel provides a total signal from a loop of arbitrary inclination angle observed by pixel. Once the signal for the entire grid is computed, the grid can then by convolved with a function to take effects such as point spread functions, or defocus into account.

Figure 2.10: An image built up using multiple, simulated loops. The image on the far left shows a system of loop strands as would be viewed by the XRT instrument on *Hinode* in the Al-Poly channel with a $2''$ resolution. The center image shows the same system, in the same bandpass but with a $0.5''$ resolution. The last image shows the system in a theoretical bandpass for the *AIA* mission but with an increased resolution of $0.1''$.

CHAPTER 3

STATIC VERSUS DYNAMIC ATMOSPHERES

The previous chapters detailed the building of a suite of numerical simulation codes that combined nonthermal test particle tracking with a hydrodynamic plasma. However, it still remains to prove that the additional effort in combining these two effects was worth the programming time and extra computational expense. To this end, an experiment was designed to test the importance of combining hydrodynamics with nonthermal particles when simulating flare observables.

This experiment created two sets of simulations. One simulation set allowed the nonthermal particles to propagate through a plasma where all state variables were held constant. The other set of simulations allowed the nonthermal particles to interact with a dynamic plasma. Test variable outputs for both the the static and dynamic simulation had to be decided upon. One choice of test variable was hard X-ray emission in the $3-6\,keV$ bandpass. The thermal and nonthermal contributions to this bandpass could be calculated to gain insight into the relative importance of both mechanisms. Since the formation of looptop hard X-ray sources has remained a topic of debate in the literature, the analysis was focused on the apex region of the flare loop.

Before the experiments could be conducted, both sets of simulations required the definition of an initial post flare loop geometry and initial state of the thermal plasma. Also, the probability functions that determined the distributions of the nonthermal particles' energy, pitch angle and the point of injection into the loop had to be defined. Lastly, the errors due to the discrete nature of the nonthermal test particles and the model grids had to be quantified and analyzed before the results of the experiment could be analyzed and understood.

Experimental Setup

Loop Geometry

The experiments outlined by this thesis studied the effects of nonthermal electron beams accelerated by an electric field that was directly connected to the reconnection of magnetic field in a current sheet. A magnetic field model based upon a Y type current sheet in a potential magnetic field (*Priest and Forbes*, 2000b) was developed. This model was used to define the geometry for all experiments described within this document.

Much analytical work has been done on constructing tractable formalisms for flare loop magnetic geometries (see *Priest and Forbes*, 2000a for a review). Much work describes the magnetic fields as complex potentials, $F(x,y)$, of which the vector potential $A(x,y)$ is the real part (*Bungey and Priest*, 1995; *Priest and Forbes*, 2000a). The reason for this is that the real and imaginary parts of any analytic function of the complex variable Z, where $Z = u(x,y) + iv(x,y)$, are each solutions to Laplace's equation, $\bigtriangledown^2\phi = 0$. This method is made even more powerful by the fact that once a solution is found in a simple geometry further solutions for more complex geometries can be found by making conformal transformations (*Riley et al.* 2002b).

Bungey and Priest (1995) developed an elegant formalism using complex potentials that not only captures potential magnetic field configurations but also force free, $\mathbf{j} \times \mathbf{B} = 0$, configurations. For potential fields the flux function takes the following form,

$$F(Z) = B_0 \left[a^2 b \, ln \left(\frac{Z + \sqrt{Z^2 - a^2}}{a} \right) + 2ac\sqrt{Z^2 - a^2} - 2adiZ - \frac{1}{2} Z \sqrt{Z^2 - a^2} \right] \quad (3.1)$$

where, a is the half length of the current sheet, b, c, and d are dimensionless constants and $i = \sqrt{-1}$. The components of the magnetic field can be obtained by taking the derivative

of 3.1 with respect to Z to yield

$$\begin{aligned} B_x + iB_y &= -\frac{dF}{dZ} \\ &= -B_0 \left[\frac{ba^2+2acZ-Z^2+\frac{1}{2}a^2}{\sqrt{Z^2-a^2}} + 2adi \right]. \end{aligned} \tag{3.2}$$

In the special case of $b = \frac{1}{2}$, $c = d = 0$ yields the simplified expression

$$B_x + iB_y = \sqrt{Z^2 - a^2}, \tag{3.3}$$

which is the original solution found by *Green* (1965) and gives the magnetic field configuration around a current sheet of half length a ending in null points where the magnetic field vanishes. The magnetic field strength of such a configuration is shown in figure 3.1 and the magnetic field lines and current sheet are shown in figure 3.2. The above may seem to be more work than was necessary to re-derive the known expression 3.3. However, by doing the extra work the code now has a wide array of potential and force free magnetic geometries at its disposal by changing a small number of parameters.

A 3D representation of a post flare loop had to be constructed from the geometry previously defined in 2.5D, with the dimension coming into and out of the page being redundant. A characteristic field line, just below the separatrix surface, was taken to represent the axis of the post flare loop. This is shown in red in figure 3.2. Now a characteristic point was taken to measure the width of the loop. This point could be at the footpoints or apex depending upon what measurements were available if comparing to an observed loop. Each surface area, perpendicular to the field line, was assumed to be circular. In order to get the

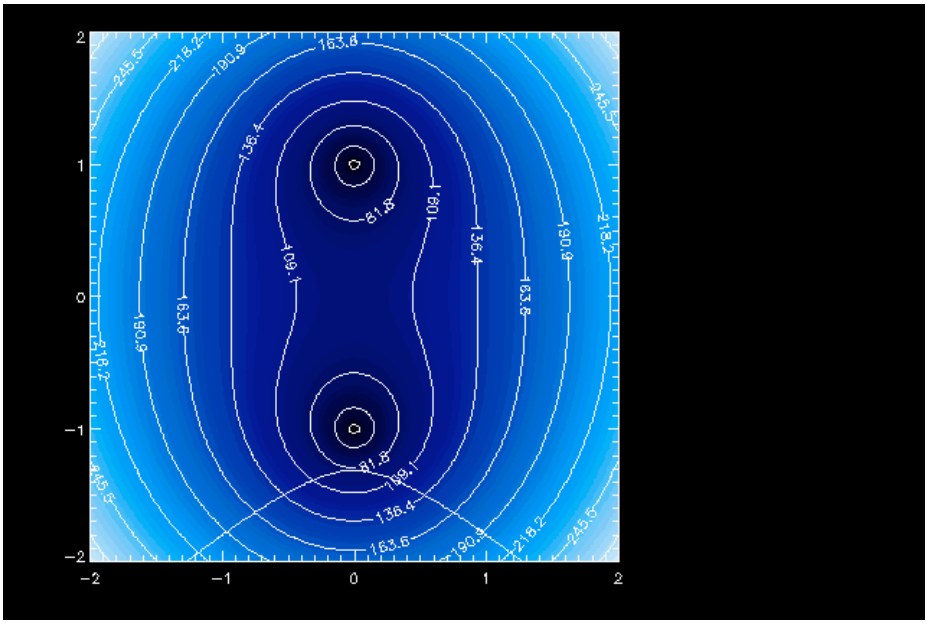

Figure 3.1: A contour map of the magnetic field generated by a *Green* (1965) style current sheet using the formalisms of *Bungey and Priest* (1995). Notice the two null points which are regions of zero magnetic field. The characteristic field line for the flare loop geometry is shown at bottom.

areas for the rest of the loop, the constant flux condition was used,

$$\phi_B = \int \mathbf{B} \cdot d\mathbf{a} = Constant. \tag{3.4}$$

to define the area everywhere via

$$A_n = \frac{A_O B_O}{B_n} \tag{3.5}$$

where the subscript O represents the point where the area was observed and n represents the nth surface grid. For this experiment, a loop radius of $2.1 \times 10^8\, cm$ was used at the loop apex. This is roughly the same radius that was used in the simulations by *Fletcher and Martens* (1998b). The x and y axes were scaled by a single constant to match the height of a typical flare loop. A height of $1.8 \times 10^9\, cm$ was chosen to match the work of *Fletcher and Martens* (1998b). Note that *Fletcher and Martens* (1998b) used the base of the corona

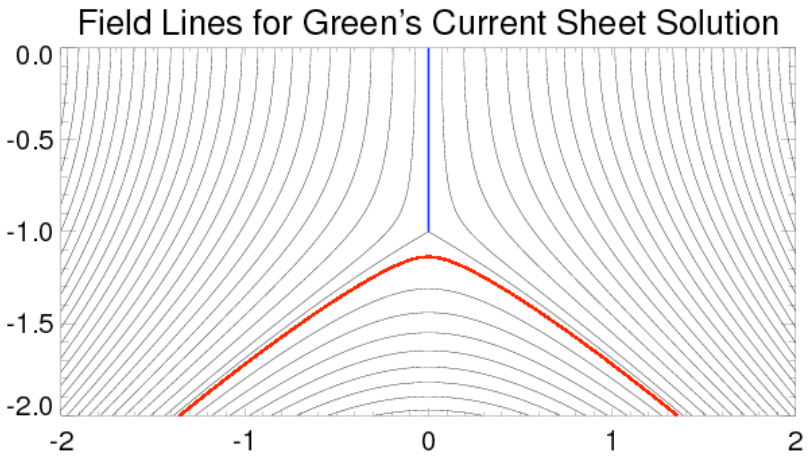

Figure 3.2: The field lines calculated by the Green current sheet model. The blue line represents the current sheet in the half plane. The red line illustrates the field line chosen for the basis of the simulated loop's geometry. From this figure it is easy to see why this is called Y-type. The current sheet connects with the separatrix field lines, just above the red line, to form an inverted Y.

Table 3.1: Initial properties of the post flare loop.

Parameter	Value
Length (L)	$6.0 \times 10^9\, cm$
Height	$1.8 \times 10^9\, cm$
Max Radius	$2.1 \times 10^8\, cm$
B_{min}	$21\, G$
B_{max}	$100\, G$
T_{max} (Initial)	$1.9 \times 10^6\, K$
Power Law heating parameters	$\alpha_H = \frac{3}{2}$, $\beta_H = 0$

as the origin of their coordinate system. This work used the top of the photosphere which led to a $2.0 \times 10^8\, cm$ difference in heights. The coordinates were then transformed with the local solar surface normal pointing in the $\widehat{z}$ direction. From Eq. 3.5 it can be seen why a field line just below the separatrix field line was chosen. If the separatrix line was chosen then the loop apex would intersect a magnetic null causing a discontinuity in the area. The loop was then placed on the top of the chromosphere. Cylindrical loop legs extended deep into a model chromosphere to provide a boundary condition and a reservoir of particles for the loop to draw from for chromospheric evaporation.

Now that a geometry had been defined, the state variables for each volume and surface grid had to be set. This was done by using the procedure described by *Martens* (2008). The simulated loop was heated by the power law heating equation of the form $E_h(s) \sim T^{\alpha_H} P^{\beta_H}$. A value of $\alpha_H = \frac{3}{2}$ was chosen since a flare loop was expected to be heated close to the reconnection site at the loop apex which was also the point where the temperature was a maximum. The loop was allowed to stabilize before particles were injected so that the effects of the nonthermal particles could be measured in isolation. After multiple iterations of MSULOOP with the heating function applied, the maximum velocity throughout the loop fell to a value $|\mathbf{V}| \leq 10^5 cm\, s^{-1}$. At this point the loop was considered stable, and the temperature, density and velocity profiles of the loop were set until the nonthermal particles were injected into the loop. The flare loop parameters are listed in table 3.

Nonthermal Particles

Nonthermal particles can be injected into a loop in a beam or series of beams, the properties of which are highly adaptable and dependent upon the experiment being conducted. The beam parameters were defined by a separate program that can be called on any of the time scales that were described previously and which also had access to all the loop state variables. This means that nonthermal beams can be generated as a function of a loop's evolution. While this offers many exciting possibilities, in the series of experiments described within this work, a single species beam was defined *a priori* and injected at the loop apex to simulate the effect of a current sheet directly accelerating nonthermal particles.

Beam Species In the following experiments all nonthermal particles were assumed to be electrons. This may seem to have been a cavalier choice, since the assumed electric field that accelerated the electrons should have accelerated protons and ions as well. Since it was previously stated that PATC could handle protons and ions, the exclusion of these positively charged particles requires an explanation. Many studies focus on nonthermal electrons to the exclusion of protons and ions. The reasons for this vary from study to study. The rationale for excluding protons and ions in this study is limited to two simple arguments.

While there are theoretical and some observational arguments that suggest that the energy carried by protons and ions should dominate the energy carried by electrons in flares (*Simnett* 1986; *Martens* 1988; *Ramaty et al.* 1995) this is not always observed to be the case. The γ-ray lines produced by proton bremsstrahlung are only observed by *RHESSI* in the most powerful of flares (*Shih et al.*, 2007). This is not simply an observational bias since *RHESSI*'s dynamic range adequately covers an unsaturated dynamic energy range of a few tens of *keV* to tens of *MeV* that covers soft X-ray emission to the hard X-ray and γ-ray emission indicative proton bremsstrahlung and the excitation of nuclear lines that could

only be the product of proton/ion collisions (*Lin et al.* 2002; *Brown et al.* 2006). Also, *Aschwanden* (1996) analyzed the energy dependent time of flight profiles of protons, electrons and the observed HXR spectrum and discovered that protons were a very unlikely source of the observed HXR emission in the $20-200\,keV$ range and therefore ruled out protons as the primary energy carrier in solar flares. Thus, many of the observational studies of flares assume that electrons are the dominant, if not only, particle species that is accelerated out of the thermal distribution. This has led to many studies that deal with electrons as the sole nonthermal particle species in flares (Eg., *Holman* 1985; *Mariska et al.* 1989; *Li et al.* 1989; *Veronig et al.* 2002b; *Veronig et al.* 2002a; *Yokoyama et al.* 2002; *Benz and Saint-Hilaire* 2003; *Kašparová et al.* 2005; *Hamilton et al.* 2005). In order to compare the results of the experiments carried out to these previous studies, it makes sense to consider electrons only for now.

Despite the above argument, there are flares that produce signatures of proton and ion acceleration (Eg.: *Lin et al.* 2003; *Aurass et al.* 2006; *Li et al.* 2007). So the question becomes, why do some flares show signs of proton acceleration while most do not? Is it simply a function of the amount of energy liberated by the flaring process? *Litvinenko* (1996) proposed a model of nonthermal particle acceleration in a reconnecting current sheet that contained a longitudinal component of the magnetic field. The strength of this component changes the ratio of electrons to protons in the emerging nonthermal beam. The longitudinal component of the magnetic field is treated as a free parameter. In this particular study it is assumed that the parameter is set to an unknown value that yields a number of protons in the nonthermal beam that is insignificant compared to the number of electrons. The exploration of that particular domain of parameter space is left to future work.

Beam Time and Energy Distribution. Nonthermal particles were injected into the post flare loop in a series of sub-beams, each of duration equal the the PATC cross-talk time,

$\Delta_C t$. The number of sub-beams created depended upon the time assumed that particles are accelerated out of the thermal distribution and into their nonthermal state. In the model used for the experiments outlined, it was assumed that nonthermal particles were directly accelerated by the current sheet formed in the reconnection region. Particle acceleration occurred as field lines pass through the current sheet and were reconnected to form a post flare arcade. Following the work of *Fletcher and Martens* (1998a) it was assumed that the time scale for particle acceleration was of the order of the time it took the field line to pass through the current sheet assuming an average speed of $\sim v_A$. With a loop top density of $n_e \approx 9 \times 10^8\, cm^{-3}$ and a magnetic field strength of $B \approx 21\, G$ the Alfvén speed was found to be $v_A \approx 1.5 \times 10^8\, cm\, s^{-1}$. At this speed it would take the field line $\approx 2s$ to traverse the current sheet.

The initial injection of nonthermal electrons was assumed to follow a power law distribution in energy flux, $F(E) = F_0 E^{-\delta}$, which followed the work of other studies (E.g. *Tandberg-Hanssen and Emslie* 1988). The energy for each particle was drawn from a random probability distribution that followed the above power law, i.e. $p(E) \sim E^{-\delta}$, where δ is a free parameter. In these experiments, $\delta = 3$ was chosen to follow the work of *Fletcher and Martens* (1998a) and was held constant. An energy distribution for a representative beam is shown in Figure 3.3.

The total energy injected had a time dependent Gaussian profile. Once the time profile and energy distribution of the nonthermal beam as a function of energy have been defined, a scaling factor is applied to the test particles so that the total energy in the test beam corresponds to observed flare energies. A total energy of $1.0 \times 10^{30}\, ergs$ is chosen to simulate a reasonably sized flare (See *Sui et al.*, 2005b, for an example of an observation of such a flare.). Since the current set of experiments was designed to test the strength of hydrodynamic effects on nonthermal particle evolution, the entire energy budget of the flare was put into the generation of nonthermal particles and no energy was put into an additional

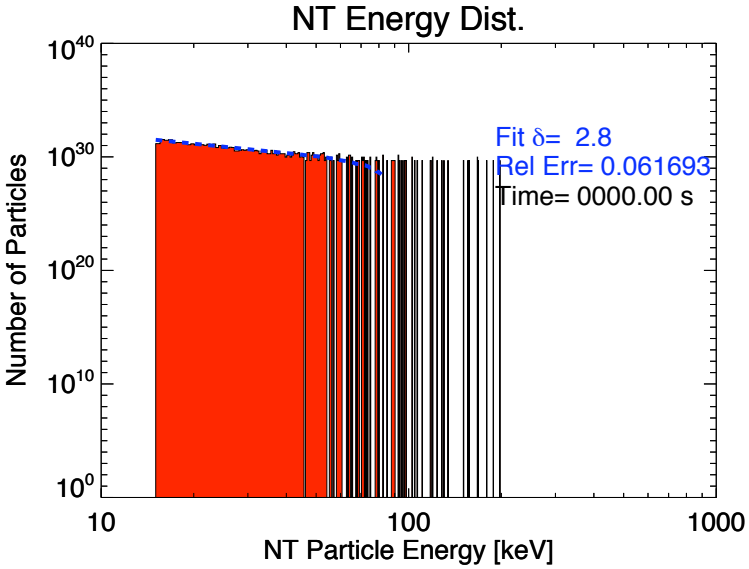

Figure 3.3: A log-log plot of the number of particles as a function of energy. The slope of this corresponds to the *electron spectral index* δ. A value of $\delta = 3$ was input into the beam generator. The fitted value is shown as $\delta = 2.8$.

thermal heating term.

Pitch-Angle Cosine Distribution The cosine of the pitch-angle for each nonthermal test particle was randomly drawn from a probability function that is defined by a single parameter, γ_{PA}. The parameter γ_{PA} acted as a knob that changed the *kurtosis* of the probability function (See *Press*, 2002, for a complete description on kurtosis and other higher moments of distributions.). A γ_{PA} value of zero represents a normal distribution in pitch-angle cosine with every value having an equal probability. As γ_{PA} increased the distribution became more *leptokurtic*, or steeply peaked, around zero in pitch-angle cosine. A γ_{PA} value of 9 corresponds to a Gaussian distribution. A uniform distribution has a kurtosis of -1.22 (*Weisstein*, 2009) which corresponds to a $\gamma_{PA} = 0$. A negative value of γ_{PA} decreases the kurtosis of the distribution further. This has the effect of making the distribution more steeply peaked around -1 and 1.

The above formulation of the pitch-angle cosine probability distribution allowed for a wide range of physically relevant nonthermal beams to be described by a single pitch-angle cosine parameter. For this experiment $\gamma_{PA} = -4$ and was constant in time for all experiments. This value was chosen to yield nonthermal beam with a large number of particles that had momentum aligned parallel or anti-parallel to the magnetic field. However the beam still had a nonzero fraction of particles with a significant amount of their momentum perpendicular to the magnetic field. This distribution was consistent with the results of the reconnecting current sheet models of *Martens* (1988) and *Litvinenko* (1996). Both of these direct acceleration models predict that the majority of particles accelerated from a thermal distribution with a temperature of $\sim 2-3\times10^6\,K$ will primarily be beamed along the magnetic field lines that comprise the flaring loop. This, again not coincidently, was also similar in general character to the pitch-angle distribution used by *Fletcher and Martens* (1998a). However, no effort was taken to exactly match the parameters of their distribution,

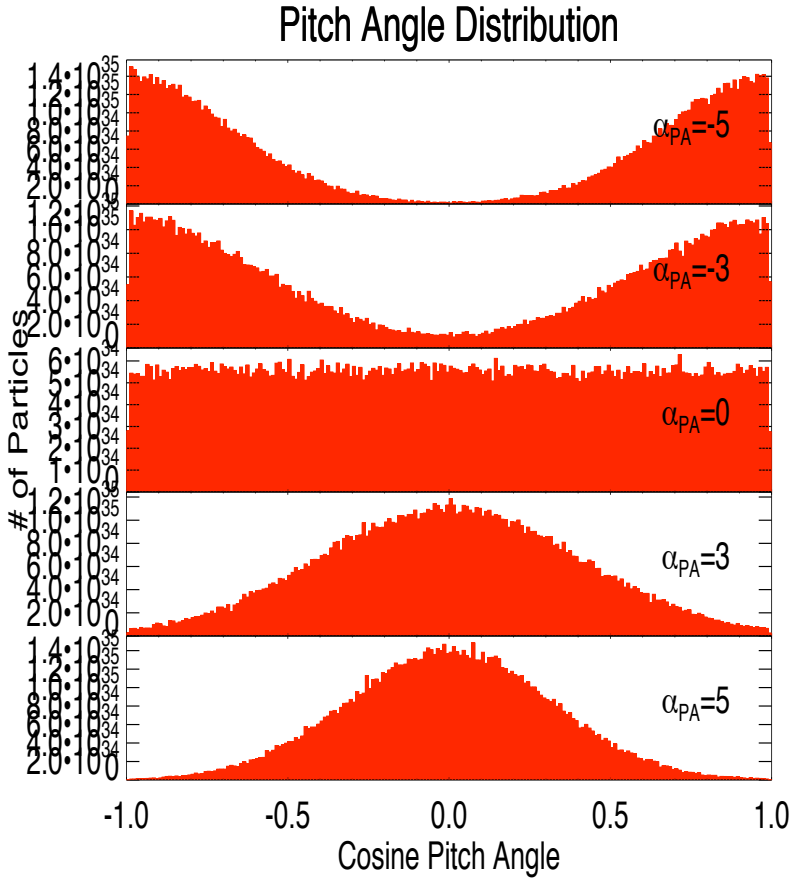

Figure 3.4: A plot of various pitch-angle cosine distribution functions, $f(\mu_{PA})$, corresponding to $\gamma_{PA} = -5, -3, 0, 3, 5$. A pitch-angle cosine of 1 (-1) corresponds to the nonthermal particle's momentum being directed parallel (anti-parallel) to the loop axis. A pitch-angle cosine of zero corresponds to the nonthermal particle's momentum being directed perpendicular to the loop axis.

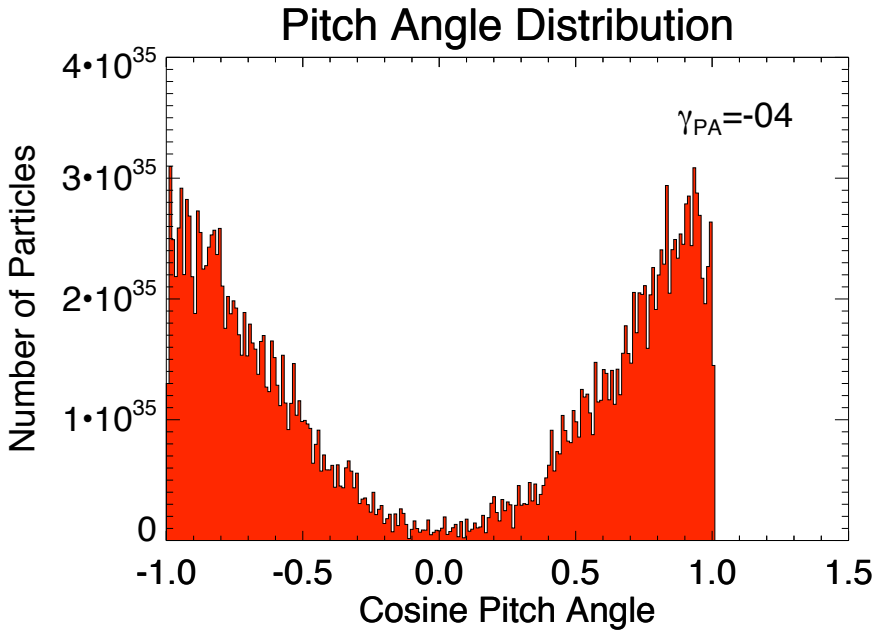

Figure 3.5: A plot of the pitch-angle cosine distribution to be used in the current experiment with $\gamma_{PA} = -4$.

such the distribution e^{-1} width, and the pitch-angle cosine distribution in this experiment lack the energy dependence of the previous work.

Error Tests

Grid Spacing Test

In order to determine the number of grid cells required for an accurate run, a series of simulations were performed. Each run used identical injected nonthermal beams to minimize random differences. The number of grid cells increased on each successive run. Temperature and density were chosen as test variables since they were not only state variables of the thermal plasma but also would affect the energy and momentum loss rates of the nonthermal particles. No nonthermal parameters, such as HXR flux, were chosen as

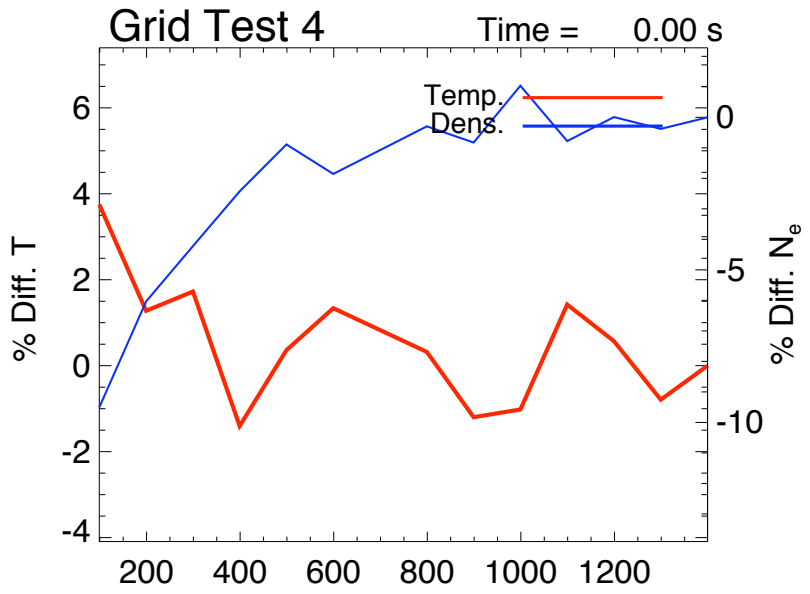

Figure 3.6: A graph showing the percent difference between the test variables, temperature and density, at a given number of grid cells in comparison to a simulation run with 1400 grid cells. This still was taken at the beginning of the simulation.

test variables since the position for each particle is defined on a continuum. A percent difference was taken comparing the test variables calculated from each run to a reference run with a grid containing 1400 cells. The percent differences, as a function of number of grids, are plotted in figures 3.6- 3.19 for five, ten, and 300 *seconds*. After the slope of the percent difference as a function of grid size was analyzed a determination that increasing the number of grids past 700 will not reduce the percent difference significantly enough to justify the increase in run time.

Monte Carlo Tests

In this test the simulation was repeated until the standard deviation, as defined by equation 2.38, of the test variables fell below some threshold value. Figures 3.9-3.11 show the average of the temperature and density, and the associated standard deviation as a function

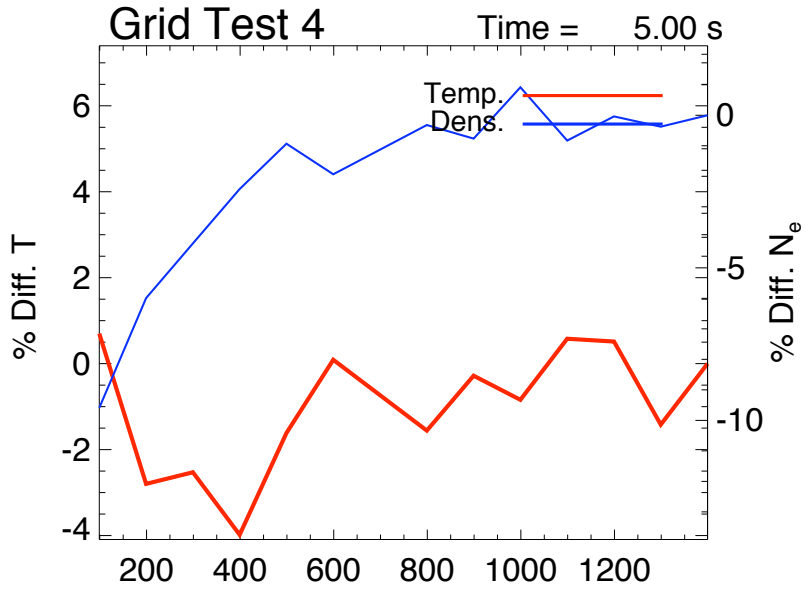

Figure 3.7: Same as 3.6 but taken after 5 *seconds* of simulated time.

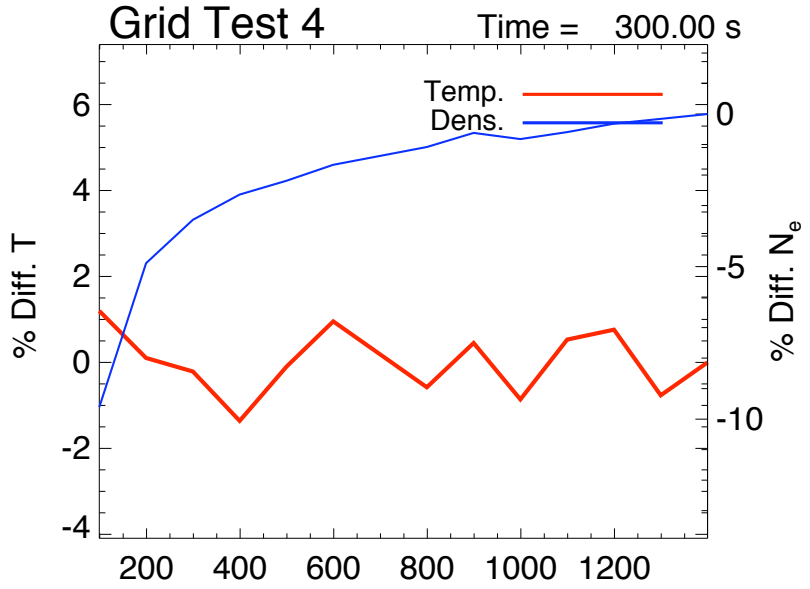

Figure 3.8: Same as figures 3.17 and 3.7 but at 300 *seconds*. By analyzing plots such as this for every time step it becomes apparent that increasing the number of grid cells past 700 only yields minor improvements in accuracy.

of the number of repeated runs at 5, 10 and 300 *seconds* respectively. Note that for all times the plots even out at $\sim N_{runs} = 10$. Past ten runs the rate of decrease in the standard deviation became small, while the increase in computer time for each additional run became high.

In order to test the effect of multiple runs over the lifetime of the simulation, a new variable, the *percent standard deviation*, was defined as

$$\%s_{QN-1} = \frac{s_{QN-1}}{\langle Q \rangle} \times 100\%, \tag{3.6}$$

where again $\langle Q \rangle$ is the average of the variable Q over all runs. This variable was plotted as a function of time for a given number of runs to help determine the number of runs necessary to produce an accurate simulation. Figures 3.12, 3.13, 3.14, and3.15 show the percent standard deviation of the temperature and density variable with five, eight, 12, and 15 runs in the simulation. Again it was apparent that increasing the number of runs past 12 does not drastically reduce the percent standard deviation of the hydrodynamic test variables.

The number of repeated runs also had a direct effect on nonthermal variables, such as HXR emission. In order to test the effects of run number on nonthermal particle variables, run tests are performed using the HXR emission in the $3-6\,keV$ and $12-25\,kev$ bandpasses at the loop apex as a test variable. Figure 3.16 shows that the percent error is a rapidly varying function that can be well in excess of 300%. This highlighted one of the difficulties of using importance sampling when drawing test particles from a random distribution. Since most of the energy of the beam is contained in particles with energy $< 50\,keV$ that range was more heavily sampled. The higher energy particles were not as well sampled but still contribute strongly to HXR emission at lower energies via bremsstrahlung. Thus, it required many more runs before the errors became small compared to the variables.

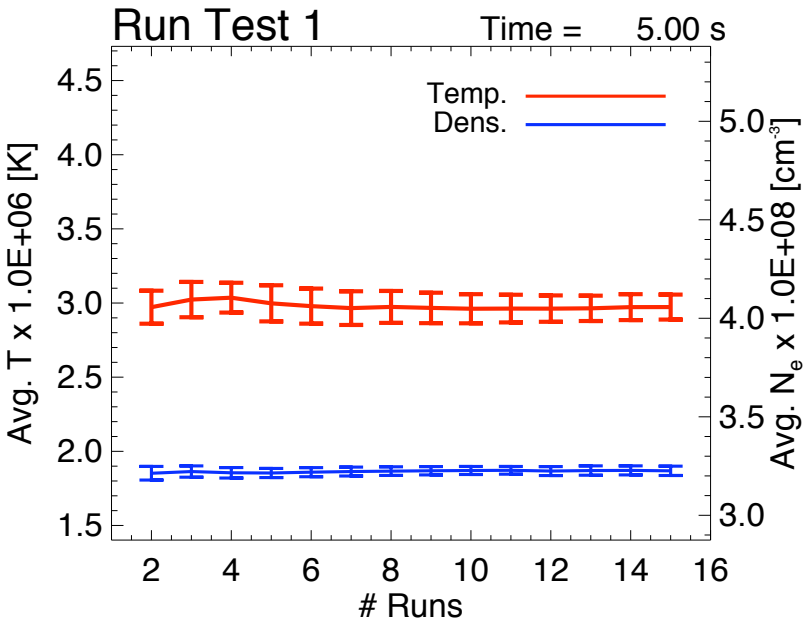

Figure 3.9: This plot shows how the average of the apex density and temperature and the associated standard deviation changes as a function of the number of runs five *seconds* into the simulation,

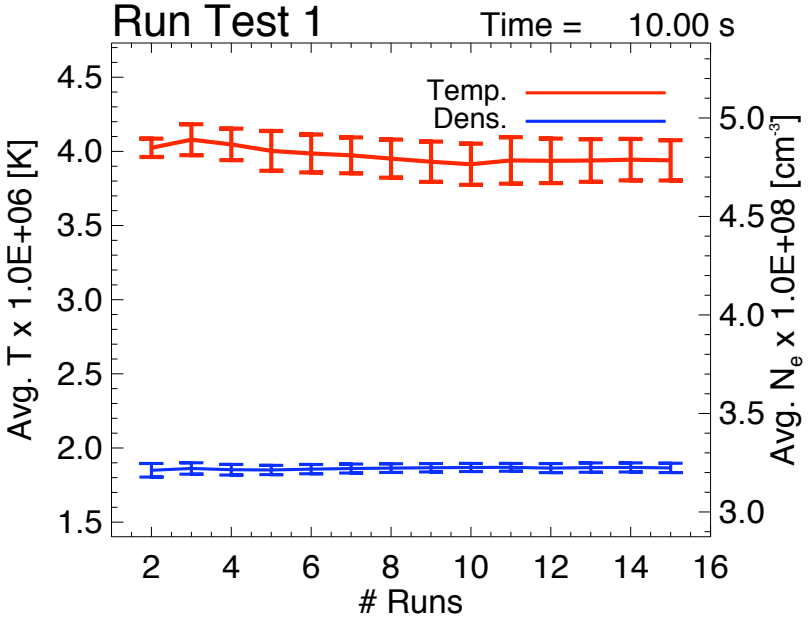

Figure 3.10: The same as 3.9 but 10 *seconds* into the simulation.

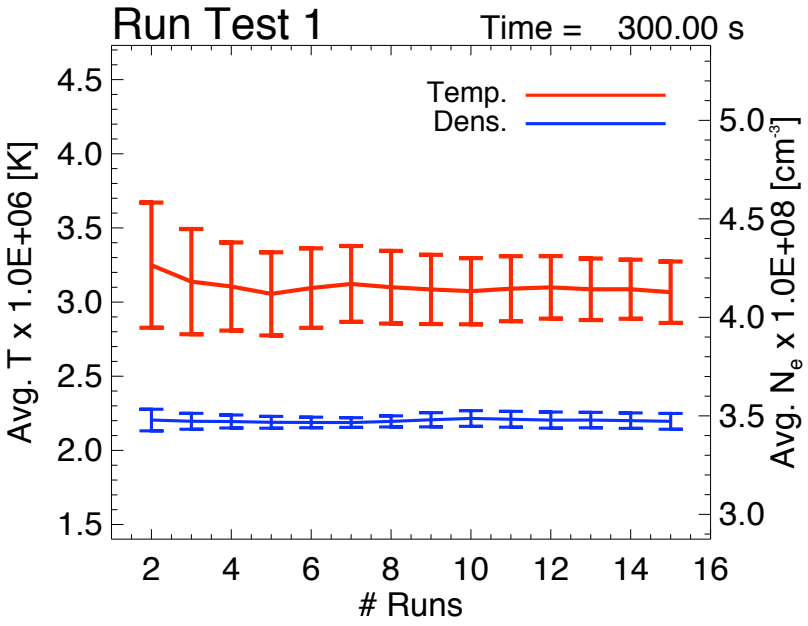

Figure 3.11: The same as 3.9 and 3.10 but 300 *seconds* into the simulation.

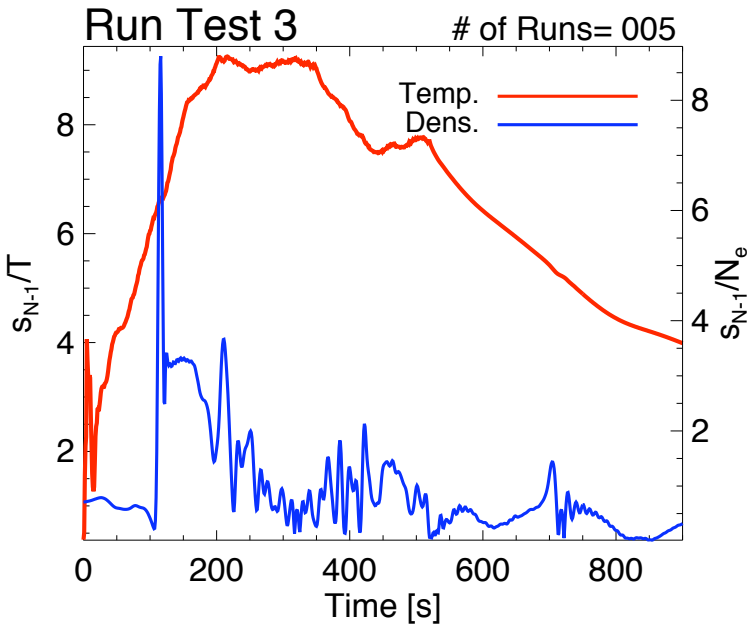

Figure 3.12: A plot showing how the percent standard deviation for temperature and density changes as a function of time for five runs.

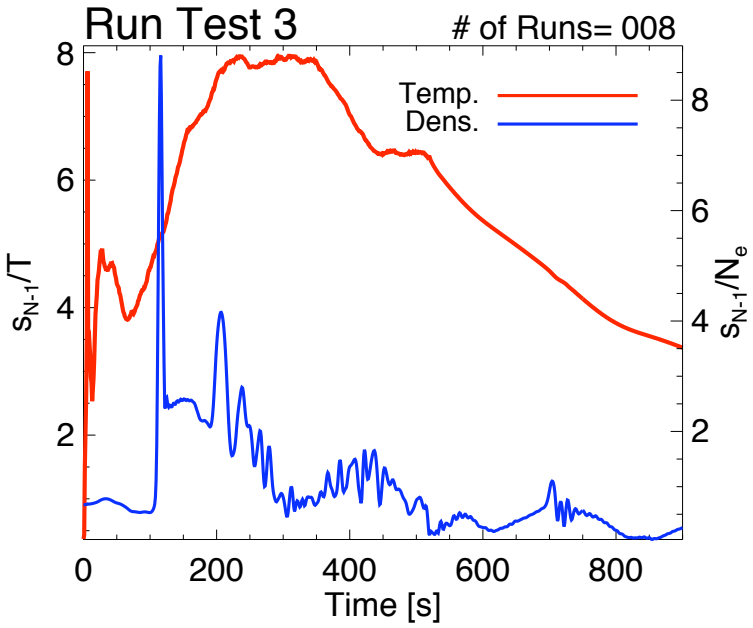

Figure 3.13: A plot showing how the percent standard deviation for temperature and density changes as a function of time for eight runs.

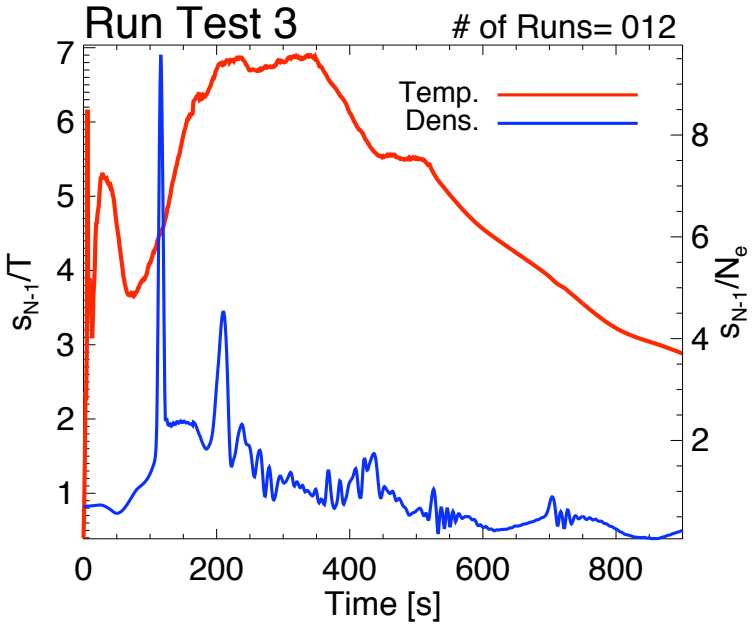

Figure 3.14: A plot showing how the percent standard deviation for temperature and density changes as a function of time for 12 runs.

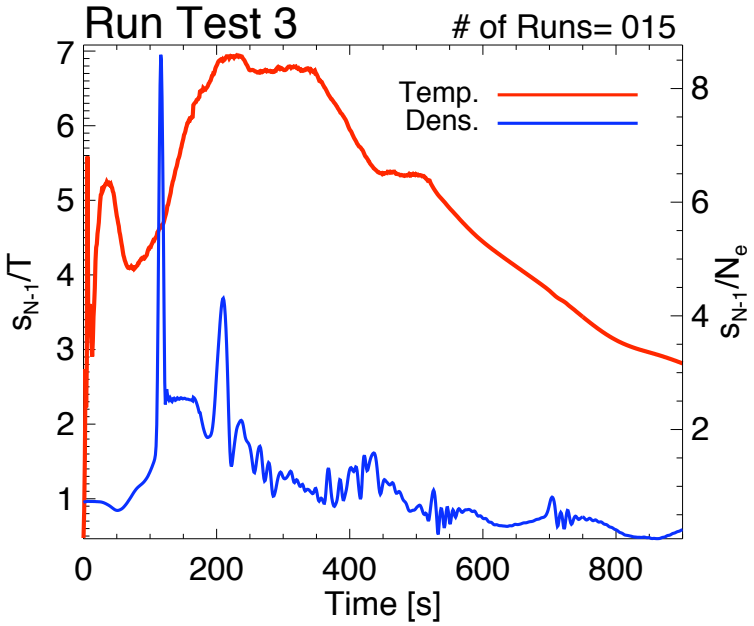

Figure 3.15: A plot showing how the relative standard deviation for temperature changes as a function of time.

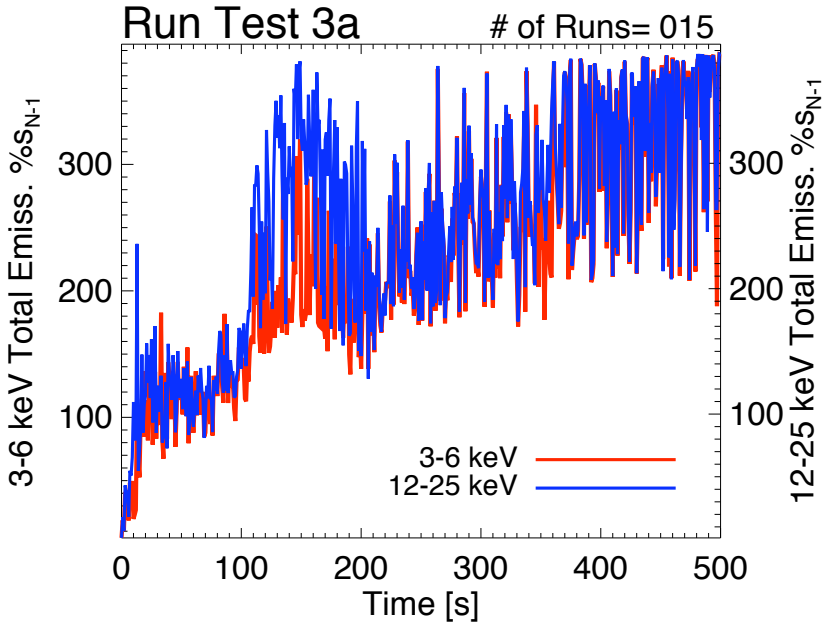

Figure 3.16: A plot showing how the percent standard deviation for $3-6\,keV$ and $12-25\,kev$ emission as a function of time.

The Effect of a Hydrodynamic Plasma on a Nonthermal Particle Beam

Common sense would dictate that allowing the thermal plasma target to evolve would have a significant impact upon the evolution of the nonthermal particle beam. However, this must be tested and may show surprising results. It also remains an open question as to the extent of an evolving plasma's effect upon the beam. To this end, several test variables were defined to describe the evolution of the nonthermal beam. Each test variable was measured for both the static and dynamic cases. In accordance with the most basic interpretation of the scientific method, a *null hypothesis* was defined as no statistical difference between nonthermal particle beams in the static simulation as opposed to the dynamic simulation as evidenced by the test variable measurements. Statistical tests were applied to the comparisons of each test variable measurement to yield the confidence level at which the null hypothesis could be rejected.

Effects on HXR emission

HXR emission was used as a test variable for nonthermal particle evolution since it is directly observable by *RHESSI*. Since photons in this energy regime were expected to be emitted primarily by nonthermal particles it should provide a useful diagnostic of the nonthermal beam. In order to test this assertion, both the thermal and nonthermal components of the HXR emissions were calculated. This allowed for the monitoring of thermal effects on the HXR signal.

A time series of plots were created for both the dynamic and static atmosphere simulations. In each plot, images were synthesized for a fictitious instrument with a angular resolution of $7''$ and a Gaussian point spread function with a full width at half maximum of 3 pixels. Each image was averaged over a temporal bin size of $4 seconds$. Note that

no attempt was made to make a detailed simulation of a specific instrument's response. However, the parameters stated above were close to commonly used values for the *RHESSI* instrument. Each plot shows the total, nonthermal and thermal contributions to the total signal in each passband, with contours enclosing the 40%, 60%, and 80% signal levels.

The light curve at the bottom of figures 3.17- 3.22 was calculated by summing the total emission in the bounding box at each time step. By visual comparison, the light curve of the dynamic atmosphere simulation appeared to be different than the static atmosphere light curve. While both show an initial nonthermal emission source at the loop apex, the static atmosphere's source was far longer lived, lasting past $500 seconds$, albeit at a greatly reduced intensity that would possibly be drowned in noise. The nonthermal emission source in the static atmosphere was initially stronger but decreased far more gradually than the dynamic case. Both atmosphere simulations showed an initial dip in apex HXR flux as particles moved from the apex to the loop legs. The signals rebounded as particles were scattered or mirrored back to the loop apex. The dynamic atmosphere showed a thermal emission component that roughly equaled the nonthermal component during the rise of the flux. However, the thermal signal quickly plateaued and did not contribute significantly to the apex HXR emission for the rest of the simulation.

Since one of the long term goals of this code is to aid in the understanding of loop top sources, the differences in emission at the loop apex are tested. The apex emission is defined as all emission occurring within the bounding box in figures 3.17-3.22. The Monte Carlo estimated variable for this study was the summed emission within this box. This estimated value, along with its associated standard deviation, were plotted as a function of time for both the dynamic and static cases. These plots appear in figure 3.23 and in log scale without error bars in figure 3.24. The large standard deviations seemingly mask any differences between the two distributions. While the log scaled plot in figure 3.24 is suggestive of a difference between the two samples' variables, a more rigorous test is

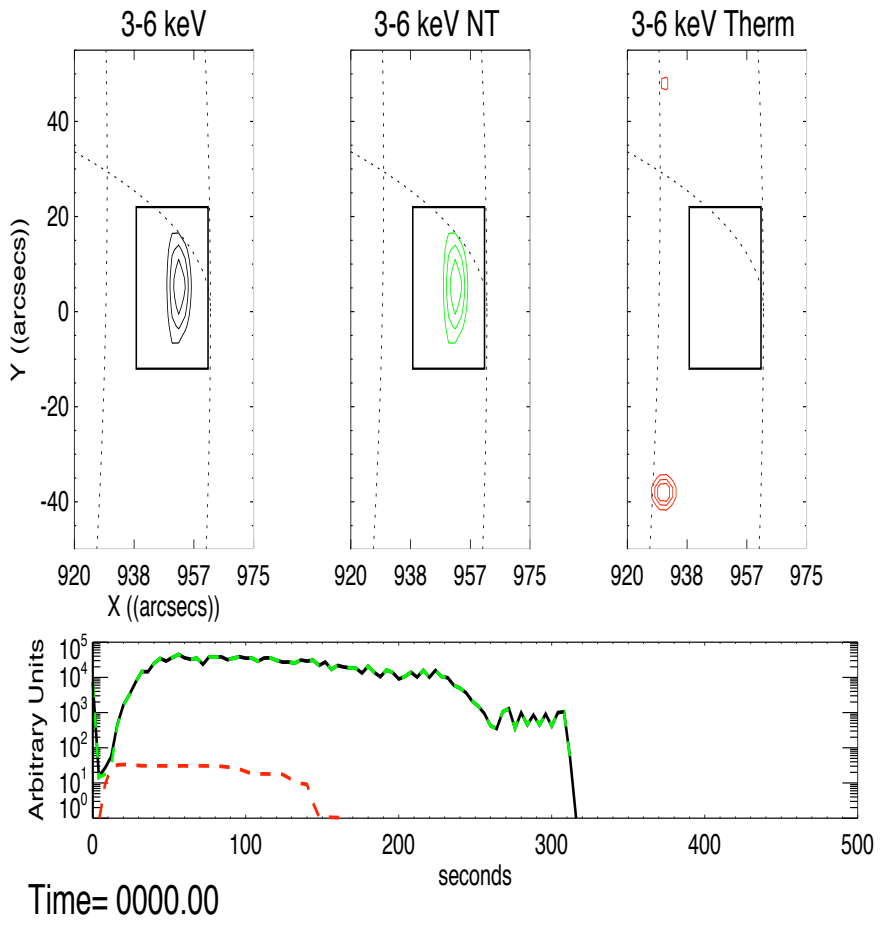

Figure 3.17: Hard X-ray emission in the $3-6\,keV$ passband for a dynamic atmosphere simulation. The top row shows emission simulated in an instrument with $7''$ pixels and a Gaussian point spread function with a FWHM of 3 pixels. The first column shows the total emission, the second shows the nonthermal component only, and the last column shows the thermal component only. The lower row shows the light curve of the total (black), nonthermal (green) and thermal (red) emission in the box defining the loop apex. Images are binned in $4\,second$ increments. Contours enclose the 40%, 60%, and 80% levels. This plot shows emission in the $0-4\,second$ time bin.

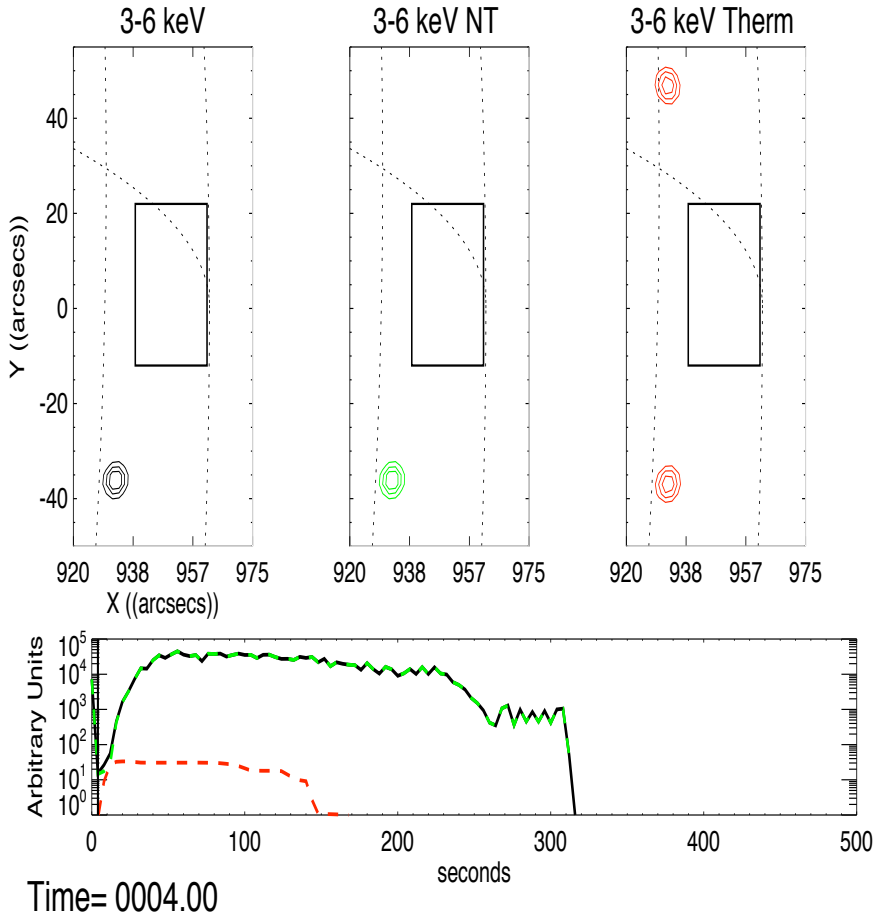

Figure 3.18: Same as figure 3.17 but from $4-8$ *second* time bin.

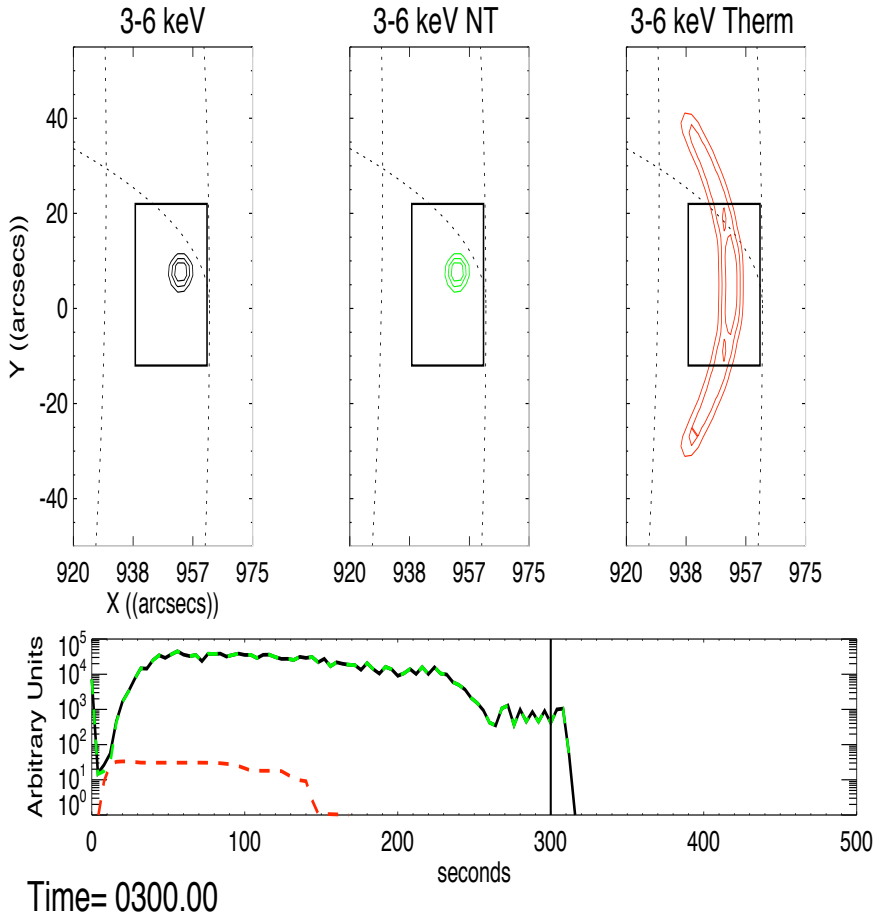

Figure 3.19: Same as figure 3.17 but from $296 - 300$ *second* time bin.

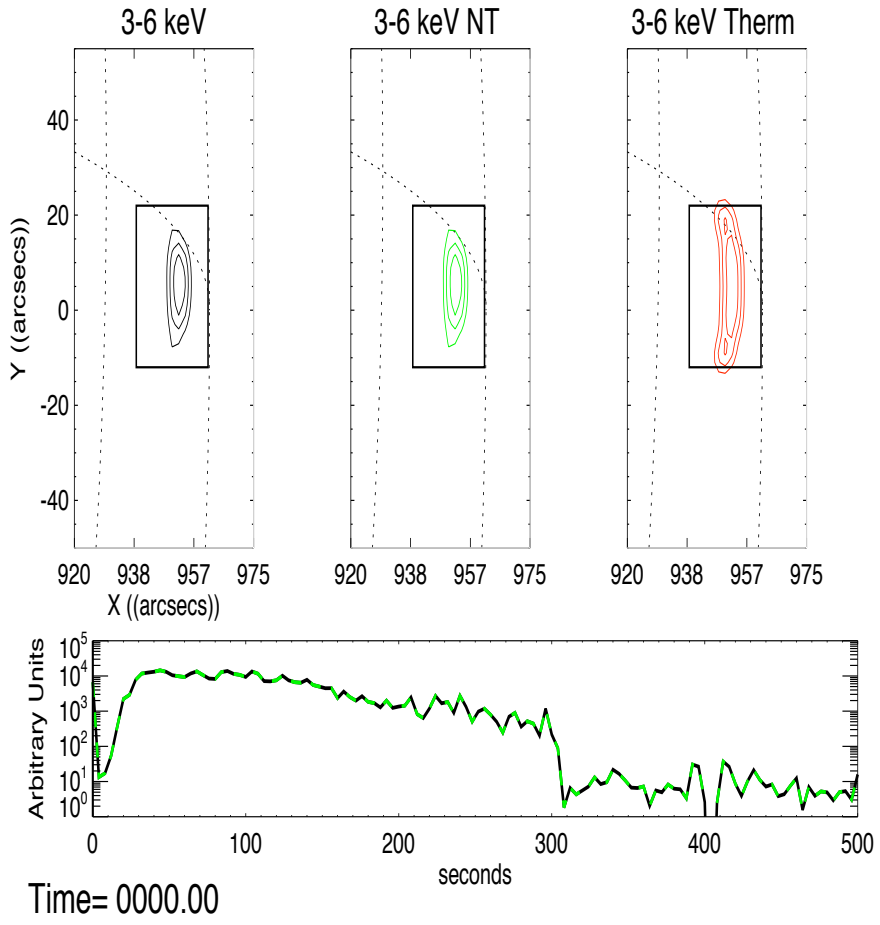

Figure 3.20: Hard X-ray emission in the $3-6\,keV$ passband for a static atmosphere simulation. This plot shows emission in the $0-4\,second$ time bin.

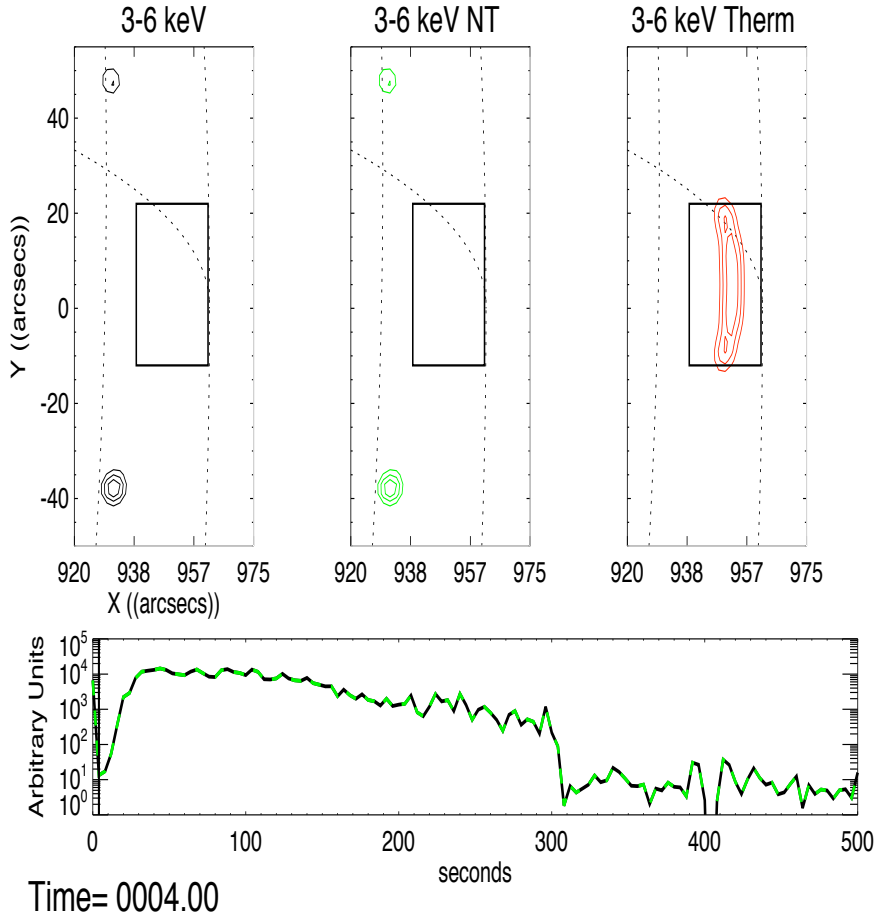

Figure 3.21: Hard X-ray emission in the $3-6\,keV$ passband for a static atmosphere simulation in the $4-8\,second$ time bin.

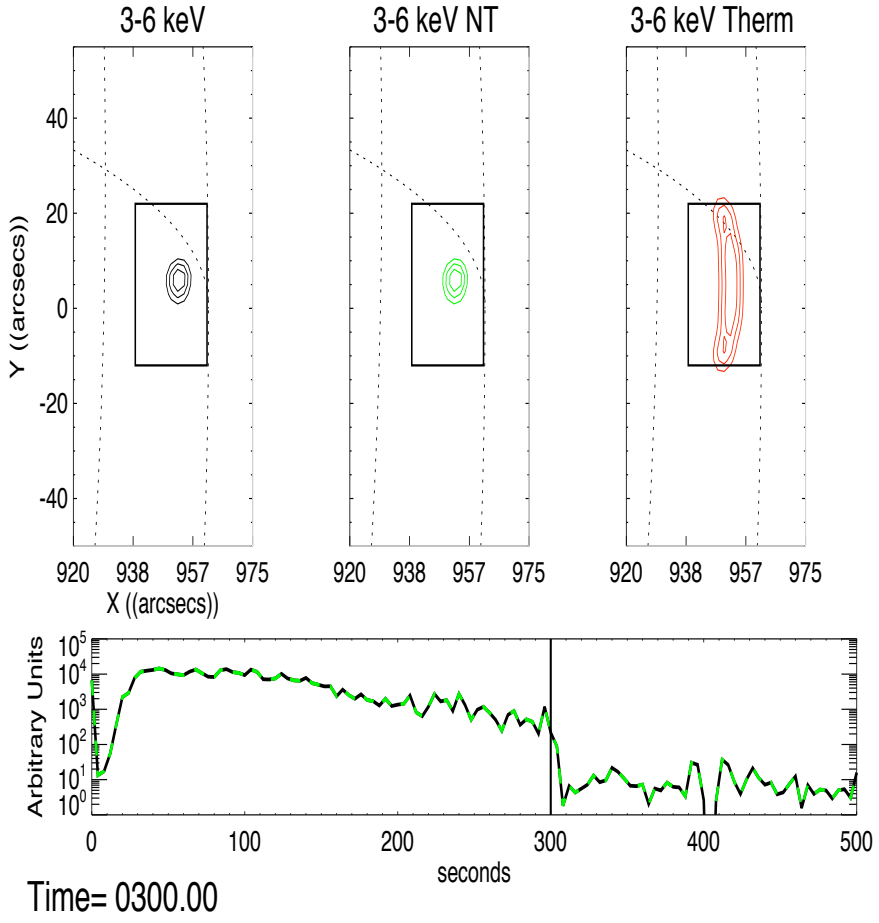

Figure 3.22: Hard X-ray emission in the $3-6\,keV$ passband for a static atmosphere simulation in the $0-4\,second$ time bin.

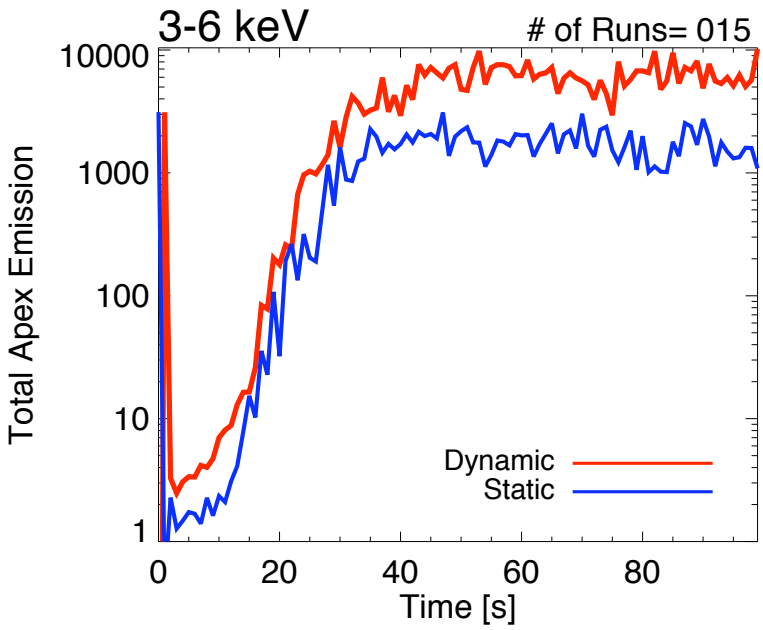

Figure 3.23: A comparison of the Monte Carlo estimator value of the apex hard X-ray emission in the $3-6\,keV$ passband in a dynamic (red) and static (blue) atmosphere. Error bars show the $+/-s_{N-1}$ value.

obviously required.

A statistical test must be applied to determine if the two sample data sets differ significantly. The *Student T-Test* is a widely used test that is sensitive to differences of sample means and very useful when sample sizes are small. However, the T-Test makes the assumption that the sample data to be tested are distributed normally. In order to determine if the sample data are distributed normally, a histogram plot is made of the sample data from both the dynamic and static atmospheres. The number of runs with an apex HXR flux in each energy bin are plotted in figure 3.25with the dotted lines representing the means of each distribution. Via inspection, it is obvious that the data sample is not distributed normally. Fortunately, there are other statistical procedures that can be used on non-normal data.

The *Kolmogorov-Smirnov Test* (KS) can not only be used to test if sample data are

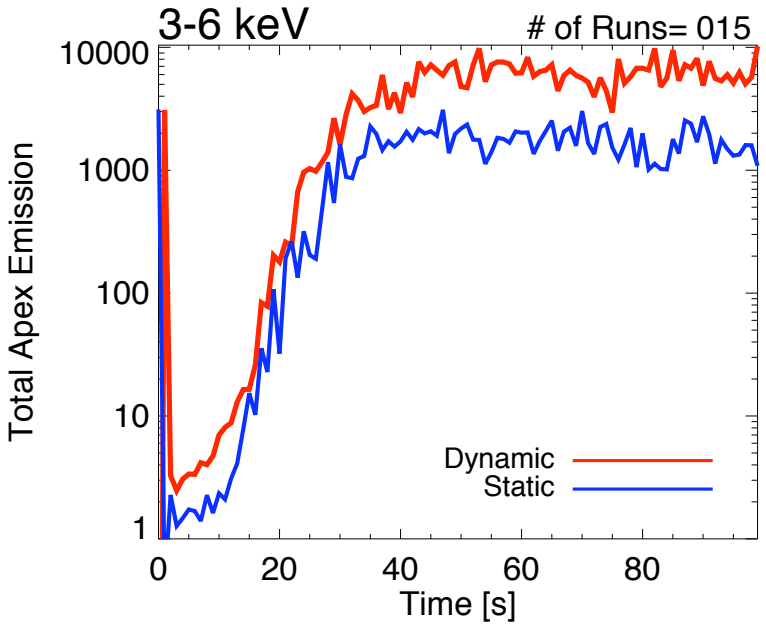

Figure 3.24: Same as figure 3.23 but plotted on a log scale. Error bars have been removed for clarity.

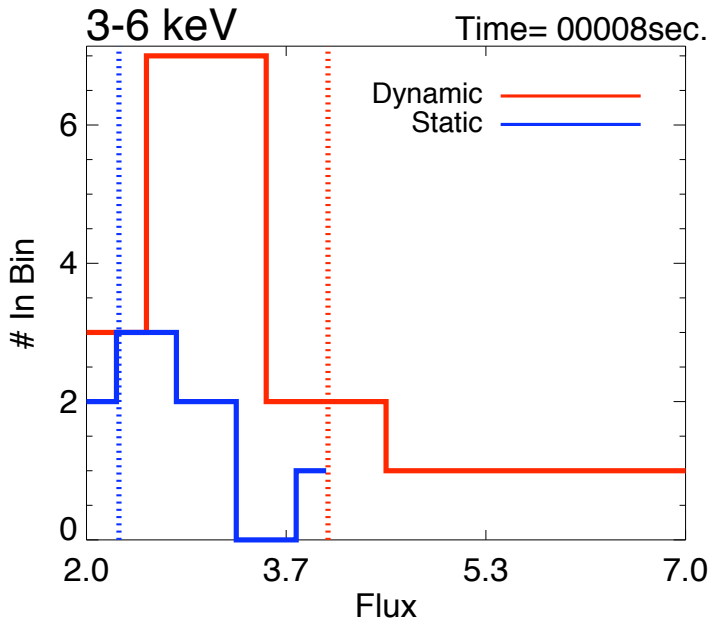

Figure 3.25: Distributions of sampled data with the dynamic case in red and the static case in blue. The means of the distribution, which comprise the value for the Monte Carlo estimator, are over plotted as a dashed line. Flux units are arbitrary.

normally distributed, but the two-sided version of this test can be used to test if the samples come from different distributions. The KS test has the advantage of being distribution independent, meaning that the shape of the sample data distribution need not be known, *a priori*. For each time step in the static and dynamic atmosphere simulation the HXR in the $3-6\,keV$ bandpass was sampled for each run. The samples from both simulations were then compared and a *Kolmogorov-Smirnov D* statistic was calculated using the *kstwo.pro* procedure in the SOLARSOFT software library. For each value of D, a probability, p_D, was calculated that the value could have been obtained by chance. A *percent confidence* was defined as

$$\%Confidence = 100\% - p_D \tag{3.7}$$

and yields the confidence with which the null hypothesis, that the two samples came from the same distribution, can be rejected. The test is limited to the first $300\,seconds$ of the simulations since the nonthermal beam in the static simulation has mainly been thermalized after this time and comparing a sample to a null sample, while valid, is non-illustrative.

Figure 3.26 shows the results of the KS test as a function of time. The results are striking: at no time after $80\,seconds$ does the percent confidence fall below 99.5%. These plots show that, on a second by second basis, the inclusion of hydrodynamic effects to the simulation of nonthermal particle beams has a statistically significant effect on the distribution of the simulated HXR signal in the $3-6\,keV$ bandpass.

Discussion It has been shown that hydrodynamics affects the evolution of the nonthermal electron but it remains to show how this effect is carried out. Of the three state variables, only the density and the internal energy density, as expressed by the temperature, are important to the evolution of the nonthermal particle beam. The speeds of even the lowest energy nonthermal particles are at least two orders of magnitude larger than the sound

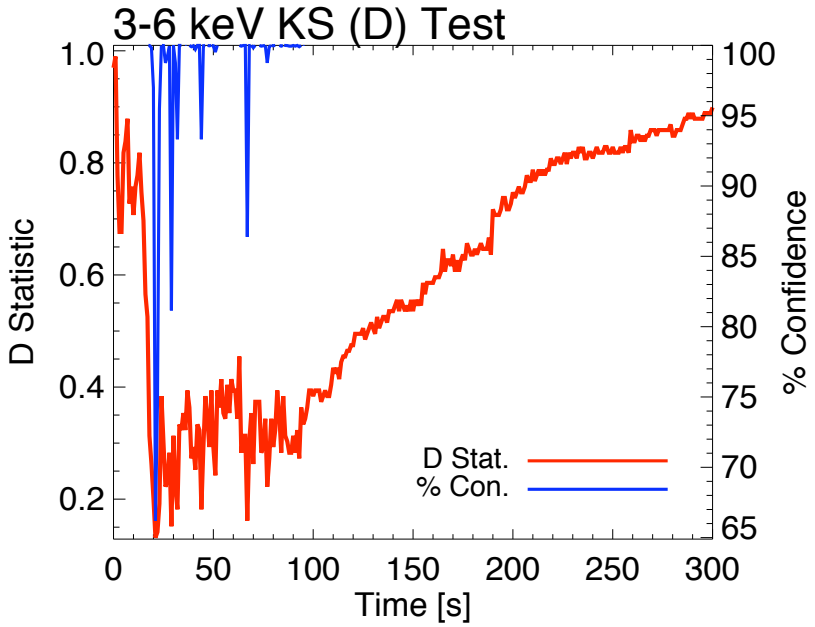

Figure 3.26: Kolmogorov-Smirnov test of the differences hard X-ray emission in the $3-6 keV$ bandpass in the dynamic and static atmosphere simulations. The red line maps the evolution of the D statistic as a function of time. The blue lines shows the confidence level with which the null hypothesis can be rejected. This provides strong, quantitative evidence that the evolution of the nonthermal beam is significantly statistically different in the dynamic atmosphere than in the static atmosphere.

speed of the thermal plasma. Even sonic flows change the relative velocity between nonthermal particle and target plasma very little. In order to understand the thermal plasma's effect on the nonthermal beam, the density and temperature evolution of the flare loop must be investigated.

The values of the state variables as functions of loop coordinate, s, are output at every $\Delta_R t$. Figures 3.27-3.30 show the evolution of the state variables over time. Material from the denser footpoints of the loop is heated and flows to the loop apex. The density and temperature both undergo a short lived increase of about a factor of three. Both the temperature and density factor into the electron-proton deflection time, and the electron-electron energy exchange time logarithmically through the Debye length, Eq. (2.17). Since the increases in temperature and density are of the same order, the linear density term in Eqs. (2.61) and (2.60) dominates making density the state variable that most strongly influences the nonthermal beam's evolution.

To look at the density more closely, it is plotted by itself in figures 3.31 - 3.34. The red lines represent the density of the dynamic atmosphere and associated 1σ errors. The blue lines are the values for the static run. The density increase at the apex undergoes a maximum at $t = 125\,seconds$ as the waves of increased density coming up from both sides collide. The compact increase in density straddles minor density decreases on either side, but the apex density increase is long lived as can be seen in fig. 3.34. It is hard to understand how an increase of density at the loop apex can increase the lifetime of a looptop HXR emission source. At first one might think that a density enhancement would decrease the life of the beam due to additional collisions. The density enhancement in this experiment is not enough to provide a thick-target which would extinguish the nonthermal beam, but would increase the HXR signal via Eq. (2.73). However, this still does not explain the longer life of the nonthermal beam.

The longer life of the nonthermal beam can be explained by the deflection time of

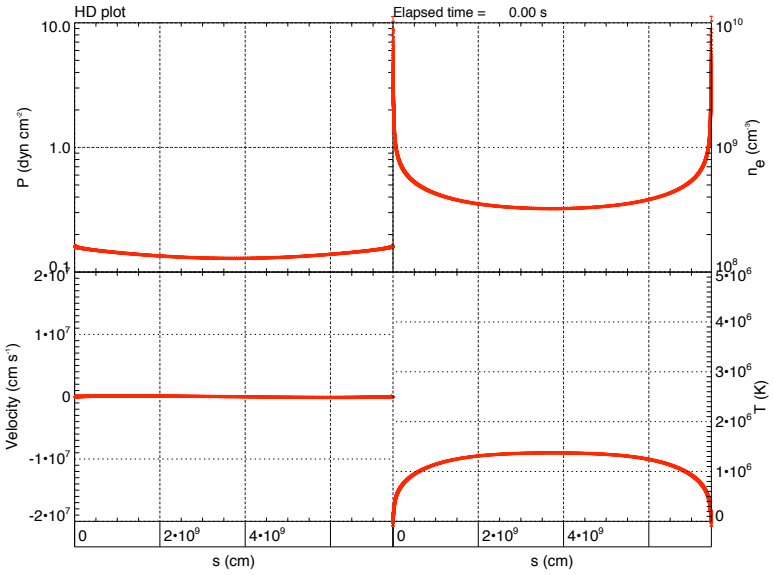

Figure 3.27: Plots of the pressure, density, average velocity, and temperature as a function of loop coordinate. This plot is at the beginning of the simulation.

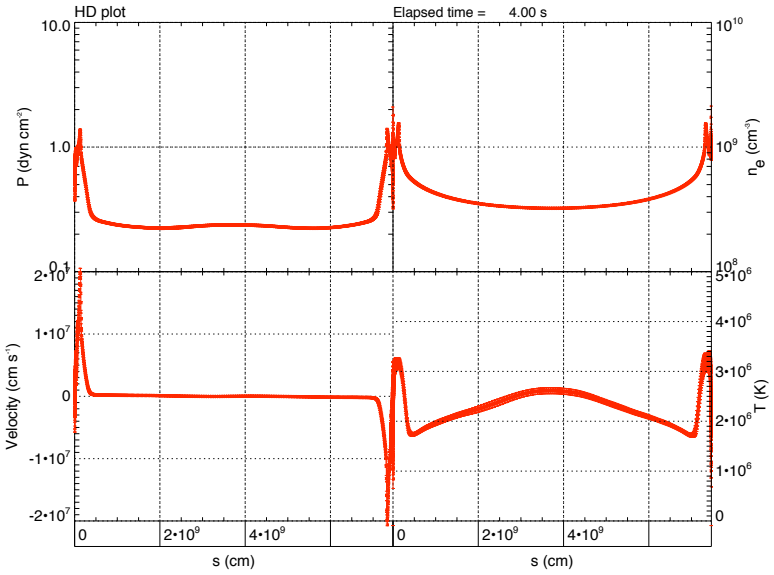

Figure 3.28: Same as figure 3.27 but after four seconds of simulated time.

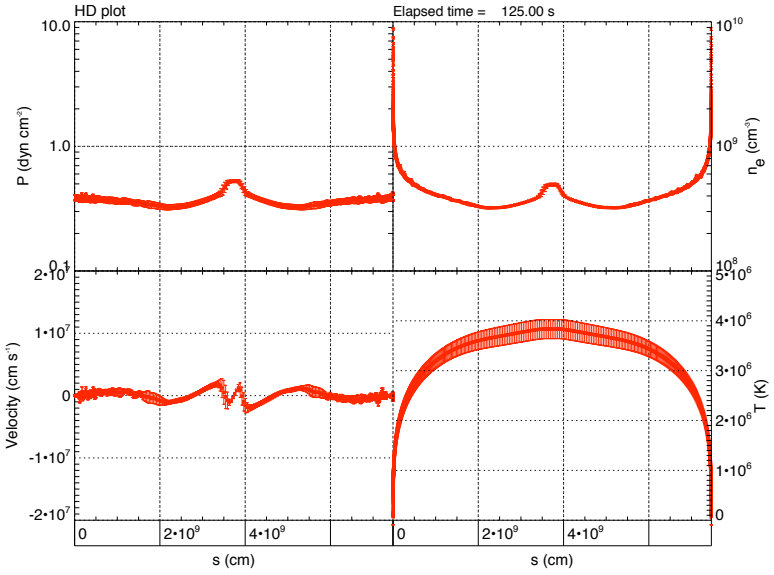

Figure 3.29: State variables plotted after 125 seconds of simulated time.

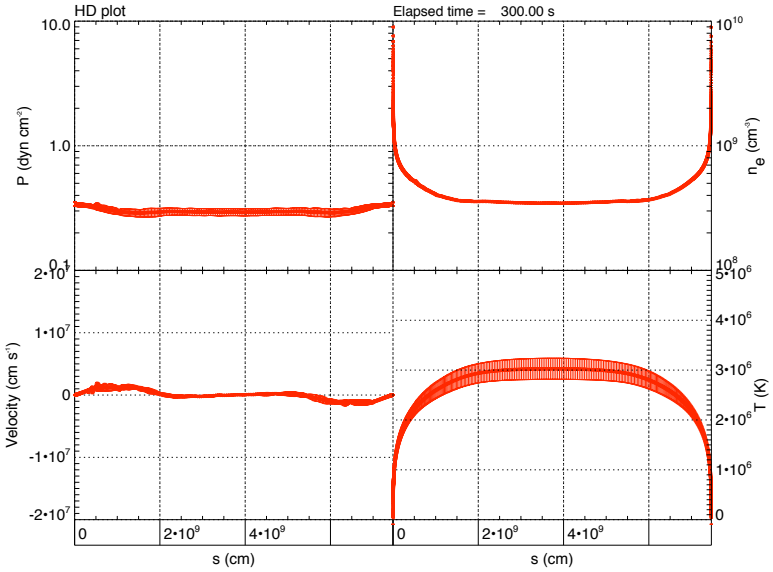

Figure 3.30: Plots of the state variables at 300 *seconds*.

particles in the beam, Eq. (2.61). Unlike the energy loss time, the deflection time is linear density. Thus, density changes will have a much stronger effect on the rate of change of the beam's pitch-angle cosine that the beam's energy loss rate. Deflections change the pitch-angle cosine distribution of the particles so that it is more isotropic. Particles that are not initially lost to the thicker target at the loop base, may be deflected to a pitch-angle cosine which catches the particle in the magnetic trap. Particles with a smaller absolute value of pitch-angle cosine sample the denser loop legs less frequently and lose less energy as a consequence. Thus it is the increased isotropization of the pitch-angle cosine distribution that causes the longer life of the nonthermal beam, and thus, the longer lived HXR source.

Apparent HXR Source Motions

In many ways the 2002 November 28 flare observed by *Sui et al.* (2006) resembles

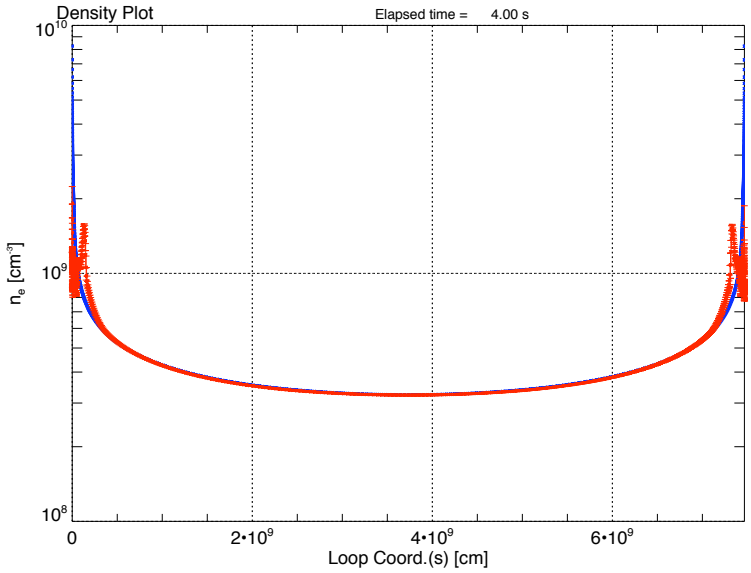

Figure 3.31: A plot of the density at four seconds of simulated time. Red represents the dynamic atmosphere and blue represents the static atmosphere, which is the same as the dynamic atmosphere at $t = 0 seconds$.

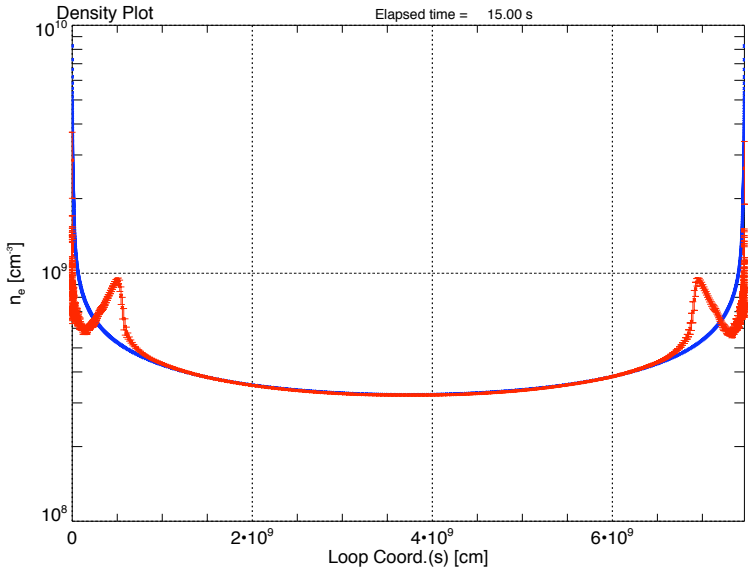

Figure 3.32: A plot of the density at 15 seconds of simulated time.

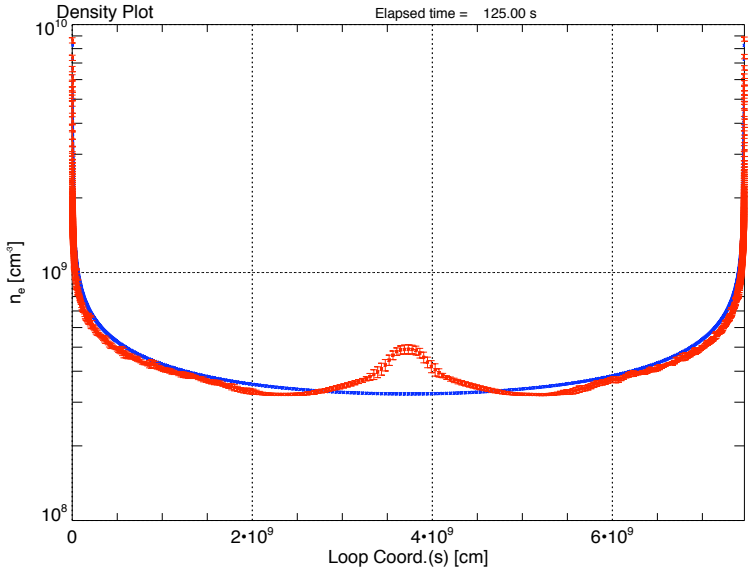

Figure 3.33: A plot comparing the static and dynamic atmosphere density at 125 *seconds*.

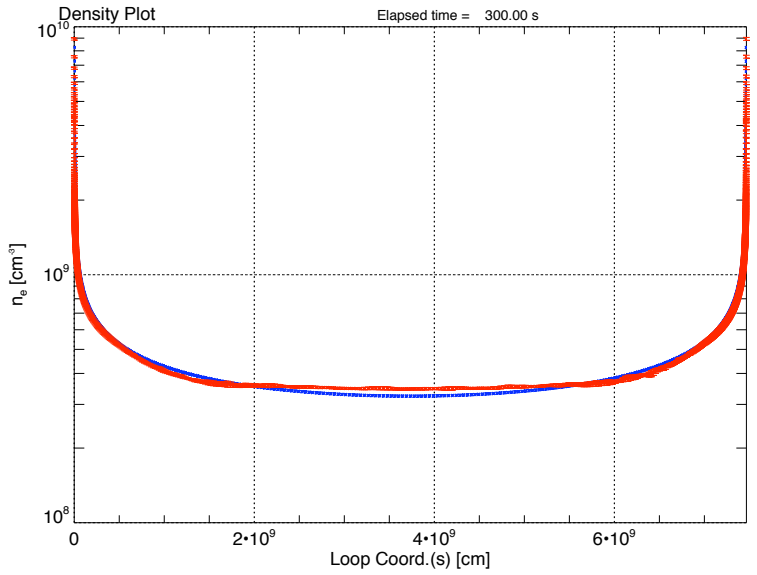

Figure 3.34: Density plot at 300 *seconds*.

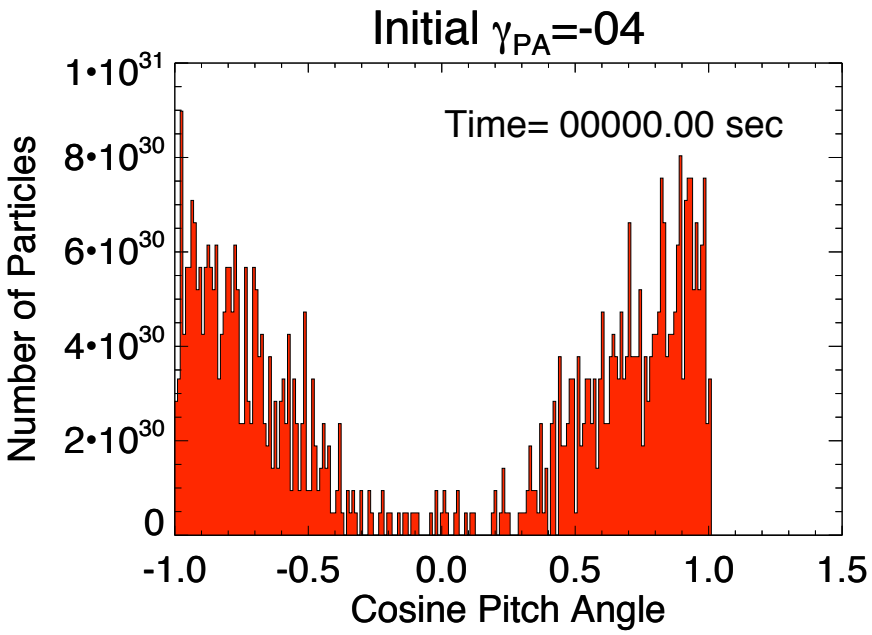

Figure 3.35: The initial pitch-angle cosine distribution for the dynamic atmosphere simulation.

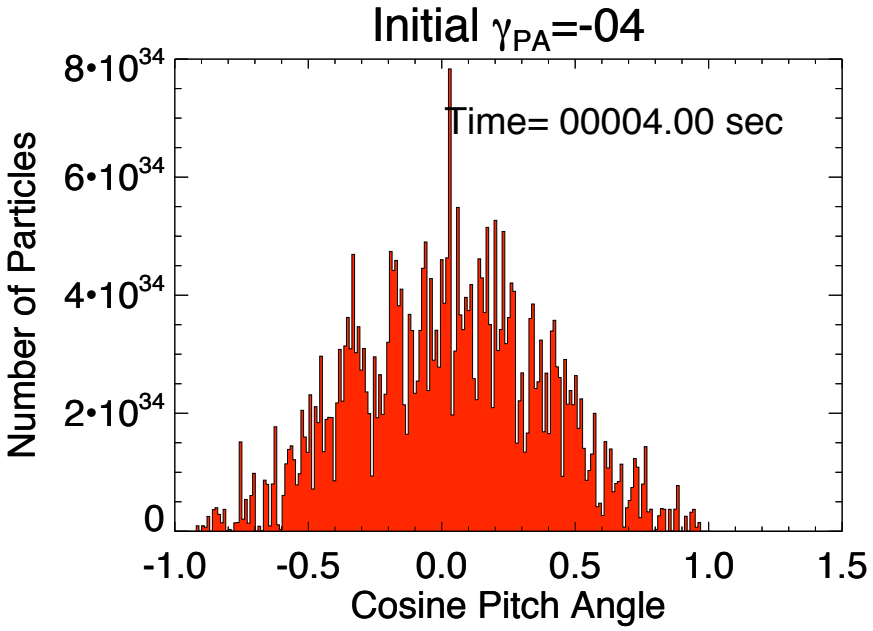

Figure 3.36: The pitch-angle cosine distribution for the dynamic atmosphere after four seconds of simulated time. Note that at this time the beam pitch-angle cosine distribution is closer to a Gaussian centered around zero. Particles with large absolute values of pitch-angle cosine have already lost all of their energy in the denser loop legs.

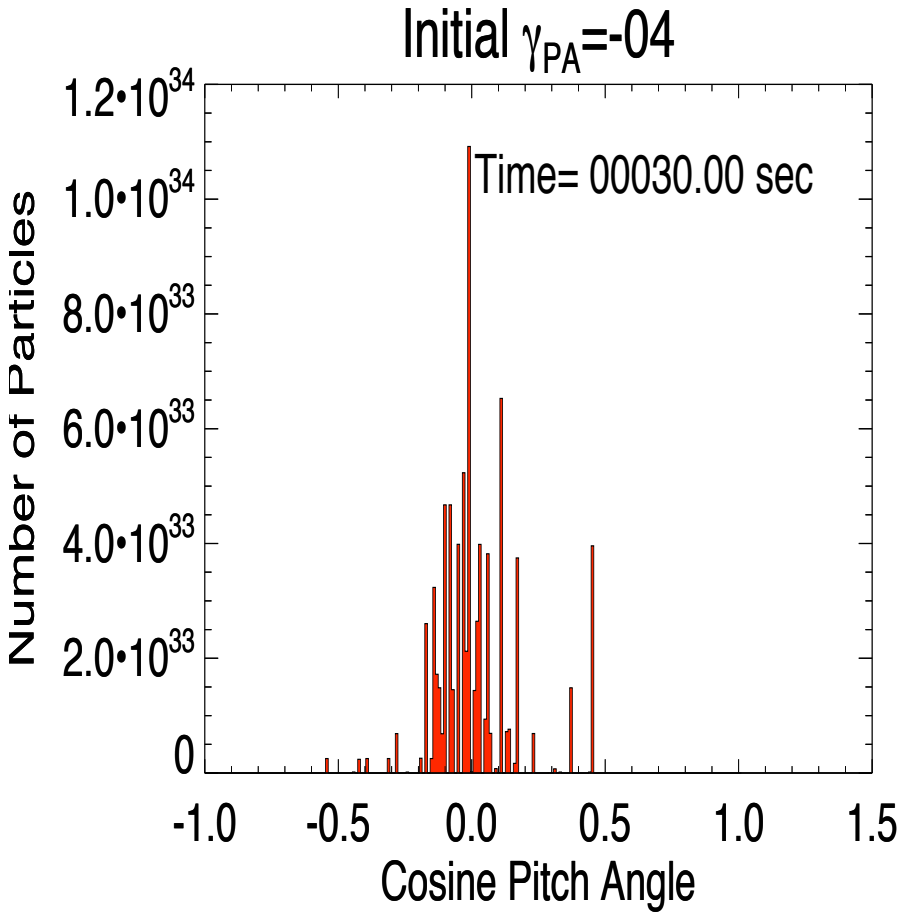

Figure 3.37: The pitch-angle distribution for the dynamic atmosphere after 30 seconds of simulated time. Note that the distribution of pitch-angle cosines is steeply peaked around zero. Particles that are at the loop apex, with such a small pitch-angle cosine will scatter less due to the low density of the loop apex. With less scattering, and a pitch-angles near zero, any particle near the apex will now be effectively trapped there.

the simulated flare in this experiment. In order to compare the effects of a static and dynamic atmosphere on a nonthermal beam's evolution, the entire energy of the flare was put into the nonthermal particles. This is analogous to an early impulsive flare that has no thermal, pre-heating of the flare plasma before the nonthermal HXR signal. Just as in the 2002 November 28 flare, figures (3.17)-(3.19) also show a $3-6keV$ HXR source that was initially at the loop apex, moved down to the footpoints and then back up to form a long lived HXR source. However, this apparent motion cannot be explained by the injected nonthermal beam having soft-hard-soft behavior in the energy spectral index since the spectral index of the injected beam was held constant at $\delta = 3$. Another interpretation of this apparent motion must exist for the simulation.

The explanation of this HXR source motion can be deduced by careful examination of figures 3.35-3.37. At the beginning of the simulation a nonthermal HXR source appeared at the loop apex due to the nonthermal beam being initially injected there. At this time there were a large number of nonthermal particles with large absolute values of pitch-angle cosines. These, highly beamed, particles could travel further down the loop legs, where the density was higher, without appreciable mirroring. The HXR source rapidly moved to the loop footpoints as the nonthermal particles travel down the loop legs. Particles that traveled further down the loop legs had increased nonthermal bremsstrahlung emission due to the linear density term in the bremsstrahlung, Eq. (2.73), and the increased density of the target plasma near the footpoints. Particles that traveled down the loop legs were also taken out of the nonthermal distribution more quickly due to the linear density term in the nonthermal energy loss equation, Eq. (2.56). With these particles out of the nonthermal distribution, the next strongest emission source were particles that mirror low in the loop where the atmosphere was still dense but not dense enough to provide a truly thick target. However, these thermalized quickly leaving the strongest emission source just slightly higher up the loop legs. This process continued with the HXR source appearing to move up the loop

legs until only nonthermal particles with a pitch-angle cosines near zero were left. These particles never strayed far from the loop apex, where the density was at a minimum.

The above explanation of the apparent motion of the HXR source was compelling. It offered a competing hypothesis for the observations of the 2002 November 28 flare that is simpler than that posed by *Sui et al.* (2006) and the only explanation possible for the simulated flare. However, tracking the centroids of the HXR revealed an estimated upward of speed of $1.3 \times 10^8\, cm\, s^{-1}$. This was an order of magnitude higher than the average upward speed of $3.4 \times 10^7\, cm\, s^{-1}$ reported by *Sui et al.* (2006). However, *Sui et al.* (2006) had no information as the the inclination, or shape of the loop observed. It may be found in future experiments that this apparent motion due to pitch-angle cosine evolution may still play a role in understanding this observation.

CHAPTER 4

THE EFFECTS OF DENSITY GRADIENTS ON NONTHERMAL PARTICLES

As was noted in the previous chapter, only the density variation in the dynamic case could have caused the the nonthermal beams to live longer than in the static case. While the changes in density were not large, around a factor of ~ 3, there were steep gradients in density that propagated up the loop as chromospheric evaporation took place. In order to study the effects of density gradients on nonthermal particle evolution, an experiment was undertaken to study these effects in isolation.

Experimental Setup

In order to understand the effects of density gradients on nonthermal particles, simulations were constructed that eliminated other factors, such as magnetic mirroring, temperature effects, etc. This was done by constructing a tube of uniform cross-section and at uniform height, to eliminate the effect of magnetic mirroring on the nonthermal particles and varying gravitational potential on the thermal plasma. The thermal plasma contained in the tube was not allowed to evolve hydrodynamically during the course of the simulation. Some details of the thermal plasma are listed in table 4.1. A series of ten simulations were conducted, each with ten runs. In each simulation the thermal plasma density in the tube was described by the following function,

$$n_e(s) = A_{NC} n_{e0} \exp\left(\frac{Gd(s)}{l/2}\right), \tag{4.1}$$

where $n_{e0} = 1.0 \times 10^9\, cm^{-3}$, A_{NC} is a normalization constant set so that the number of

Table 4.1: A table showing the properties of the constant cross-section tube.

Parameter	Value
Length (L)	$1.0 \times 10^{10}\,cm$
n_{e0}	$1.0 \times 10^{9}\,cm^{-3}$
Radius (Constant)	$5.0 \times 10^{7}\,cm$
T (Constant)	$1.0 \times 10^{7}\,K$

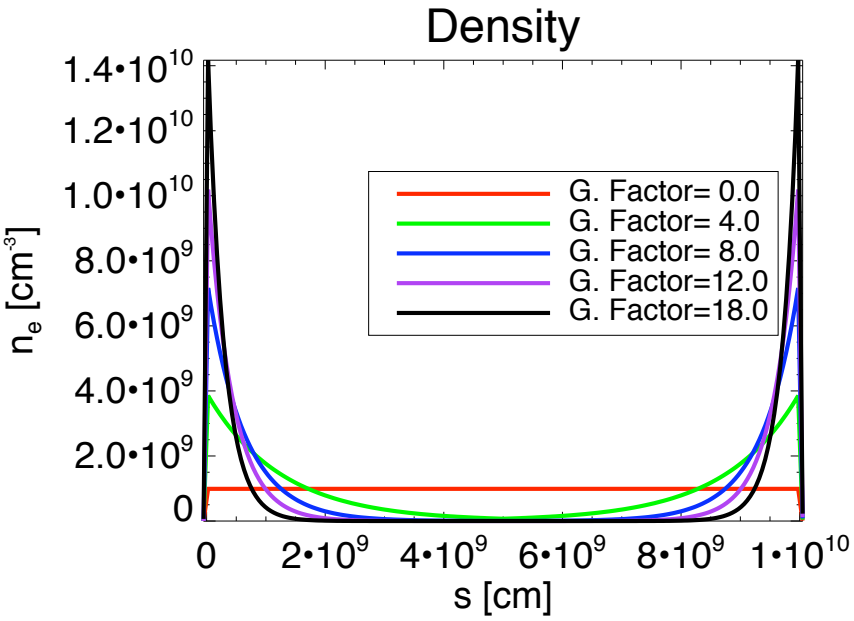

Figure 4.1: A plot showing the density profiles of the tubes used in this experiment.

thermal particles remains constant from simulation to simulation, G is a gradient factor that varies from 0 representing a uniform density to 18 representing a massive density gradient, $d(s)$ is the distance of point s from the center of the tube and $l/2$ is the tube half-length. A sample of density profiles as a function of tube length is shown in figure 4.1.

A nonthermal beam of 10^3 electrons was injected at the center of each tube. The pitch-angle cosine distribution was defined by $\gamma_{PA} = -4$ to correspond with the previous experiment. The position and pitch-angle cosine of each particle was tracked as a function of time. In order to describe the evolution of the pitch-angle cosine distribution as a function of time and gradient factor, I_{PA}/N was defined as the ratio of nonthermal particles with

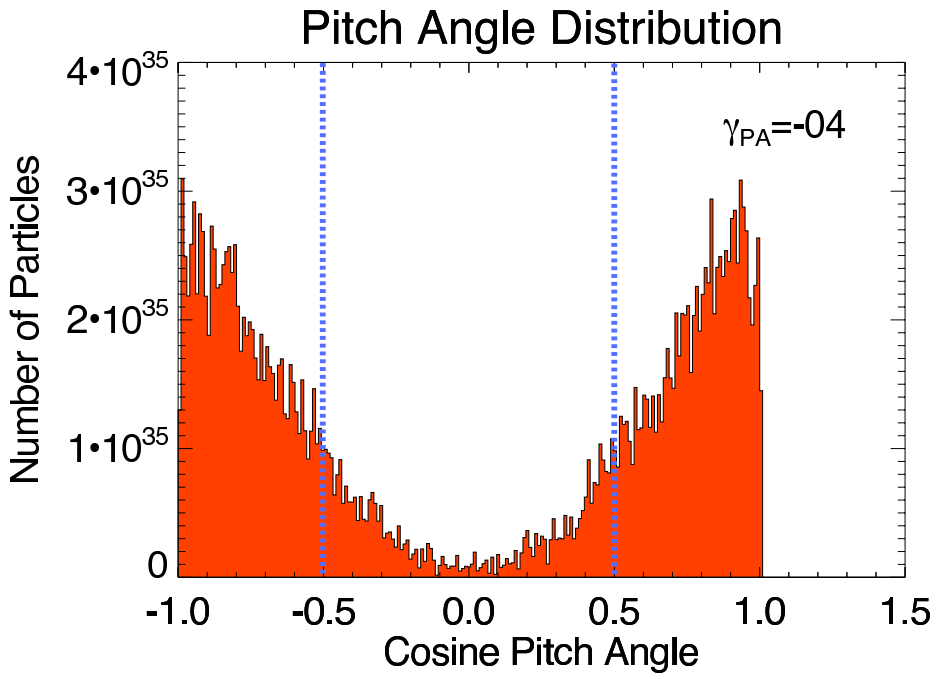

Figure 4.2: A plot showing the initial pitch-angle cosine distributions of the nonthermal particle beams injected into the center of the tube. The quantity I_{PA} is defined as the number of particles with a pitch-angle cosine between the two blue dotted lines, in the central portion of the distribution.

a pitch-angle cosine within the inner portion of the distribution, $-0.5 \leq \cos(\alpha_{PA}) \leq 0.5$, to the total number of nonthermal particles. Similarly, I_{pos}/N, was defined as the ratio of nonthermal particles in the inner portion of the tube to the total number of particles. All nonthermal particles had an initial kinetic energy of $25\,keV$. This energy corresponds to a velocity of $9.1 \times 10^9\,cm\,s^{-1}$, meaning that a particle with a pitch-angle cosine of 1 or -1 would reach the end of an empty tube in $\sim 0.5\,sec$. Any nonthermal electron that reached either end of the tube was reported as becoming part of the thermal distribution at that position and remaining there.

Results

To monitor how the nonthermal beam changed as a function of time, the median values

of I_{PA}/N and I_{pos}/N were taken due to the smaller number of runs. The median values for I_{PA}/N are shown in figure 4.3. Initially, the lower gradient factors showed a marked rise in I_{PA}/N. This was due to the fact that beams in a tube with a more uniform target scatter more initially. This had the effect of making the pitch-angle cosine distribution more uniform, since the direction of the scattering was random, more quickly than for the low gradient factor cases. The beam never reached a uniform distribution since many of the highly beamed particles reached the end of the tube quickly and had their pitch-angle cosine frozen. The higher gradient cases kept their more beamed ($|\cos(PA)| \approxeq 1$, small $\{I_{PA}/N\}\,med$) nature for a longer period of time. Eventually, each beam hit a density where enough pitch-angle cosine scattering occurred to increase the number of particles with $|\cos(PA)| \approxeq 0$. Higher gradient factor (≥ 8) $\{I_{PA}/N\}\,med$ curves show a shallower slope than the more uniform gradient factors, meaning that more particles kept their smaller pitch-angle cosines and had a significant fraction of their momentum directed perpendicular to the tube for a longer period of time. The gradient factor$= 8$ case showed the steepest rise in the number of particles with a small pitch-angle cosine.

The positions of the nonthermal particles were also tracked as a function of time for each density gradient factor. When the nonthermal particles became part of the thermal distribution, their position in space became fixed in time. Figure 4.4 shows the median inner position ratio, $\{I_{pos}/N\}\,med$, of the particles as a function of time. Initially, the majority of particles in all cases were near the tube center. The fraction of centrally located particles quickly drops at $t \simeq 5\,seconds$, as highly beamed particles, that did not scatter much in their travels, reached the ends of the tube. Note the slightly different slope for the gradient factor$= 0$ case. This was due to the fact that there were less highly beamed particles in the gradient factor$= 0$ case at $t \leq 1\,second$ because the nonthermal particles were encountering a higher density, thus more scattering, for a longer portion of the tube.

A closer examination of median inner position ratio plots at $2 \leq t \leq 6$ in figure 4.5showed

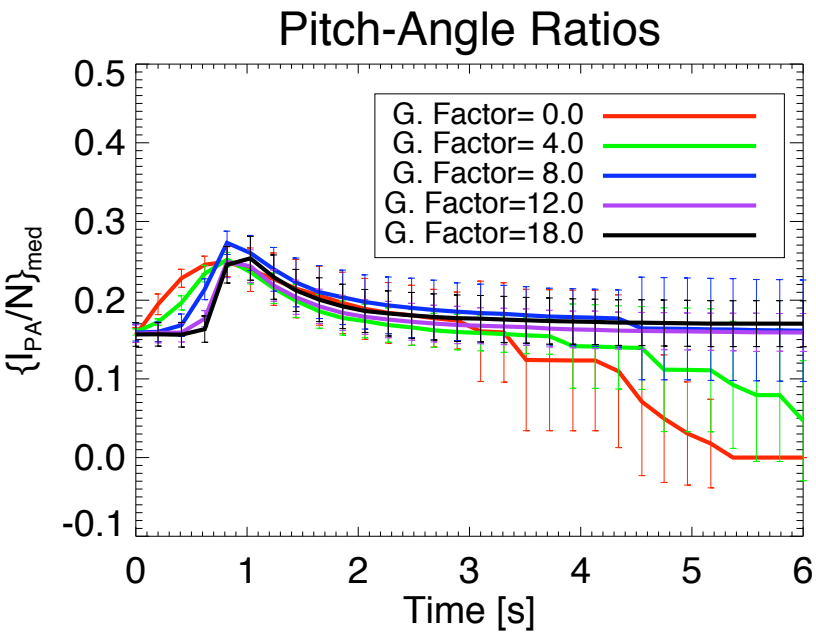

Figure 4.3: A plot showing the median values of the inner pitch-angle ratio, I_{PA}/N. Error bars were taken using a bootstrap with replacement method and represent the 95% confidence level. A completely uniform distribution would have a $\{I_{pos}/N\}\,med = 0.5$.

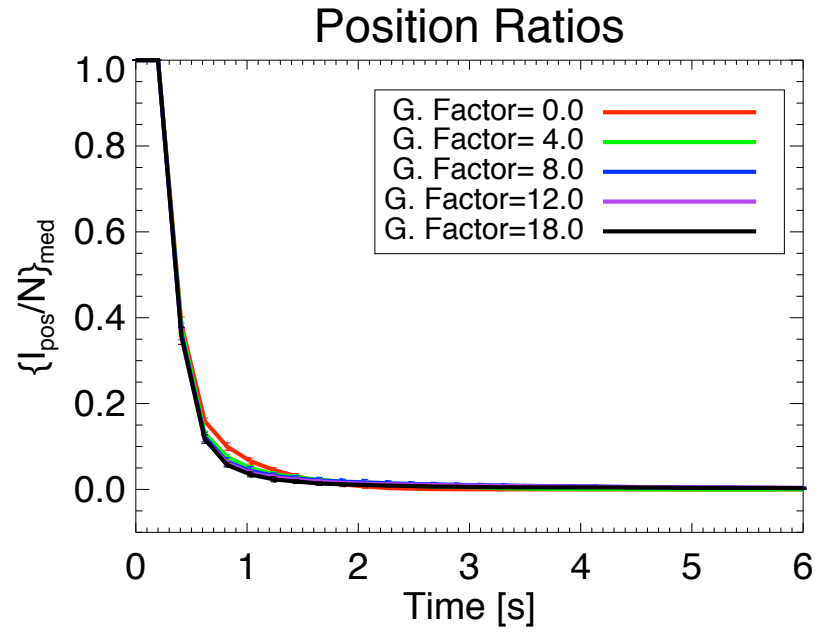

Figure 4.4: This plot shows the median values inner position ratio, I_{pos}/N, for each value of the density gradient factor as a function of time.

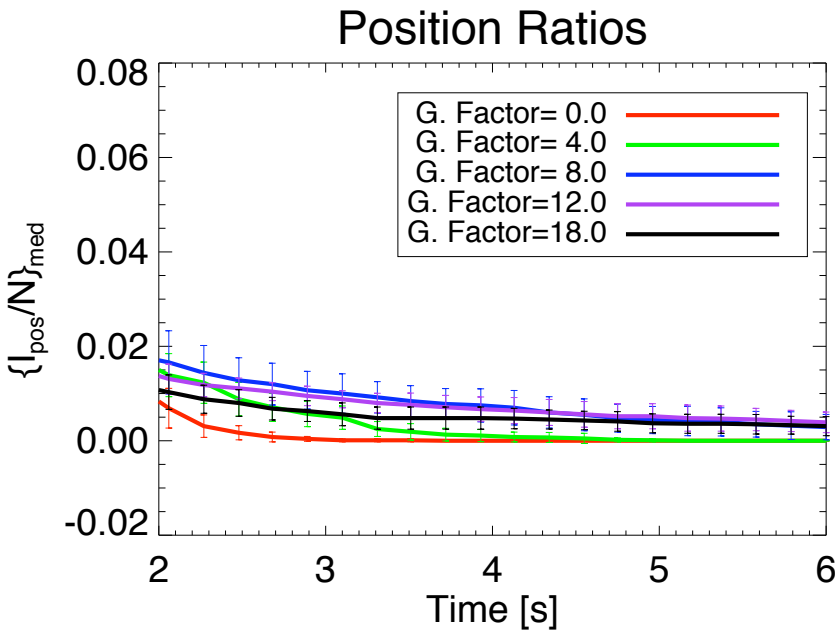

Figure 4.5: This plot is the same as figure 4.4 but zoomed in at $2 \leq t \leq 6$.

some unexpected results. The curves for gradient factor$=0$ and gradient factor$=8$ crossed. The gradient factor$=8$ curve, and 95% confidence level error bars remained higher than the gradient factor$=0$ curve and error bars. While this was not a large difference, it was more than the error on the simulation. It should also be noted that in the uniform case, no nonthermal particles thermalized within the central portion of the tube. However, a simulation with gradient factor>4 did have a small number of nonthermal particles thermalize in the central region of the tube, where the density was less for these cases.

The *beam alive times* were defined as how it took the last particle in the electron beam to become part of the thermal distribution. Taking a median of the beam alive times showed vary little variation with gradient factor, $\sim 2 \pm 2\, seconds$ for all gradient factors. The average beam alive times over all runs (as shown in figure 4.6) showed a definite trend. Such a large difference in the median and the mean values of the beam alive times was indicative of a skewed distribution.

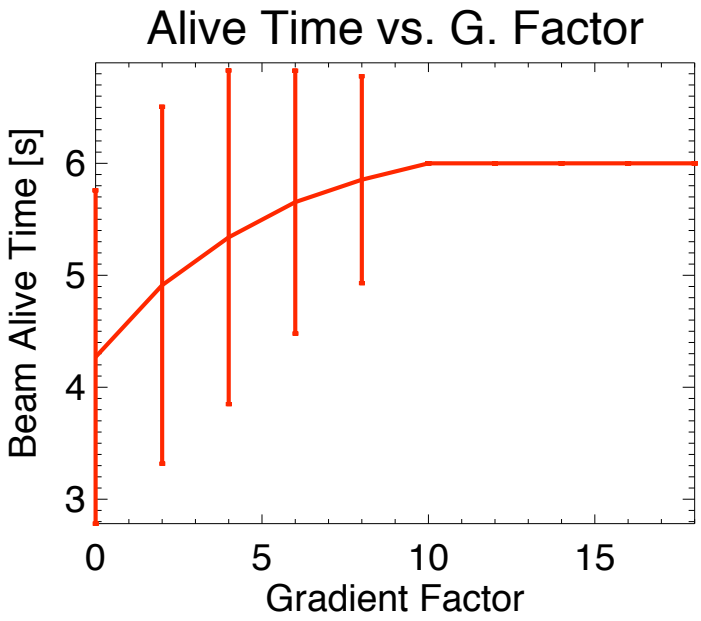

Figure 4.6: A plot showing the nonthermal beam alive times as a function of gradient factor averaged over the ten runs.

In order to better investigate how density gradients affect nonthermal particle lifetimes, the alive times for each individual particle was tracked for all runs with a given gradient factor. The skewness of these alive time distributions was then tracked and is shown in figure 4.7. From $t = 0 - 0.5\,seconds$ the alive time skew of all gradient factors was essentially zero, the skew for a uniform distribution. Before $t = 0.5\,seconds$ almost all nonthermal particles had an alive time equal to the simulation time which lead to a uniform distribution in alive times. At $t = 0.5\,seconds$ the nonthermal particles that remained highly beamed reached the ends, leaving the nonthermal distribution, and caused a skew of ~ -30 for all gradient factors. After $t = 0.5\,seconds$ the skew of each gradient factor alive time distribution grew and quickly became greater than zero. A large, positive skew in the alive time meant that the means of the distributions were larger than the medians due to a larger number of long lived particles in the tails of the distribution. The skew of the alive time distribution after $t = 0.5\,seconds$ was strongly influenced by gradient factor, as shown by

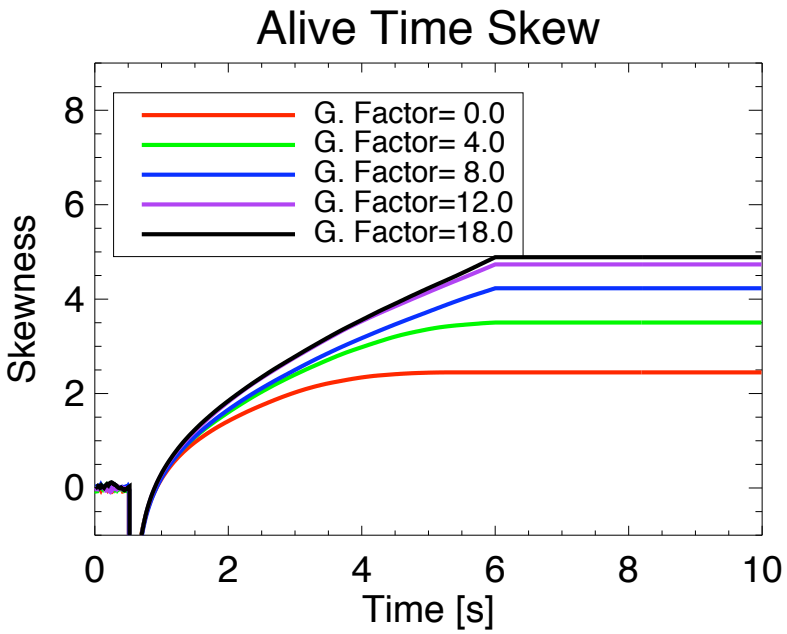

Figure 4.7: A plot showing the skew of the distribution of alive times for all runs.

figure 4.7. A stronger gradient caused more long lived outliers in the nonthermal particle distribution.

Discussion

This experiment showed that gradients in the density of a thermal plasma affected the evolution of the nonthermal electron beam. It would be tempting to think that this was cause solely by the fact the decision was made to conserve total particle number in these experiments. Due to this choice, particles with an initially small absolute pitch-angle cosine in a tube with a large density gradient factor, would scatter very little since the density was low at the injection point. Hence, they would spend more of their lifetime in the low density center of the tube, slowly releasing their energy. However, if this were the only effect then why would the $\{I_{PA}/N\}med$ curves show a higher maximum for the gradient factor= 8 than the gradient factor= 4 and gradient factor= 12 cases? The reason was that pitch-angle

cosine scattering plays an important role in the evolution of the non-thermal electron beam and the density gradient affects the amount of pitch-angle cosine scattering.

In the uniform density case, particles underwent the same amount of scattering no matter where they were located in the tube. The amount of scattering then did not depend on the pitch-angle cosine of the particle because all particles sampled the same density at all locations along the tube. Particles continued to scatter in the tube until they thermalized or scattered to a value of ptich-angle cosine that allowed them to quickly exit the tube.

In the situations where a gradient was introduced, the amount of scattering a particle underwent was a function of pitch-angle cosine. Particles with a large absolute value of pitch-angle cosine would undergo more scattering as they more quickly moved down the tube and encountered regions of higher density. As they underwent more scattering, more particles would have their absolute value of pitch-angle cosine reduced and had a larger portion of their momentum directed perpendicular to the tube axis. Particles with a $|\cos(PA)| \approxeq 0$ traveled more slowly down the tube and took much longer to reach the endpoint. In tubes with a gradient, these small pitch-angle cosine particles scattered less since they spent more time in regions of lower density. If the gradient was too steep, then there would not be enough time for many of the initially beamed particles to have undergone enough scattering to have a $|\cos(PA)| \approxeq 0$ before they were too close to the end of the tube to stop or turn around. It should be noted that $< 1\%$ of particles underwent a reversal of pitch-angle cosine, and hence velocity, in any of the simulations. The case of density gradient factor$= 8$ represents where just enough pitch-angle cosine scattering occurred before the particles moved too far down the tube, but the gradient was steep enough so that the particles with a $|\cos(PA)| \approxeq 0$ spent most of their time in a lower density regime, scattered less and changed their pitch-angle cosine and energy very slowly.

CHAPTER 5

THE EFFECTS OF DIFFERENT PITCH ANGLE DISTRIBUTIONS

The previous experiments were all conducted with a $\gamma_{PA} = -4$, representing a beamed distribution of nonthermal particles. However, the pitch-angle cosine distribution for nonthermal beams in flares is not well known and may vary from flare to flare. The effect of nonthermal pitch-angle cosine distribution on flare propertes was studied by conducting three simulations, each with different values of γ_{PA} .

Experimental Setup

For these simulations the flare loop parameters were the same as listed in table 3 on page 71. The energy power law index was also the same as the previous experiments, $\delta = 3$. The only aspect that was changed from simulation to simulation was γ_{PA}, as can be seen in figure 5.1. The flare loop parameters are listed in table 3.

Thermal Evolution

The changing of the pitch-angle distribution had a marked impact on how the thermal plasma evolved. The mean apex temperature of each simulation is shown in figure 5.2. Flaring loops with a value of γ_{PA} consistent with a less beamed distribution had a subsequent increase in apex temperatures, with the $\gamma_{PA} = 4$ case having a peak apex temperature almost three times as great as the $\gamma_{PA} = -4$ case. The reason for this increase was obvious. Highly beamed nonthermal particles ($\gamma_{PA} = -4$) deposited the majority of their energy low in the flaring loop where densities were higher. This higher density meant that the heat

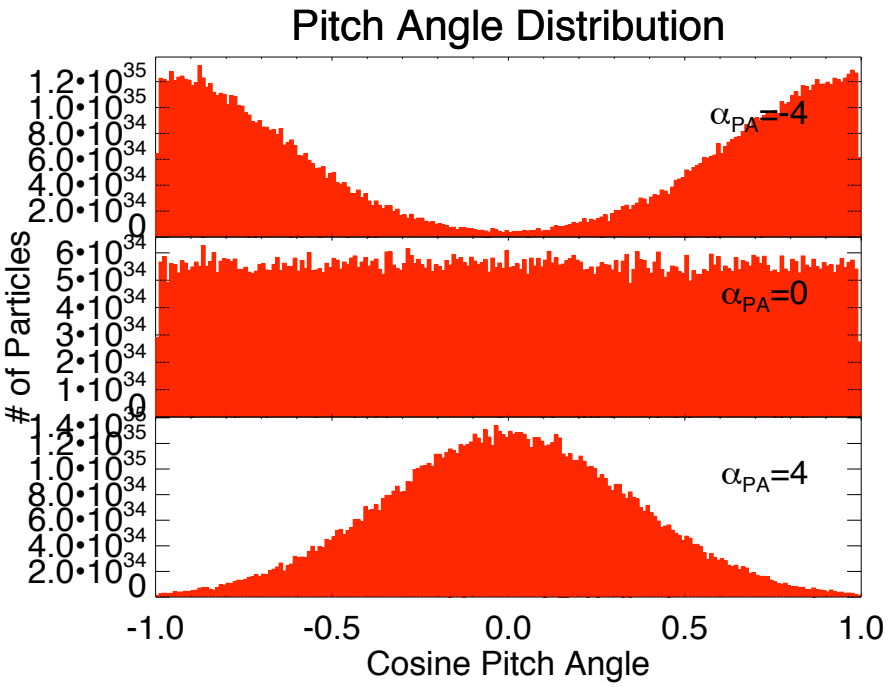

Figure 5.1: A plot showing pitch-angle cosine distributions for the three simulations to be conducted.

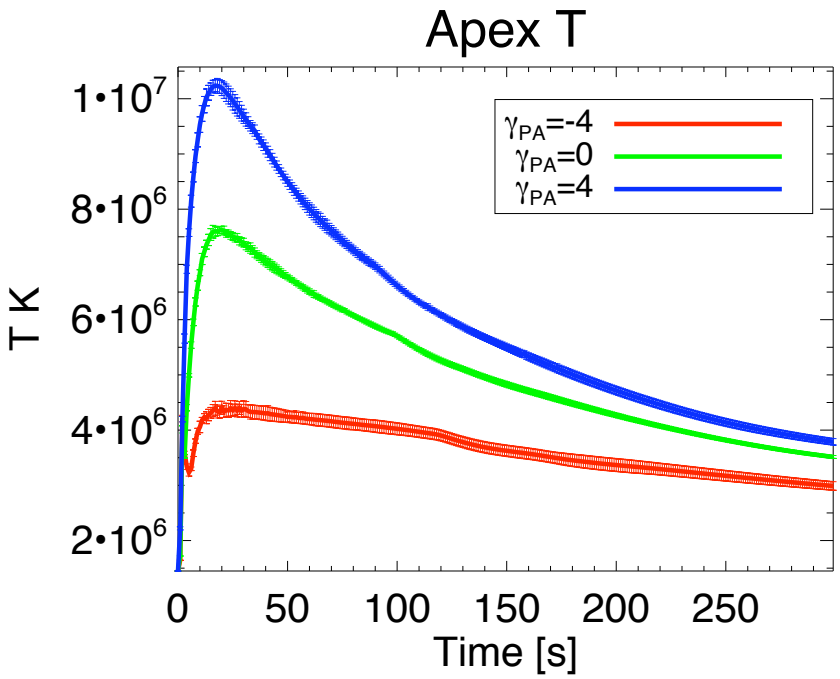

Figure 5.2: This plot shows the mean apex temperature, in kelvins, of a flaring loop for each simulation. The $\gamma_{PA} = 4$ case became almost three times as hot as the $\gamma_{PA} = -4$ case. The error bars denote one standard deviation.

capacity was higher in the regions where the highly beamed distributions were depositing the bulk of their energy thus requiring more energy to raise the temperature. Also, since radiative losses scale as n_e^2, flare loops with highly beamed nonthermal particles shed more of the excess energy influx via radiation. Figure 5.3 shows the mean radiative loss rate of each simulation as a function of time. The initial peaks of each radiative loss rate curve, at $t < 1\,second$ were due to the nonthermal particles with $|\cos(PA)| \approxeq 1$ reaching the footpoints and thermalizing quickly. For the $\gamma_{PA} = 4$, highly beamed particles represented the tails of the pitch-angle cosine distribution and were few in number. For the most part, the radiative loss rate of the $\gamma_{PA} = 4$ simulation was lower than the $\gamma_{PA} = -4$ case. The excess energy for $\gamma_{PA} = 4$ could not be radiated away and went in the heating of the plasma instead.

The temperature was not the only thermal plasma property to be dependent on the pitch-

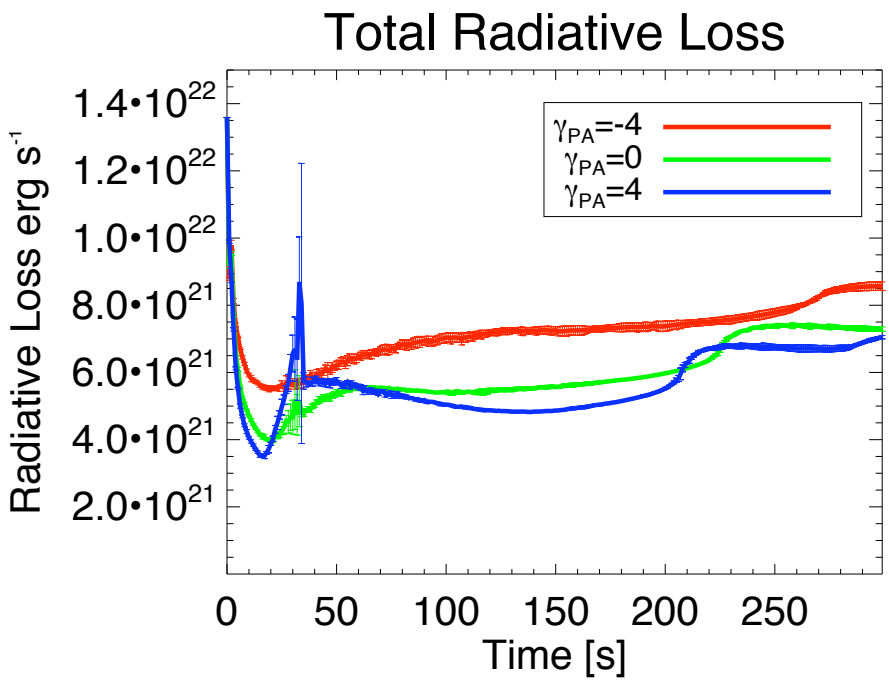

Figure 5.3: This plot shows the mean radiative loss rates, as a function of time, for each of the simulated cases. The error bars denote one standard deviation.

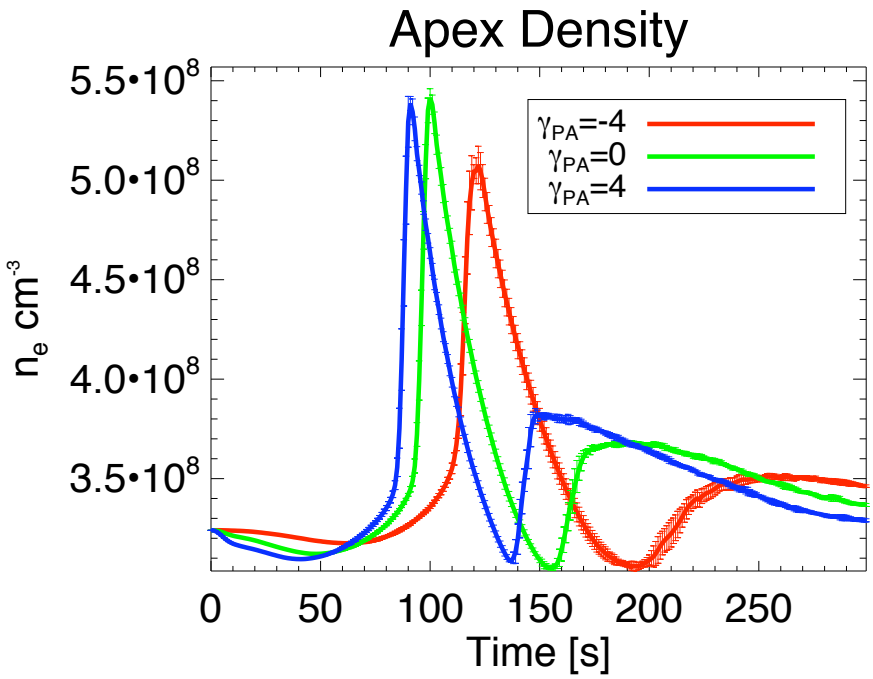

Figure 5.4: This plot shows the mean apex thermal electron density for each simulation. The maximum density enhancement of the $\gamma_{PA} = 4$ came nearly a minute before the $\gamma_{PA} = -4$ case.

angle distribution. The differences in temperature in the location of energy deposition, also caused a change in the mass motions of the thermal plasma. The faster flows in the $\gamma_{PA} = 4$ case caused a density enhancement in the flare loop apex, before the $\gamma_{PA} = 0$ or $\gamma_{PA} = -4$ cases as can be seen in figure 5.4. The magnitude of these enhancements did not vary much from case to case. However, the differences in time for the maximum apex temperature hardly varied at all. A comparison of peak apex temperature onset to peak apex density onset in observations of real flares, may provide clues to the initial nonthermal pitch angle distribution without observing the nonthermal particles directly via HXR measurements.

SXR Signatures

With the temperatures and densities calculated for each case, responses were calculated

for broadband imaging telescopes using the procedure described on page 60. In order to provide a signal that could be directly compared to real observations, the ratio of apex to footpoint SXR emission was taken in the Ti-Poly, Thin Beryllium and Thick Beryllium filter channels of the X-ray Telescope (XRT; *Golub et al.*, 2007) onboard the *Hinode* satellite. Figures 5.5, 5.6, & 5.7 show the emission in the three filters for the $\gamma_{PA} = -4, 0, 4$ pitch-angle cosine distributions respectively. The white boxes in each represent the points where footpoint and apex emission measurements where taken and the plot at the bottom of each figure shows the apex to footpoint emission ratio for each case as a function of time. The blue contours show the $3-6\,keV$ HXR emission at the 80% and 90% levels. Figure 5.8 shows the SXR signal ratios separated by filter channels.

A close examination of figure 5.8 showed that the pitch-angle cosine distribution had a strong effect on the signal ratio while the effect in each filter was fairly similar except for magnitudes. The highly beamed $\gamma_{PA} = -4$ case had a mild peak at $t \approx 40\,seconds$ followed by a much stronger peak at $t \approx 130\,seconds$. The $\gamma_{PA} = 0$ case also had a double peaked structure, but with a strong peak followed by a milder peak. The $\gamma_{PA} = -4$ case was the only one with an initial ratio > 1, bigger than either of its peaks, followed by a strong-mild double peak structure. Each case had a unique signature in apex to footpoint signal ratio that was easily distinguishable from the others. This shows that the initial pitch-angle cosine distribution can not only have a drastic effect on flare dynamics, but that it also leads to signals that can be detected by broadband, SXR imagers.

HXR Signatures

HXR emission was also calculated for the $\gamma_{PA} = 0$ and $\gamma_{PA} = 4$ cases, just had been done for the $\gamma_{PA} = -4$ case on page 86. Figures 5.9-5.12 show emission in the $3-6\,keV$ energy passband for different times during the simulation and binned intervals for the $\gamma_{PA} = 0$ case.

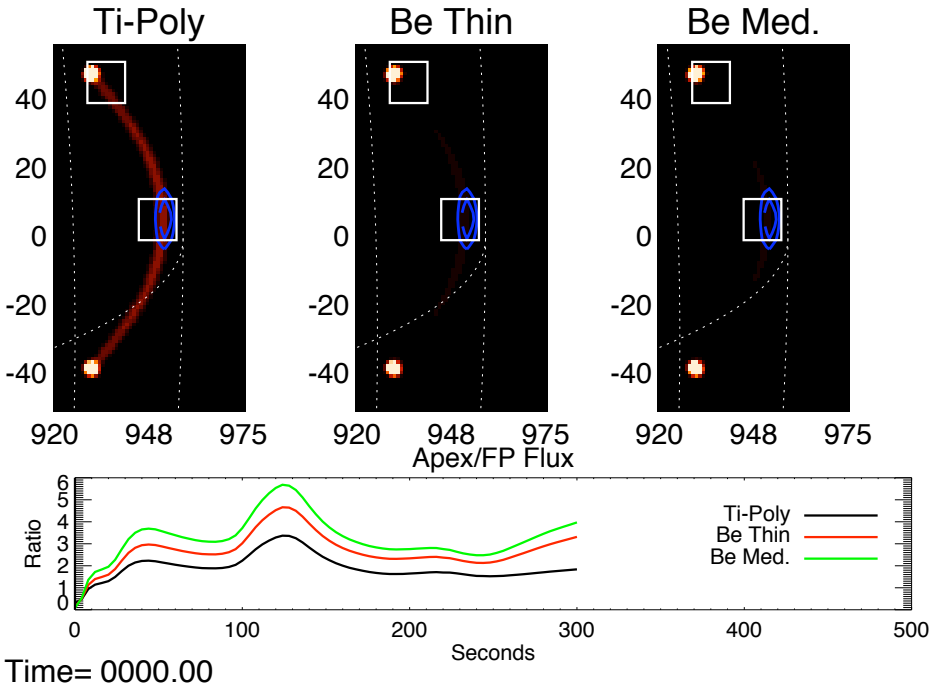

Figure 5.5: This plot shows the emission in XRT filter channels for the $\gamma_{PA} = -4$ pitch-angle cosine distribution case. The plot at the bottom of the figure the apex to footpoint emission ratio for each case as a function of time.

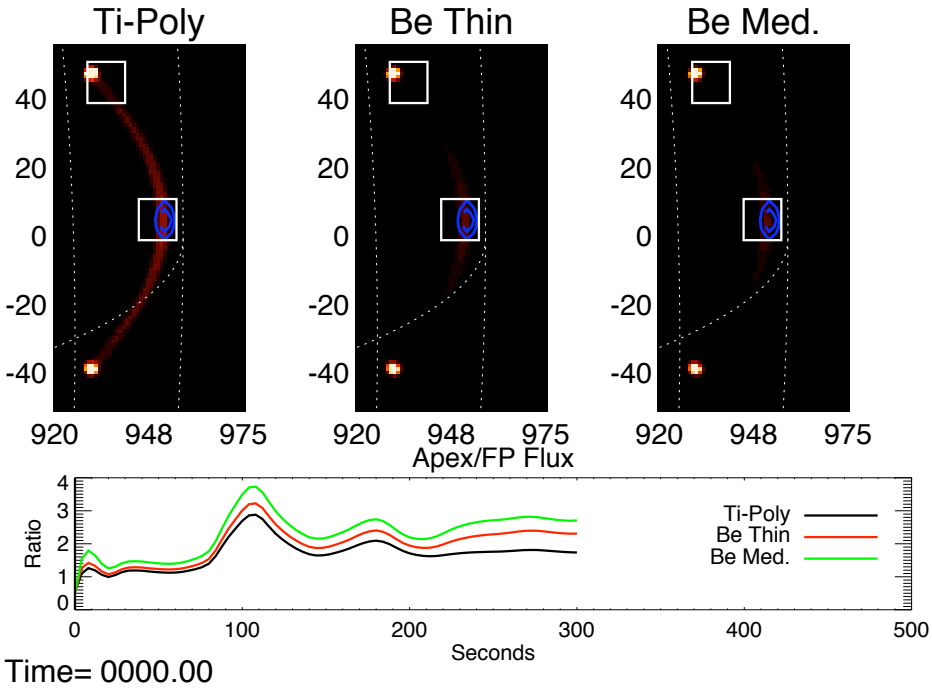

Figure 5.6: This plot shows the emission in XRT filter channels for the $\gamma_{PA} = 0$ pitch-angle cosine distribution case. The plot at the bottom of the figure the apex to footpoint emission ratio for each case as a function of time.

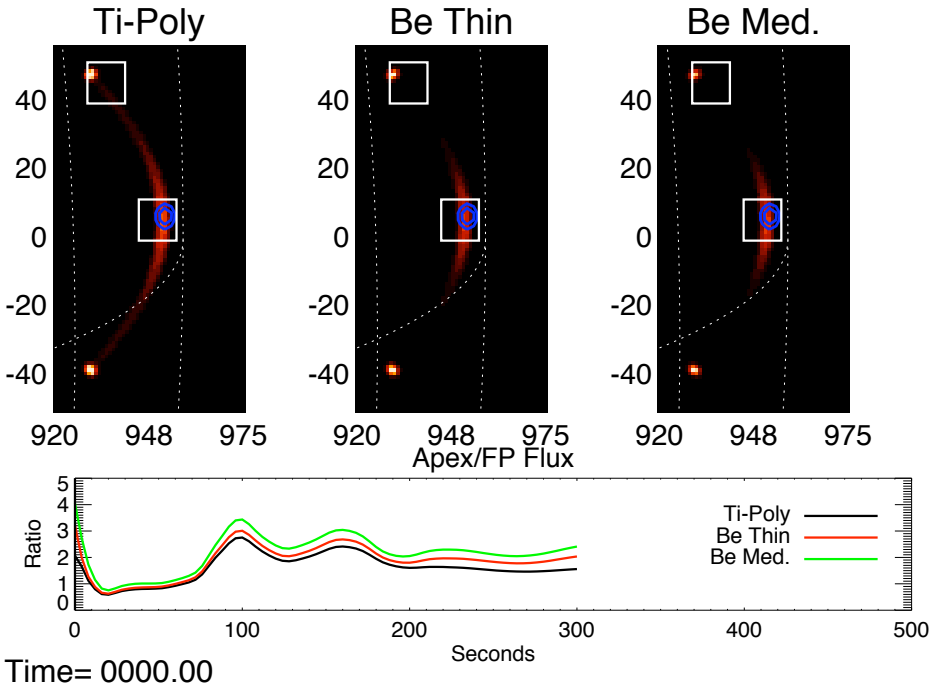

Figure 5.7: This plot shows the emission in XRT filter channels for the $\gamma_{PA} = 4$ pitch-angle cosine distribution case. The plot at the bottom of the figure the apex to footpoint emission ratio for each case as a function of time. NB This was the only case that showed an initial peak in apex to footpoint emission ratio.

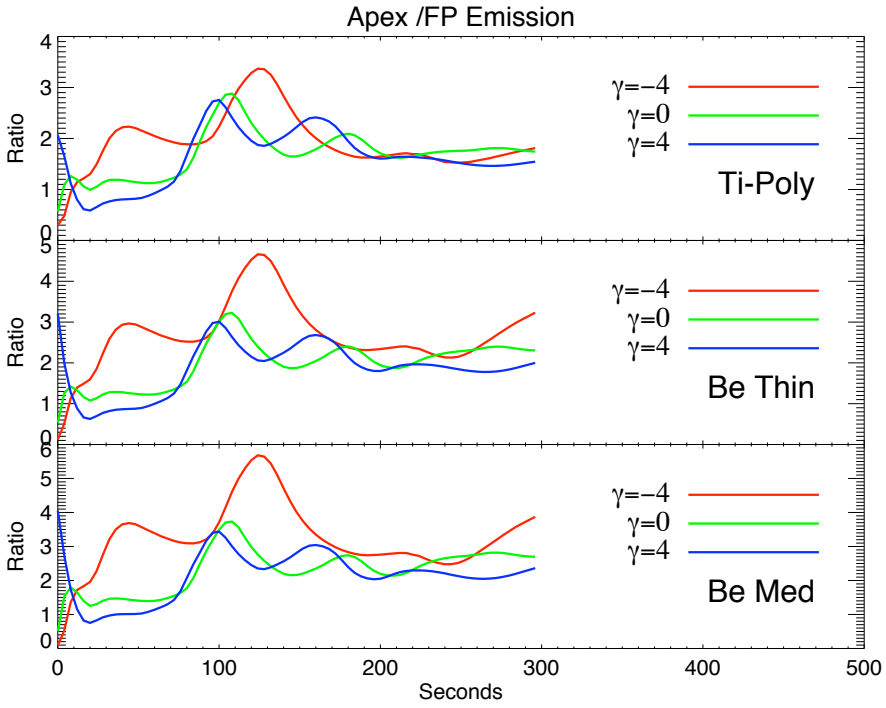

Figure 5.8: This plot shows the apex to footpoint emission ratio for each filter channels. While the ratios differed slightly in magnitude from filter to filter, the obvious signal was the time profile of the ratio.

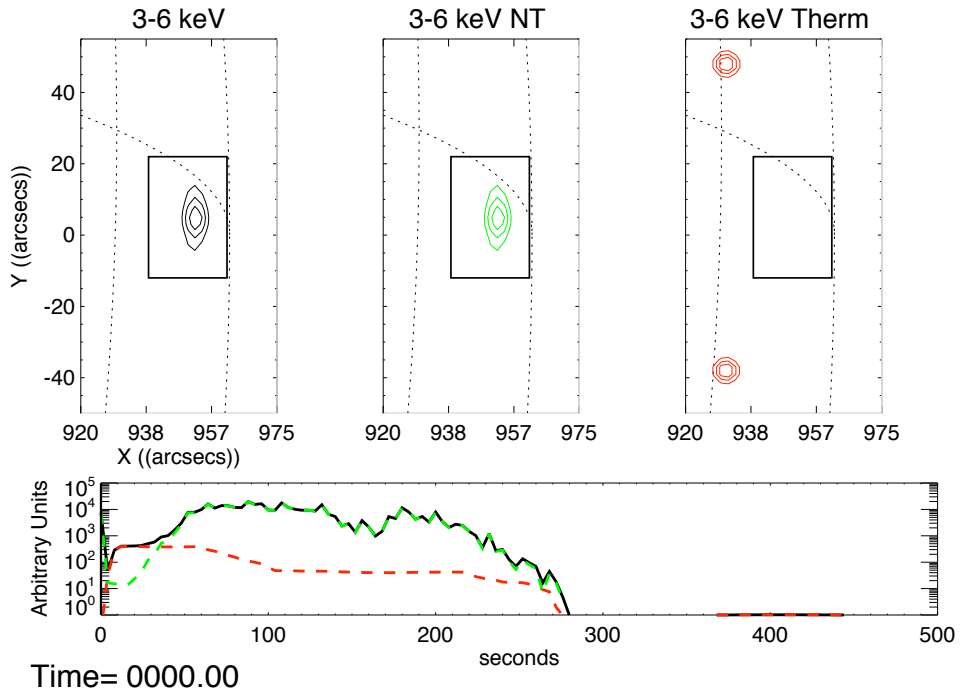

Figure 5.9: This plot shows the HXR emission for the $\gamma_{PA} = 0$ case in the $t = 0-4$ time bin. The bottom plot shows the total apex emission as defined by the bounding box as a function of time with the nonthermal signal in green, the thermal signal in red, and the total signal in black.

Figures 5.13-5.16 show the same but for the $\gamma_{PA} = 4$ case.

Both cases had a far shallower initial dip in apex HXR emission than the $\gamma_{PA} = -4$ case. This was due to a much stronger thermal signal at the apex early in each simulation. This stronger thermal signal was due to the plasma in both simulations being significantly hotter than the $\gamma_{PA} = -4$ simulation. Both the thermal and nonthermal emission of the $\gamma_{PA} = 0$ simulation dropped steeply at $t \approx 280\,seconds$. In the $\gamma_{PA} = 4$ simulation, the thermal signal decayed slowly, while the nonthermal emission remained fairly steady for many minutes. This was not surprising since most of the nonthermal particles in the $\gamma_{PA} = 4$ case had momentum perpendicular to the loop axis, and were rarely scattered far from a pitch-angle cosine close to zero.

Note again the tight sources of $3-6\,keV$ HXR emission in figures 5.9-5.16. As was

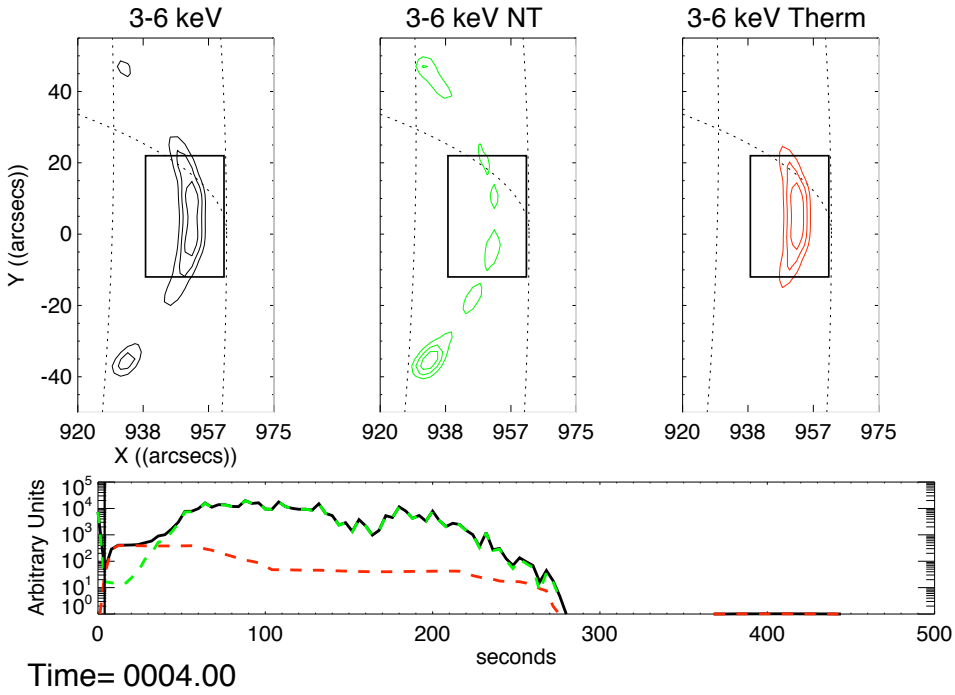

Figure 5.10: This plot shows the HXR emission for the $\gamma_{PA} = 0$ case in the $t = 4 - 8$ time bin.

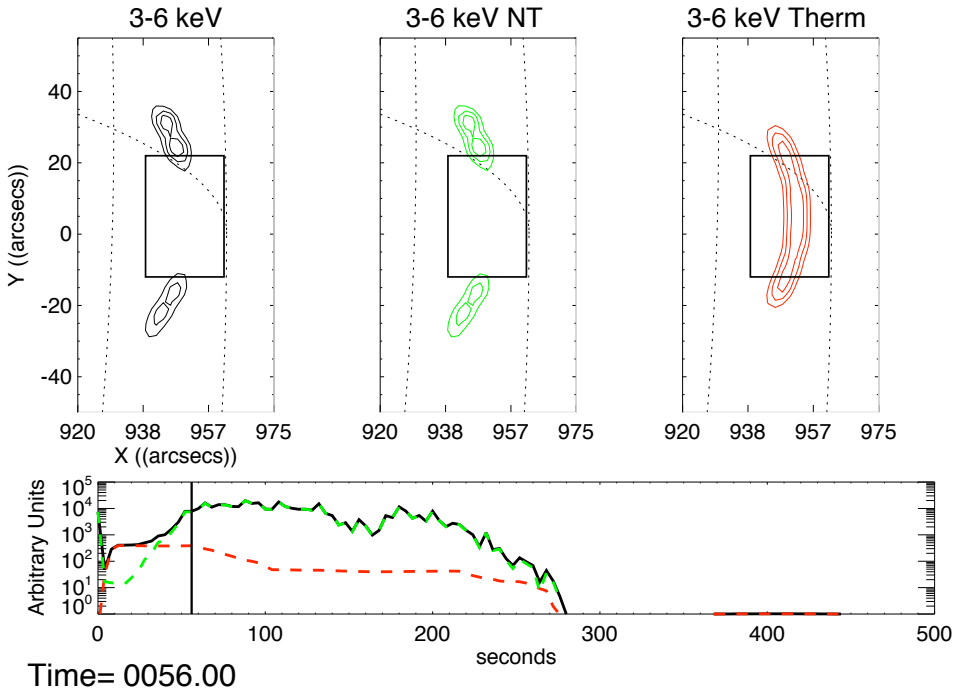

Figure 5.11: This plot shows the HXR emission for the $\gamma_{PA} = 0$ case in the $t = 52 - 56$ time bin.

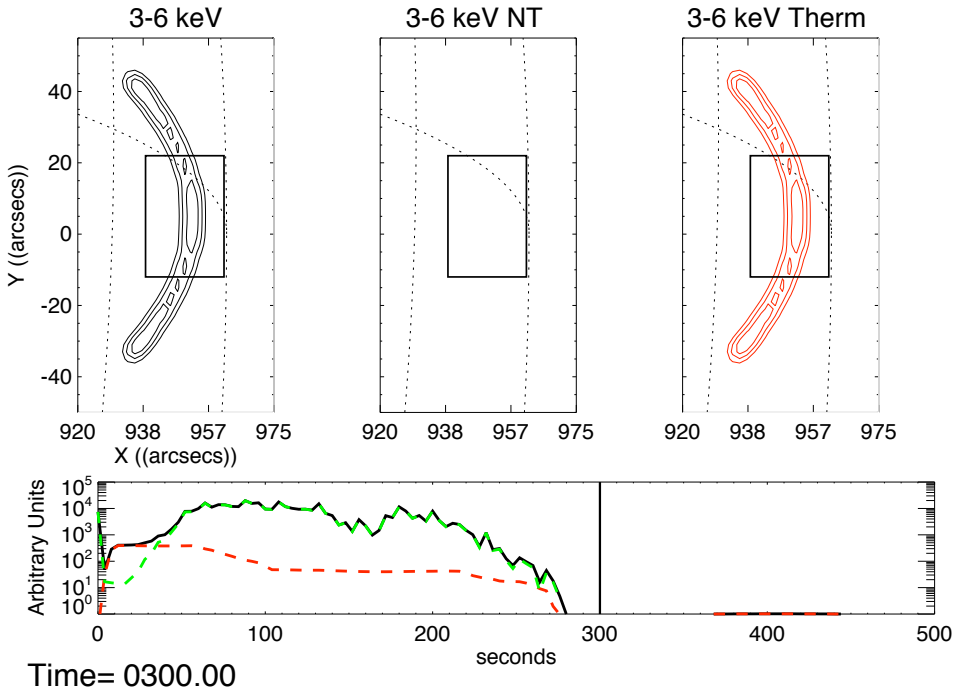

Figure 5.12: This plot shows the HXR emission for the $\gamma_{PA} = 0$ case in the $t = 296 - 300$ time bin.

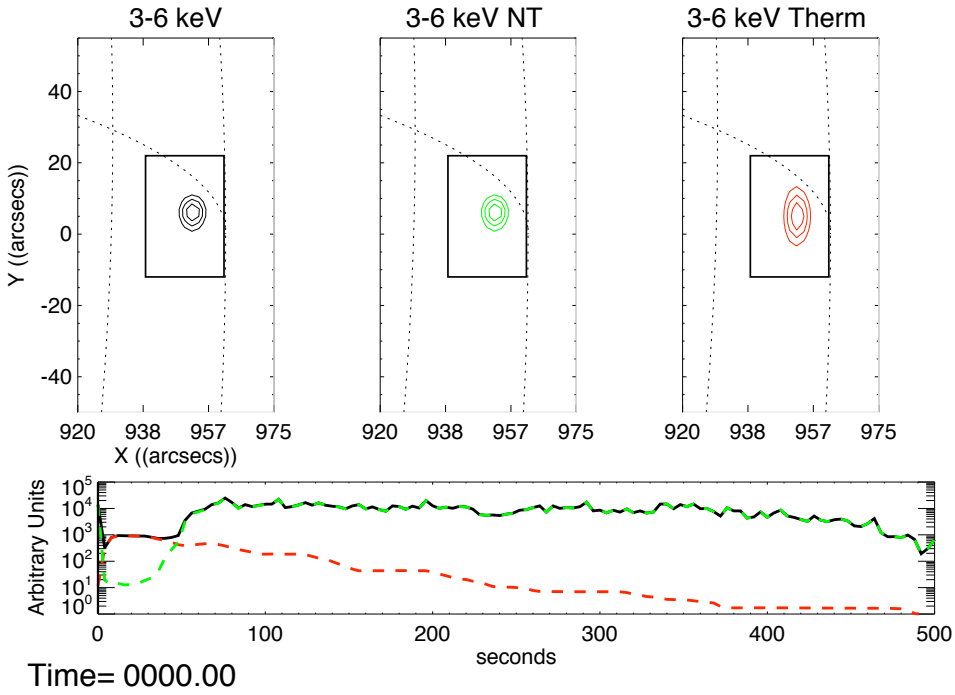

Figure 5.13: This plot shows the HXR emission for the $\gamma_{PA} = 4$ case in the $t = 0-4$ time bin.

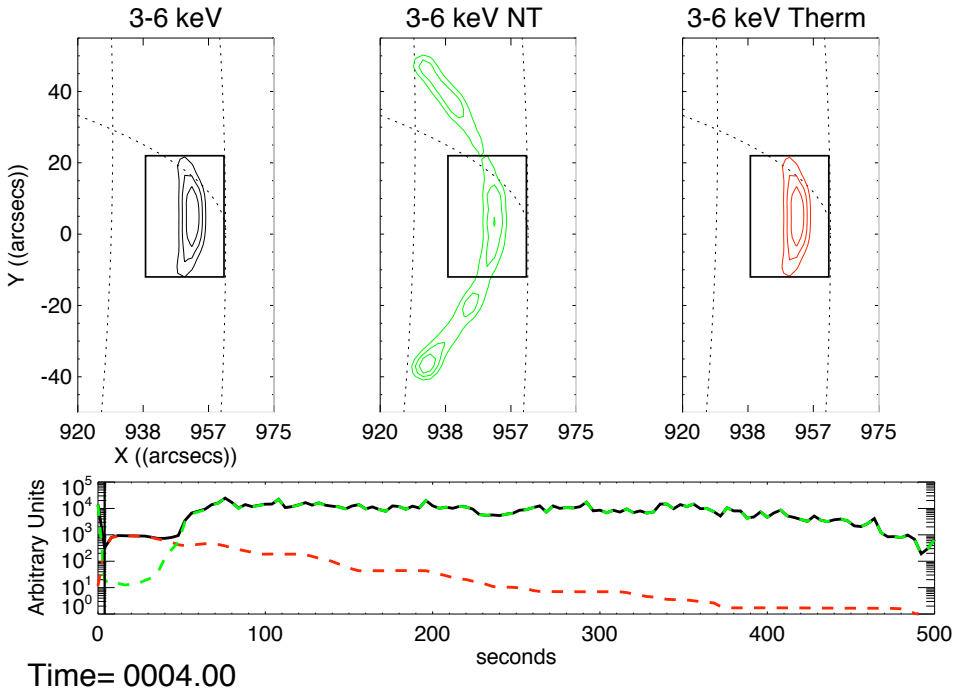

Figure 5.14: This plot shows the HXR emission for the $\gamma_{PA} = 4$ case in the $t = 4 - 8$ time bin.

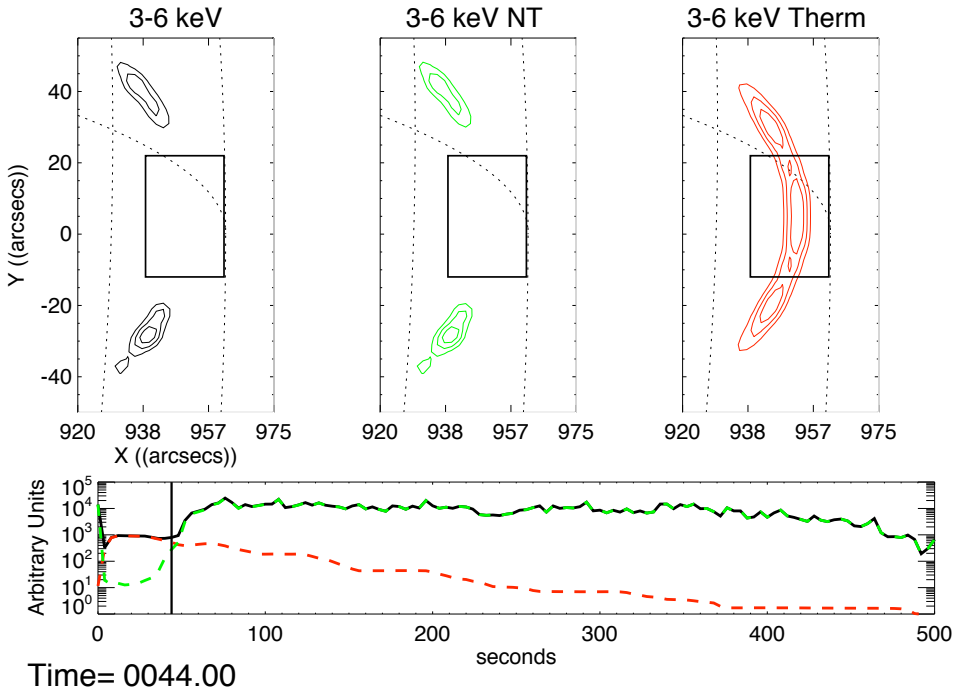

Figure 5.15: This plot shows the HXR emission for the $\gamma_{PA} = 4$ case in the $t = 40 - 44$ time bin.

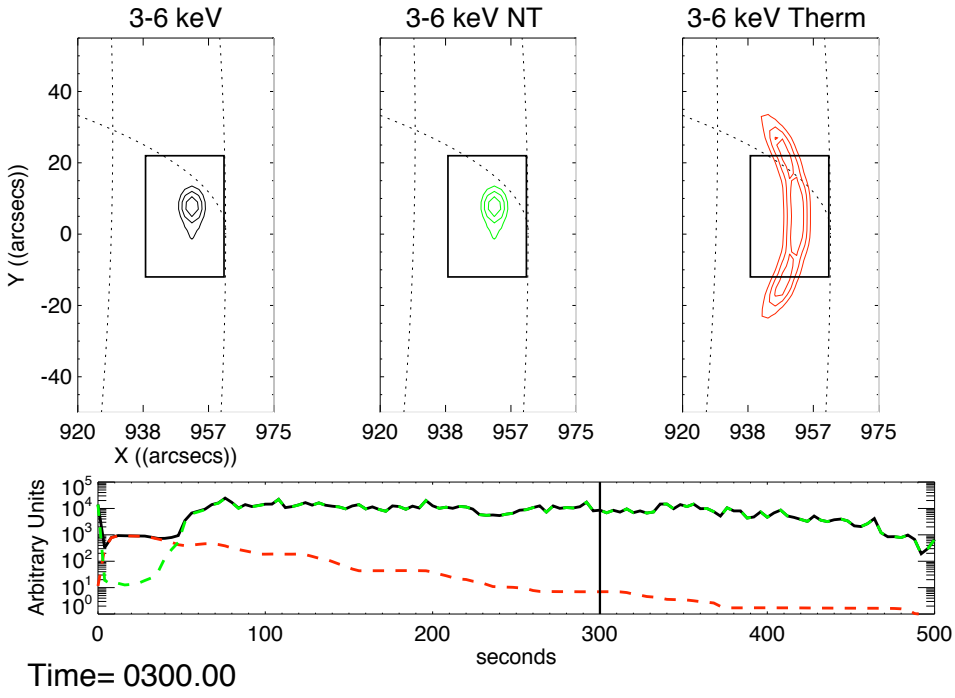

Figure 5.16: This plot shows the HXR emission for the $\gamma_{PA} = 4$ case in the $t = 296 - 300$ time bin.

the case for $\gamma_{PA} = -4$, these sources started at the loop apex, moved down the loop legs, then climbed back up to the loop apex to form a compact, long-lived HXR source. The sources in the $\gamma_{PA} = 0$ case were often too smeared to make an accurate determination of location. However, the sources did become compact at the foot points and apex. The time it took for the source to travel from the footpoints to the loop apex corresponded to an upward velocity of $\sim 2.0 \times 10^7 cm\,s^{-1}$. This was slower but the same order of magnitude as the upward velocity reported by *Sui et al.* (2006). The sources in the $\gamma_{PA} = 4$ case had an upward velocity of $\sim 5.4 \times 10^7 cm\,s^{-1}$, only slightly larger than the velocity reported by *Sui et al.* (2006)! This shows that the moving sources seen in the early impulsive flare observed by *Sui et al.* (2006) may have been caused by an apparent motion due to the nonthermal electron beam's pitch-angle cosine distribution evolving in time.

CHAPTER 6

CONCLUSION

Discussion

In this work a new set of simulation codes, HYLOOP, was introduced that combined a 1D hydrodynamics code with a stochastic nonthermal particle tracker in order to improve the simulations of flaring loop structures on the sun and the puzzling emissions they produce at their apexes. A large fraction of this work was spent explaining the assumptions that went in the the codes' construction and applying proof of concept and evaluation tests to the components of the code. This was fitting and proper when introducing a new code and is a step often overlooked in the refereed literature where the pressures to publish new results are strong.

In addition to the description of a new code, a question of scientific importance was asked: does the addition of a hydrostatic atmosphere have an effect on the evolution of a nonthermal particle beam? Following strict scientific rigor, the null hypothesis explicitly stated the hydrodynamic atmosphere would not affect the nonthermal particle beam any differently than a static atmosphere. The hypothesis was tested by monitoring a series of test variables that would be used to monitor the evolution of the nonthermal beam. Realistic images of hard X-ray emission were synthesized in the $3-6\,keV$ bandpass. A region at the loop apex was defined and the emission in that region was totaled to provide a useful proxy of nonthermal particle evolution that is comparable to available datasets. The data was carefully analyzed and a Kolmogorov-Smirnov test was performed to test the differences between data samples taken from the dynamic and static atmosphere simulations.

The samples were found to come from different distributions with a high degree of confidence, $> 95\%$ for most times in the simulation. The static atmosphere's distribution of HXR flux in time, as expressed by light curves, was also shown to be significantly different the dynamic atmosphere's. This provided quantitative evidence that the inclusion of hydrodynamic effects is very important in the understanding of nonthermal particle evolution.

The effects of density gradients on nonthermal particle evolution was also investigated. It was found that a strong density gradient caused a larger, positive skew in the nonthermal lifetime distribution of injected electron beams. There was also a specific gradient factor, 8, that corresponded to a density gradient that maximized the number of particles with a small pitch-angle cosine and also maximized the number of nonthermal particles that thermalized in the central portion of the loop. This proved that strong density gradients skew the distributions of nonthermal particles' lifetimes.

This work showed how and why different distributions of nonthermal particles can affect the thermal properties of flares. The emission in several XRT filter channels was analyzed and it was found that different distributions produced easily recognizable signals in this instrument. This is an important result that can be utilized when the Sun approaches its next period of enhanced activity.

This work also provided a competing explanation for the observed motion of HXR sources in an early impulsive phase loop. While this work cannot reject the SHS hypothesis posed by *Sui et al.* (2006) for the 2008 November 28 flare, it does show that this hypothesis is invalid for simulated loop. It also, amazingly, showed that the upward speeds of the HXR sources in the simulation could be made comparable to the velocities measured by *Sui et al.* (2006) by simply changing the pitch-angle cosine distribution. This unique result was not the original intent of the simulations in this work. It was a serendipitous result that showed the utility of a code that combines the proper physics to govern evolution of both thermal and nonthermal distributions of particles. It also showed that this code

can reproduce observed features of flares in a manner that is directly comparable to those observations. HYLOOP provides a unique laboratory to test theories of nonthermal particles in flaring loops and compare the results to real data.

Future Studies

This work is primarily provided proof of concept of a new numerical model which restricted the scientific question being asked to a fairly simple one. However, with the code thoroughly tested and the code's core concept validated, a wide range of physically meaningful situations can be simulated and tested.

Alfvén Wave Acceleration of Particles

For over forty years many theories have been proposed to explain the generation of nonthermal particles in a flaring region. Modeling the acceleration of particles near magnetic X-points has been successful in producing nonthermal particles of high enough energy (*Hannah and Fletcher*, 2006; *Hamilton et al.*, 2003), and the proper energy spectrum (*Fletcher and Petkaki*, 1997; *Heerikhuisen et al.*, 2002) to match observations of solar flares. The acceleration of nonthermal particles near an X-point has also been observed in laboratory plasmas (*Brown et al.*, 2002). Yet with all of these successes this model shares a fundamental shortcoming with all other models that have the acceleration region at the apex of the flaring flux tube. Thick-target modeling of observations in UV and X-ray suggests that the number of particles accelerated out of a thermal distribution is quite high compared to the number available in the corona. Work by *Hannah and Fletcher* (2006) suggest that the number of electrons that this model can accelerate is six orders of magnitude too low to explain large flares! This supposed "number problem" has encouraged theorists to look for other sources of nonthermal particles. Since the particle density is

orders of magnitude larger in the chromosphere than in the corona, some theorists are looking to that layer as a source of nonthermal particles for flares. The main thrust of this work is explaining how the energy from the reconnection site, which is still agreed to be in the corona, is transmitted to the chromosphere where number densities are higher. *Fletcher and Hudson* (2008) suggest that the energy necessary for the acceleration of the nonthermal particles comes from the large scale restructuring of the magnetic field and is transferred to the chromosphere via inertial Alfvén waves. These waves would dissipate in the lower corona or chromosphere, and transfer their energy in regions where the particle densities are high. In the model proposed by *Fletcher and Hudson* (2008), Alfvénic perturbations can lead to field aligned electric fields in the non-ideal MHD limit that can accelerate particles out of the thermal distribution, and the dissipation of these perturbations leads to secondary acceleration mechanisms such as first order Fermi acceleration (*Fermi*, 1949) and stochastic acceleration via turbulent waves (*Melrose*, 1974; *Miller and Ramaty*, 1987; *Miller*, 1997). Some recent observations may support this model. Joint observations carried out by *Fletcher and Hudson* (2007) observed hard X-ray and White Light/Ultra-Violet (WL/UV) continuum emissions from nine flares observed by both *RHESSI* and *TRACE*. They found that the nonthermal electron beam intensity inferred by thick-target hard X-ray models of the footpoints has to be $4-10$ times stronger to explain the WL/UV emission (*Fletcher and Hudson*, 2007). We offer a possible explanation for this discrepancy in the context of *Fletcher and Hudson* (2007). While the electron beam inferred by the hard X-ray footpoints is not enough to power the UV/WL emission, it would be enough to excite a population of electrons out of the thermal distribution and to energies of a few keV. At this energy range gyro-resonant stochastic mechanisms become efficient particle accelerators (see *Aschwanden* (2005) sec. 11.4.2 for a review). In essence the initial nonthermal beam provides a seed population that the mechanisms proposed in *Fletcher and Hudson* (2008) can act upon. The low energy cutoff for this new distribution would presumably be

lower than the initial nonthermal beam, i.e., thermalized quickly providing localized heating, and if the power law were soft enough then these new nonthermal particles would not contribute significantly to the hard X-ray emission, explaining the discrepancy in *Fletcher et al.* (2007b). This model, while enticing on many levels leaves open several questions that need to be addressed by theorists and modelers. These questions include, but are not limited to: 1. What fraction of the flare energy goes into the production of inertial Alfvén wave perturbations and how efficiently can these disturbances accelerate particles? 2. What energy spectrum of nonthermal particles would be produced by these perturbations? The HYLOOP codes offer a unique laboratory to address these questions. We propose a simple first step in the simulation of the effects of wave accelerated nonthermal particles. In this first set of simulations total energy budgets for flares will be determined either observationally, as in *Sui et al.* (2005a), or by computing the energy difference in the energy contained in the magnetic field pre- and post-flare as in *Des Jardins et al.* (2008), or a combination thereof. The ratio of the energy used in accelerating nonthermal particles to the energy that goes directly into heating the loop will be a free parameter that is adjusted for each simulation run. Nonthermal particles will be drawn from an energy probability distribution that is a simple power law, $F(E) = F_0 E^{-\delta}$, with δ providing another dimension in parameter space to search. In the experiments described in this work, all nonthermal particles were assumed to be injected at the loop apex. In the proposed experiments injection locations will be randomly drawn from a probability distribution that is proportional to the Alfvén energy, $E_A = {}^{m_e}/_{2}v_a^2$ (*Fletcher and Hudson*, 2008). The emission signatures from each simulation will be calculated and compared to real observations from *RHESSI*, *XRT*, and *TRACE*. This ability to produce realistic synthetic images will allow for the direct comparison of the simulations to the work of *Fletcher et al.* (2007b).

Code Improvements

Improved Test Particle Sampling

One of the strengths of Monte Carlo techniques is that the error on a result can be reduced to an arbitrary fractional accuracy by repeating the experiment until s_{N-1} falls below a desired value. However, since $s_{N-1} \sim (N-1)^{-1/2}$ reducing the error can be a time consuming process requiring ~ 100 times more runs for a 10% increase in accuracy (*Murthy*, 2001a). Importance sampling can alleviate this situation somewhat. However, importance sampling undersamples the tails of the distribution. In this work it was shown that the tails of the distribution were relatively unimportant for the hydrodynamic evolution of the flare, which is why they were undersampled. However it was shown that the tails did make a significant impact on the Monte Carlo estimators for the HXR emission. In this experiment only basic importance sampling techniques were used. There is a wide range of literature on more advanced importance sampling techniques that may improve the sampling of the tails while still allowing a quick convergence of the hydrodynamic variables which are not tail dependent.

The slow convergence can also be relieved somewhat by using quasi-random numbers to define the random distributions. Quasi-random number sequences, such as the *Sobol Sequence*, have been shown to change the scaling of the standard deviation to N^{-1}(*Press*, 2002). Figure 6.1 shows how using Sobol numbers can increase the fractional accuracy of the Monte Carlo calculation of π while using fewer random number pairs than if the pairs where drawn from a random normal distribution. In this experiment a fractional accuracy of 10^{-3}% requires $\sim 10^6$ random normal pairs while it only requires $\sim 10^3$ Sobol pairs. Modifications to the nonthermal beam generating procedures to allow for the particles to be drawn from distributions defined by quasi-random distributions are currently underway.

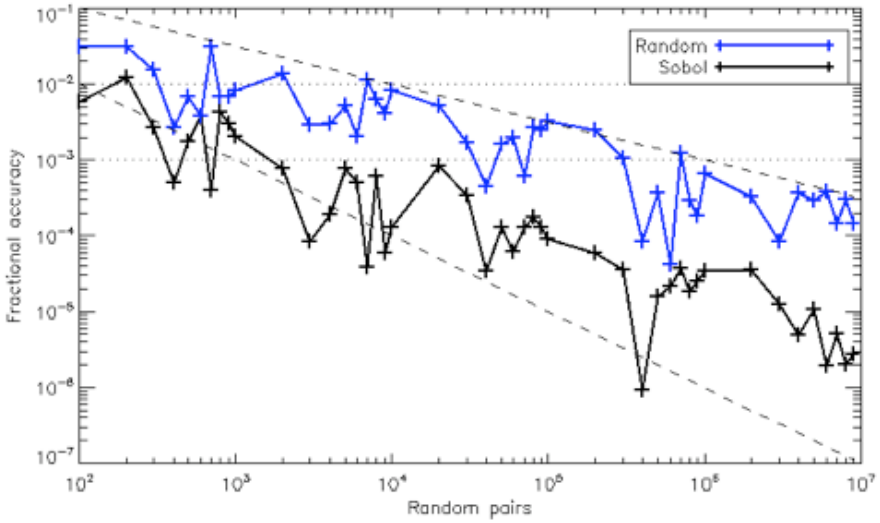

Figure 6.1: This plot illustrates how the use of Sobol numbers can increase the fractional accuracy the Monte Carlo calculation of *pi* while using fewer pairs of random numbers. The upper dashed line represents $N^{-1/2}$ while the lower dashed line represents N^{-1}. The blue line charts the fractional accuracy as a function of number of uniformly distributed random pairs, which matches the $N^{-1/2}$ line well. The black solid line is the fractional accuracy as a function of number of Sobol pairs. While the Sobol pairs do not exactly track the N^{-1} trend they do show an orders of magnitude improvement over uniform pairs.

CUDA Programming

Stochastic simulations with test particles require a large number of particles in order to have simulations converge quickly. One of the challenges of designing the current HYLOOP suite of codes was balancing the need for including enough test particles to provide a meaningful simulation with restricting the number of test particles so that the codes could run on the current available computer resources in a reasonable amount of time, $< 1\,week/run$.[1] The limitation of the number of test particles that can be used seriously limits the number of scientific questions that can be addressed by this code. Of course, running these codes on supercomputer clusters is the preferred way of solving this problem and would make the addition of millions of test particles per simulation seem trivial. However, this would put the codes out of reach of researchers at small universities and limit its use. Also, designing a code for supercomputer use is non-trivial. One affordable solution to this problem is the implementation of the Compute Unified Device Architecture, CUDA^{TM} , into the simulation code.

CUDA and its rival architecture, OpenCL, allow for codes to access a computer's graphics processing unit (GPU). GPUs are massively multi-cored processors that are designed to handle thousands of processing threads simultaneously. Previously their use in scientific applications has been limited due to their limited numerical precision. However, current models have the ability to use $64\,bit$, double precision floats making them accurate enough for scientific use.

CUDA has been used in conjunction with numerous scientific simulations. For N-Body gravitational interaction simulations *Belleman et al.* (2008) found that CUDA utilizing a NVIDIA GeForce 8800GTX GPU could decrease the time of a $65,536$ particle simulation by 148 times when compared to a $3.4\,GHz$ Xeon processor. This increase in processing

[1]The computers available to the author include a mix of MacIntosh Quad Core MacPros and Sun Quad Core machines. Codes had to be written in a way to minimize the effort involved in installing software on a multitude of machines and to facilitate syncing data structures between all machines.

speed, good numerical precision, and relative low cost of GPU cards make programming in CUDA an exciting prospect.

APPENDIX A

LIST OF SYMBOLS

α_D Pitch angle free parameter. Changing this parameter changes the probability distribution that the non-thermal particle pitch angles are drawn from. [*Dimensionless*]

α_H Temperature exponent of the power law heating function of *Martens* (2008), [*Dimensionless*]

α_{PA} Pitch angle, [*radians*]

β_H Pressure exponent of the power law heating function of (*Martens*, 2008), [*Dimensionless*]

ψ Non-thermal particle scattering angle, [*radians*]

μ_{rm} Reduced mass of a system [*grams*]

μ_B Magnetic moment $\left[g^2 cm^2 sec^{-2} Gauss^{-1}\right]$

λ_{mfp} Mean free path, [*cm*]

Λ_p Ratio of the boundaries on the spatial integral around the test particle where interactions take place, $\frac{b_{max}}{b_{min}}$, [*Dimensionless*]

Λ_{rad} Radiative loss function, $[ergs\, cm^3\, s^{-1}]$

c_s Sound speed, $\left[cm\, s^{-1}\right]$

E_H Volumetric heating rate, $[ergs\, cm^{-3}\, s^{-1}]$

E_R Radiative loss rate $[ergs\, cm^{-3}\, s^{-1}]$

erg Erg, cgs unit of energy

F_c Conductive energy flux, $\left[erg\, cm^{-2}\, s^{-1}\right]$

K Kelvin, cgs unit of temperature

k_B Boltzmann constant, $1.3807 \times 10^{-16}\,[erg\,K^{-1}]$

$\kappa_{\|}$ Spitzer conductivity, parallel to the magnetic field, $10^{-6}T^{\frac{3}{2}}$

L_T Thermal characteristic scale length, $L_T \equiv \frac{T}{\bigtriangledown T} = \left(\frac{d\,lnT}{ds}\right)^{-1}\,[cm]$

L_n Density characteristic scale length, $L_n \equiv \frac{n}{\bigtriangledown n} = \left(\frac{d\,lnn}{ds}\right)^{-1}\,[cm]$

L_v Velocity characteristic scale length, $L_v \equiv \frac{v}{\bigtriangledown v} = \left(\frac{d\,lnv}{ds}\right)^{-1}\,[cm]$

P_H Power input to heating, $[erg\,s^{-1}]$

APPENDIX B

NUMERICAL METHODS

In numerical modeling there are often multiple ways to approach a problem. Each one has its advantages and disadvantages. Choosing between them is what makes numerical modeling an art as well as a science. This appendix explains some of the numerical techniques used in HYLOOP and the reasoning behind them.

Numerical Differencing

> "The calculus is the greatest aid we have to the appreciation of physical truth in the broadest sense of the word. "
>
> -William F. Osgood

Any numerical modeler will have to find ways of dealing with derivatives. Infinitesimal rates of change provide an excellent way for describing how the world works. Undergraduate students learn the basic definition of a derivative and then are inundated with the various rules and shorthands for using derivatives in various situations. A numerical treatment of derivatives immediately flows from these basic lessons. Firstly, an expression for the change of the function $f(x)$ is given by

$$f'(x) \approx \frac{f(x+\Delta x) - f(x)}{\Delta x}. \tag{2.1}$$

The above is an approximation to the derivative, which is denoted by a prime. It is the definition of the derivative in the limit of $\Delta x \to 0$. Computers have difficulty with such limits. The best that can be done with eq. 2.1 is to make Δx smaller and smaller until an acceptable precision is reached. At some point the limit is reached where the computer cannot distinguish between the value for Δx and zero, which yields an answer of infinity. The numerical difference operator, Δ, is defined which is simply the difference between the value of a function at the next point forward on a finite grid from the value at the current

point, i.e.

$$\Delta u = u_{i+1} - u_i. \tag{2.2}$$

So that if the grid step is defined by a step size of h so that $x_{N+1} = x_N + h$, the rate of change in f as a function of

$$\begin{aligned} \frac{\partial f}{\partial x} &\approx \frac{\Delta f}{\Delta x} \\ \frac{\Delta f}{\Delta x} &= \frac{f(x+h)-f(x)}{x+h-x}, \\ \frac{\Delta f}{\Delta x} &= \frac{f(x+h)-f(x)}{h} \end{aligned} \tag{2.3}$$

which looks just like equation 2.1 with Δx being replaced by the step size of the grid, h. The question now becomes, how good is this approximation?

Much of numerical modeling is based on Taylor's theorem which allows for the expression of a function in series expansion of its derivatives. The derivation of a Taylor series is left to math texts (See *Boas*, 1983; *Riley et al.*, 2002b, for texts that actually use words to describe the math) and the expansion of an unknown function $f(x+h)$ is written as

$$f(x+h) = f(x) + h f'(x) + \frac{1}{2}h^2 f''(x) + \frac{1}{6}h^3 f'''(x) + \mathscr{O}\left(\frac{1}{24}h^4 f^4\right), \tag{2.4}$$

where the primes and superscripts denote succeeding powers of differentiation with respect to x and $\mathscr{O}(\aleph)$ represents an infinite progression on the series with terms of order $\aleph$ and higher. Now equation 2.4 is rearranged to yield the following definition for the derivative,

$$f'(x) = \frac{f(x+h) - f(x)}{h} - \frac{1}{2}h f''(x) + \mathscr{O}\left(\frac{1}{6}h^3 f'''\right). \tag{2.5}$$

Now it is clear what terms are being ignored with equation 2.1. It is only *zero order accurate* which is to say that the terms of the step size, h, that have powers of one or greater are being neglected. This is a measurement of the truncation error, err_t. How does

the truncation error relate to the overall accuracy of the calculation? It is often difficult to determine the effect of truncation error without carrying out the calculation to the next term in the expansion and the truncation error strongly depends on the functions being evaluated. Often the programmer will not know the exact relation between the two and cannot even be guaranteed that high order accuracy will lead to better accuracy overall (*Press*, 2002)! However, the truncation error is one of the few elements that a programmer has full control over and measures should be taken to minimize it.

If the higher derivatives of a function are known or can be approximated the truncation error of eq. 2.5 can made arbitrarily low. Usually, this is not the case, especially when one is trying to find the function's first derivative. The order accuracy can be improved by Taylor expanding $f(x-h)$,

$$f(x-h) = f(x) + hf'(x) + \frac{1}{2}h^2 f''(x) + \frac{1}{6}h^3 f'''(x) + \mathcal{O}\left(h^4\right), \tag{2.6}$$

where from now on the order error is only expressed in terms of h. Now equation 2.4 is subtracted from equation 2.6 and rearranged to solve for $f'(x)$. This yields the *symmetric form* for the evaluation of the derivative written as

$$f'(x) = \frac{f(x+h) - f(x-h)}{h} - \mathcal{O}\left(h^2\right), \tag{2.7}$$

whose truncation error is $err_t \sim h^2 f'''$. The truncation error has been reduced at the price of another evaluation of f. Part of the art of numerical methods is determining if the addition accuracy is worth the extra effort required.

Explicit Methods

There are two broad strategies in the numerical integration of functions. The first is

by the use of explicit methods. Simply put, explicit methods determine some new value, y_{i+1}, explicitly in terms of the old value, y_i. Explicit methods are easier to implement and understand than their implicit cousins. However, the price paid for this ease of use is instability if the step sizes are too large or if the function has two drastically different scale sizes, i.e., if the equations are *stiff*. There is a wide range of explicit methods available but this discussion will be limited to the discussion of the few used within the HYLOOP codes.

Euler's Method

Euler's method is the simplest of the explicit solvers. It is derived directly from eq. 2.4 as expressed by

$$y_{n+1} = y_n + hy'(x_n, y_n), \tag{2.8}$$

where a change of notation by expressing $f(x)$ as y has been made. Also, the derivative of the function has been allowed to depend on both x and y, and the subscript has been used to represent a position on the grid of the independent variable, usually either space or time. Remembering Eq. (2.4) it is clear that this method is only first order accurate. This method is rarely used for most numerical work because there are many methods that are more accurate and more stable (*Press*, 2002). However, if the equations are not stiff and their characteristic scales are orders of magnitude larger than the step size then the speed of this method may make it of use.

The true limitation of Euler's method is that the slope of the function, y', is evaluated at the starting position and held constant for the entire step. While this might be a good approximation in a slowly varying function, it is usually true that taking multiple evaluations of a function's slope and then using them to progress along the step would improve the accuracy of the calculation. Methods to do just that are discussed below.

Runge-Kutta Methods

Runge-Kutta (RK) methods are the workhorse of the numerical modelers. RK methods take multiple Euler steps and use the higher order terms from Eq (2.4) and multiple evaluations of the function's slope to increase the accuracy to the desired order (*Press*, 2002). RK methods range from the basic to the advanced and it would require an entire textbook, or several, to describe them all. Here, the discussion is limited to the three forms found currently in HYLOOP (RK2, RK4, & RK5).

The simplest RK form is the second order Runge-Kutta (RK2) or the midpoint method. The RK2 method gains the extra order of accuracy by making a second evaluation of the derivative halfway through the step. The formula from *Press* (2002) is given as

$$\begin{aligned} k_1 &= hf'(x_n, y_n) \\ k_2 &= hf'\left(x_n + \tfrac{h}{2}, y_n + \tfrac{k_1}{2}\right). \\ y_{n+1} &= y_n + k_2 + \mathcal{O}\left(h^3\right) \end{aligned} \tag{2.9}$$

At the cost of one more evaluation of the function one can improve the accuracy by finding the slope of the function halfway through the step. The HYLOOP codes use a similar but slightly altered method to advance the state variables through the time step $\Delta_C t$. The modified midpoint method advances through a of series of sub-steps. This second order method was found to be more stable if the sub-steps were slightly larger than half of the total step, $0.6\Delta_C t$ to ensure the accuracy of the *upwind differencing scheme* used for advection terms (*Press*, 2002).

In PATC, tracking the evolution of the nonthermal particles requires a higher order scheme. This is due in large part to the fact that the mechanism that converts the particles' parallel momentum into perpendicular momentum, Eq. (2.65), does not explicitly conserve the test particle's magnetic moment. In order to preserve this adiabatic invariant, accuracy

is a must. A fifth order accurate scheme was chosen to get a higher accuracy at a reasonable step size. It was also used to calculate the particles' change in kinetic energy and parallel momentum due to collisions. Implementing an RK5 scheme is a two step process.

The first step is to implement a fourth order scheme (RK4) . RK4 is one of the most widely used numerical integration schemes in existence. It increases its accuracy by using the same general strategy as RK2 but using more evaluations of the derivative to estimate the slope. The steps for RK4 are given by *Press* (2002) as

$$\begin{aligned} k_1 &= hf'(x_n, y_n) \\ k_2 &= hf'\left(x_n + \tfrac{h}{2}, y_n + \tfrac{k_1}{2}\right) \\ k_3 &= hf'\left(x_n + \tfrac{h}{2}, y_n + \tfrac{k_2}{2}\right) \\ k_4 &= hf'(x_n + h, y_n + k_3) \\ y_{n+1} &= y_n + \tfrac{k_1 + 2k_2 + 2k_3 + k_4}{6} + \mathscr{O}\left(h^5\right) \end{aligned} \quad . \tag{2.10}$$

The second term on the right hand side is simply an average of the estimation of the slope times a step with the two interior evaluations, k_2 and k_3 given additional weight.

The second step in our RK5 scheme is to use the RK4 method to make two estimations of y_{n+1}. One estimation, δ_1, uses Eqs. (2.10) to estimate y_{n+1} by taking one step of size h. The second estimation, δ_2 uses two steps of size $\frac{h}{2}$ to reach y_{n+1}. The difference between the two estimations, $\Delta = \delta_2 - \delta_1$, gives a useful measure of the truncation error and can be used to make a fifth order accurate scheme as shown in *Press* (2002)

$$y_{n+1} = \delta_2 + \frac{\Delta}{15} + \mathscr{O}\left(h^6\right). \tag{2.11}$$

PATC conserved particles' magnetic moment$\sim$ 56% better when using an RK5 scheme rather than an RK4 scheme. It should be noted that often Δ is not used to increase the order accuracy of 2.10. Instead, it is used to adjust the step size h so that the error due to

truncation is kept below some threshold value, Δ_0. The usefulness of such an adaptive step size method will be evaluated for the next version of PATC.

Implicit Methods

As shown in Section 2 the time scales involved in conduction made use of an explicit time stepping scheme prohibitive, although other modelers have used them (*Bradshaw and Mason*, 2003). Since one of the aims of this work is to make a workable desktop code, it was decided to use implicit methods to handle equations with small time scales. This allows for the code to operate on relatively modest computer architectures and provides an example of a powerful, but sometimes mystifying, numerical tool to students who are new to numerical techniques.

Implicit schemes are notoriously difficult to implement (*Press*, 2002). Instead of describing a general method of employing an implicit differencing scheme a step-by-step derivation of the specific case involving the change in the distribution of energy due to conduction will be shown. The energy equation with conduction only

$$3n_e k_B \frac{\partial T}{\partial t} = \frac{1}{A}\frac{\partial}{\partial s}\left(A\kappa\frac{\partial T}{\partial s}\right), \tag{2.12}$$

where many of the simplifications of Eq. (2.32) have been skipped. Consider the second order differencing equation centered on the spatial grid point j, which is slightly modified from *Press* (2002) equation 5.1.6, and yields

$$\Delta^2 T_j = \left(T_{j+1} - T_j\right) - \left(T_j - T_{j-1}\right). \tag{2.13}$$

Now the neglected term within the parenthesis of Eq (2.12) must be inserted into the above equation. A pseudo diffusion coefficient is defined as $D \equiv A\kappa$. Note that the dimensionality

of this is different from a true diffusion coefficient by a factor of area. The dimensionality will be restored at the end of the derivation, where the differences in areas, A, on either side of a volume grid are taken into account. Since temperature is defined on the volume grid as defined on page ??, it makes sense to evaluate D on the surface grid point between the temperature volumes of each parenthesis term. This gives us

$$\Delta^2 T_j = D_{j+1/2}\left(T_{j+1} - T_j\right) - D_{j-1/2}\left(T_j - T_{j-1}\right), \tag{2.14}$$

where the subscript $j+1/2$ has been used to denote the surface grid between $j+1$ and j, and $j-1/2$ denotes the surface grid point between j and $j-1$.

Now the differencing of ∂s is applied in the denominator. To account for the non-uniform nature of the grid being used, the following definitions are made: $ds_{j+1/2} = s_{j+1} - s_j$ and $ds_{j-1/2} = s_j - s_{j-1}$. The s_js are defined on the volume grid, and $ds_j = s_{j+1/2} - s_{j-1/2}$. Now like terms are combined to yield,

$$3n_e k_B \frac{T_j^{n+1} - T_j^n}{\Delta t} = \frac{1}{A_j ds_j}\left(\frac{D_{j+1/2}\left(T_{j+1}^n - T_j^n\right)}{ds_{j+1/2}} - \frac{D_{j-1/2}\left(T_j^n - T_{j-1}^n\right)}{ds_{j-1/2}}\right), \tag{2.15}$$

where the left hand side has been differenced with respect to time with superscripts used to denote the position on the temporal grid. Quantities without superscripts are constant in time. Equation (2.15) is an example of a *forward time centered space* (FTCS) scheme for a parabolic equation with an analytically intractable D, which is certainly true in the case of conduction, as described by *Press* (2002) equation 19.2.19 with modifications made for a non-uniform grid.

The stability criterion for Eq. (2.15) is given by

$$\Delta t \leq \frac{(\Delta s)^2}{2D}, \tag{2.16}$$

or roughly half of the conductive cooling time (*Press*, 2002). Given reasonable flare parameters it was determined that conductive cooling time was orders of magnitude too small for an explicit time step (see on page 37). Fortunately, Eq. (2.15) can be made stable for any time step at the loss of some accuracy. Stability is achieved by evaluating the right hand side at the future time step $n+1$. Evaluation of the right hand side at a future time will make Eq (2.15) a *backward time* or *implicit scheme*. To recast Eq. (2.15) as an implicit equation the following definitions are made,

$$\begin{aligned} \alpha &= \frac{\Delta t}{A_J ds_j} \\ \beta_{+1/2} &= \frac{D_{j+1/2}}{ds_{j+1/2}} \\ \beta_{-1/2} &= \frac{D_{j-1/2}}{ds_{j-1/2}} \end{aligned} . \tag{2.17}$$

All of the n's on the right hand side of Eq. (2.15) are replaced with $n+1$, the equation is rearranged to put the sole T_j^n term by itself. Grouping terms of like subscript gives the following expression,

$$\begin{aligned} 3n_e k_B T_j^n = & -\alpha\beta_{+1/2} T_{j+1}^{n+1} \\ & + T_j^{n+1}\left(-\alpha\beta_{+1/2} + \alpha\beta_{-1/2} + 3n_e k_B\right) \\ & - \alpha\beta_{-1/2} T_{j-1}^{n+1} \end{aligned} . \tag{2.18}$$

Equation (2.18) can be described as a matrix operation of the following form

$$3n_e k_B \overrightarrow{T^n} = \overleftrightarrow{M} \cdot \overrightarrow{T^{n+1}}. \tag{2.19}$$

$\overleftrightarrow{M}$ is a tridiagonal matrix with the first term of Eq. (2.18) providing the *super-diagonal* elements, the second term providing the *diagonal* elements and the last term providing the *sub-diagonal* terms. *Dirichlet* boundary conditions are set on the volume grids holding the temperature of the first and last grid at a constant temperature, T_{min}, for all time, and

Neumann boundary conditions on the surface grid setting the conductive flux on the first and last surface grid to zero.

The last step in advancing the conduction equation forward is to find the inverse of the matrix, $\mathbf{M}^{-1}$, and use it to advance the current temperature state to the future one. This is accomplished using the IDL™ routine *trisol.pro* which is based on the *tridag* algorithm provided by *Press* (2002). This routine is useful since it does not require the full matrix $\mathbf{M}$, most of which is filled with zeroes. Instead, it only requires three vectors that represent the *super-diagonal* , *diagonal* and *sub-diagonal* elements.

During this derivation it has been assumed that the pseudo-diffusion coefficient, D, is constant over the time step. This is not the case. The coefficient contains the term κ which was shown on page 37 to have a $T^{5/2}$ dependence. The saturated flux conditions make the dependence on T even more complicated and analytically intractable. Future versions of HYLOOP will take this non-linear character into account and record its effects on the simulation's evolution.

REFERENCES

Acton, L. W., et al., The morphology of 20 X 10 exp 6 K plasma in large non-impulsive solar flares, *44*, L71–L75, 1992.

Alexander, D., and T. R. Metcalf, A Spectral Analysis of the Masuda Flare Using YOHKOH Hard X-Ray Telescope Pixon Reconstruction, *ApJ*, *489*, 442–+, doi:10.1086/304762, 1997.

Allred, J. C., S. L. Hawley, W. P. Abbett, and M. Carlsson, Radiative Hydrodynamic Models of the Optical and Ultraviolet Emission from Solar Flares, *ApJ*, *630*, 573–586, doi:10.1086/431751, 2005.

Antiochos, S. K., P. J. MacNeice, D. S. Spicer, and J. A. Klimchuk, The Dynamic Formation of Prominence Condensations, *ApJ*, *512*, 985–991, doi:10.1086/306804, 1999.

Arfken, G. B., and H. J. Weber, *Mathematical methods for physicists*, Cambridge University Press, 1995.

Aschwanden, M. J., Electron versus Proton Timing Delays in Solar Flares, *ApJ*, *470*, L69+, doi:10.1086/310294, 1996.

Aschwanden, M. J., *Physics of the Solar Corona. An Introduction with Problems and Solutions (2nd edition)*, Praxis Publishing Ltd, 2005.

Aschwanden, M. J., and C. J. Schrijver, Analytical Approximations to Hydrostatic Solutions and Scaling Laws of Coronal Loops, *ApJS*, *142*, 269–283, doi:10.1086/341945, 2002.

Aurass, H., G. Mann, G. Rausche, and A. Warmuth, The GLE on Oct. 28, 2003 - radio diagnostics of relativistic electron and proton injection, *A&A*, *457*, 681–692, doi:10.1051/0004-6361:20065238, 2006.

Bai, T., Transport of energetic electrons in a fully ionized hydrogen plasma, *ApJ*, *259*, 341–349, 1982.

Bai, T., and B. Dennis, Characteristics of gamma-ray line flares, *ApJ*, *292*, 699–715, doi:10.1086/163202, 1985.

Belleman, R. G., J. Bédorf, and S. F. Portegies Zwart, High performance direct gravitational N-body simulations on graphics processing units II: An implementation in CUDA, *New Astronomy*, *13*, 103–112, doi:10.1016/j.newast.2007.07.004, 2008.

Benz, A. O., *Plasma astrophysics: Kinetic processes in solar and stellar coronae*, Astrophysics and Space Science Library, vol. 184, Dordrecht: Kluwer, |c1993, 1993a.

Benz, A. O., *Plasma astrophysics: Kinetic processes in solar and stellar coronae*, Astrophysics and Space Science Library, vol. 184, Dordrecht: Kluwer, |c1993, 1993b.

Benz, A. O., Flare observations, *Living Reviews in Solar Physics*, *5*(1), 2008.

Benz, A. O., and P. Saint-Hilaire, Solar flare electron acceleration: Comparing theories and observations, *Advances in Space Research*, *32*, 2415–2423, doi:10.1016/j.asr.2003.01.002, 2003.

Boas, M. L., *Mathematical Methods in the Physical Sciences*, John Wiley and Sons, Inc., 1983.

Bradshaw, S. J., and H. E. Mason, A self-consistent treatment of radiation in coronal loop modelling, *A&A*, *401*, 699–709, doi:10.1051/0004-6361:20030089, 2003.

Brown, J. C., The Deduction of Energy Spectra of Non-Thermal Electrons in Flares from the Observed Dynamic Spectra of Hard X-Ray Bursts, *Solar Phys.*, *18*, 489–502, doi:10.1007/BF00149070, 1971.

Brown, J. C., E. P. Kontar, and A. M. Veronig, RHESSI Results – Time For a Rethink?, *ArXiv Astrophysics e-prints*, 2006.

Brown, J. C., E. P. Kontar, and A. M. Veronig, RHESSI Results Time for a Rethink?, in *Lecture Notes in Physics, Berlin Springer Verlag*, *Lecture Notes in Physics, Berlin Springer Verlag*, vol. 725, edited by K.-L. Klein and A. L. MacKinnon, pp. 65–+, 2007.

Brown, M. R., C. D. Cothran, M. Landreman, D. Schlossberg, and W. H. Matthaeus, Experimental Observation of Energetic Ions Accelerated by Three-dimensional Magnetic Reconnection in a Laboratory Plasma, *ApJL*, *577*, L63–L66, 2002.

Bungey, T. N., and E. R. Priest, Current sheet configurations in potential and force-free fields., *A&A*, *293*, 215–224, 1995.

Cheng, C.-C., Evolution of the high-temperature plasma in the 15 June 1973 flare, *Solar Phys.*, *55*, 413–429, 1977.

Choudhuri, A. R. (Ed.), *The physics of fluids and plasmas : an introduction for astrophysicists /*, 1998.

Cohen, R. S., L. Spitzer, and P. M. Routly, The Electrical Conductivity of an Ionized Gas, *Physical Review*, *80*, 230–238, doi:10.1103/PhysRev.80.230, 1950.

Dere, K. P., E. Landi, H. E. Mason, B. C. Monsignori Fossi, and P. R. Young, CHIANTI - an atomic database for emission lines, *A&A*, *125*, 149–173, 1997.

Des Jardins, A. C., R. Canfield, D. W. Longcope, and E. McLinden, Signatures of Magnetic Stress Prior to Three Solar Flares Observed by RHESSI, in preparation, 2008.

Dmitruk, P., and D. O. Gómez, Scaling Law for the Heating of Solar Coronal Loops, *ApJ*, *527*, L63–L66, doi:10.1086/312390, 1999.

Dreher, J., and R. Grauer, A Parallel Mesh-Adaptive Framework for Hyperbolic Conservation Laws, *ArXiv Physics e-prints*, 2006.

Emslie, A. G., The collisional interaction of a beam of charged particles with a hydrogen target of arbitrary ionization level, *ApJ*, *224*, 241–246, 1978.

Feldman, U., and K. G. Widing, Elemental Abundances in the Solar Upper Atmosphere Derived by Spectroscopic Means, *Space Science Reviews*, *107*, 665–720, doi:10.1023/A:1026103726147, 2003.

Fermi, E., On the Origin of the Cosmic Radiation, *Physical sReview*, *75*, 1169–1174, doi:10.1103/PhysRev.75.1169, 1949.

Fisher, G. H., R. C. Canfield, and A. N. McClymont, Flare loop radiative hydrodynamics. V - Response to thick-target heating. VI - Chromospheric evaporation due to heating by nonthermal electrons. VII - Dynamics of the thick-target heated chromosphere, *ApJ*, *289*, 414–441, doi:10.1086/162901, 1985a.

Fisher, G. H., R. C. Canfield, and A. N. McClymont, Flare Loop Radiative Hydrodynamics - Part Six - Chromospheric Evaporation due to Heating by Nonthermal Electrons, *ApJ*, *289*, 425–+, doi:10.1086/162902, 1985b.

Fisher, G. H., R. C. Canfield, and A. N. McClymont, Flare Loop Radiative Hydrodynamics - Part Seven - Dynamics of the Thick Target Heated Chromosphere, *ApJ*, *289*, 434–+, doi:10.1086/162903, 1985c.

Fletcher, L., and H. S. Hudson, Impulsive phase flare energy transport by large-scale Alfven waves and the electron acceleration problem, *ArXiv e-prints*, *712*, 2007.

Fletcher, L., and H. S. Hudson, Impulsive Phase Flare Energy Transport by Large-Scale Alfvén Waves and the Electron Acceleration Problem, *ApJ*, *675*, 1645–1655, doi:10.1086/527044, 2008.

Fletcher, L., and P. C. H. Martens, A Model for Hard X-Ray Emission from the Top of Flaring Loops, *ApJ*, *505*, 418–431, 1998a.

Fletcher, L., and P. C. H. Martens, A Model for Hard X-Ray Emission from the Top of Flaring Loops, *ApJ*, *505*, 418–431, 1998b.

Fletcher, L., and P. Petkaki, Particle Acceleration and Transport in Reconnecting Plasmas, *Solar Phys.*, *172*, 267–270, 1997.

Fletcher, L., I. G. Hannah, H. S. Hudson, and T. R. Metcalf, A TRACE White Light and RHESSI Hard X-Ray Study of Flare Energetics, *ApJ*, *656*, 1187–1196, doi:10.1086/510446, 2007a.

Fletcher, L., I. G. Hannah, H. S. Hudson, and T. R. Metcalf, A TRACE White Light and RHESSI Hard X-Ray Study of Flare Energetics, *ApJ*, *656*, 1187–1196, doi:10.1086/510446, 2007b.

Fontenla, J. M., E. H. Avrett, and R. Loeser, Energy balance in the solar transition region. I - Hydrostatic thermal models with ambipolar diffusion, *ApJ*, *355*, 700–718, doi:10.1086/168803, 1990.

Fontenla, J. M., E. H. Avrett, and R. Loeser, Energy balance in the solar transition region. II - Effects of pressure and energy input on hydrostatic models, *ApJ*, *377*, 712–725, doi:10.1086/170399, 1991.

Golub, L., et al., The X-Ray Telescope (XRT) for the Hinode Mission, *Solar Phys.*, *243*, 63–86, doi:10.1007/s11207-007-0182-1, 2007.

Green, R. M., Modes of annihilation and reconnection of magnetic fields, in *Stellar and Solar Magnetic Fields*, *IAU Symposium*, vol. 22, edited by R. Lust, pp. 398–+, 1965.

Grigis, P. C., and A. O. Benz, The spectral evolution of impulsive solar X-ray flares, *A&A*, *426*, 1093–1101, doi:10.1051/0004-6361:20041367, 2004.

Hamilton, B., K. G. McClements, L. Fletcher, and A. Thyagaraja, Field-Guided Proton Acceleration at Reconnecting x-Points in Flares, *Solar Phys.*, *214*, 339–352, 2003.

Hamilton, B., L. Fletcher, K. G. McClements, and A. Thyagaraja, Electron Acceleration at Reconnecting X-Points in Solar Flares, *ApJ*, *625*, 496–505, doi:10.1086/430100, 2005.

Hannah, I. G., and L. Fletcher, Comparison of the Energy Spectra and Number Fluxes From a simple Flare Model to Observations, *Solar Phys.*, *236*, 59–74, doi:10.1007/s11207-006-0139-9, 2006.

Harrison, R. A., et al., The Coronal Diagnostic Spectrometer for the Solar and Heliospheric Observatory, *Solar Phys.*, *162*, 233–290, doi:10.1007/BF00733431, 1995.

Haug, E., On the use of nonrelativistic bremsstrahlung cross sections in astrophysics., *A&A*, *326*, 417–418, 1997.

Heerikhuisen, J., Y. E. Litvinenko, and I. J. D. Craig, Proton Acceleration in Analytic Reconnecting Current Sheets, *ApJ*, *566*, 512–520, doi:10.1086/337957, 2002.

Hilts, P. J., Sunspots may hit 200-year peak, *The Washington Post*, (27), A04, 1988.

Holman, G. D., Acceleration of runaway electrons and Joule heating in solar flares, *ApJ*, *293*, 584–594, doi:10.1086/163263, 1985.

Hudson, H., and J. Ryan, High-Energy Particles In Solar Flares, *33*, 239–282, doi:10.1146/annurev.aa.33.090195.001323, 1995.

Ivlev, A. V., V. E. Fortov, and B. A. Klumov, Collision of Comet Shoemaker-Levy 9 with Jupiter: interpretation of optical observations., *Soviet Journal of Experimental and Theoretical Physics Letters*, *61*, 431–437, 1995.

Jefferies, J. T., F. Q. Orrall, and J. B. Zirker, The Interpretation of Total Line Intensities from Optically Thin Gases. I: A General Method, *Solar Phys.*, *22*, 307–316, doi:10.1007/BF00148698, 1972.

Kankelborg, C., and D. Longcope, Forward modeling of the coronal response to reconnection in an X-ray bright point, *Solar Phys.*, *190*, 59–77, doi:10.1023/A:1005205807984, 1999.

Kašparová, J., M. Karlický, E. P. Kontar, R. A. Schwartz, and B. R. Dennis, Multi-Wavelength Analysis of High-Energy Electrons in Solar Flares: A Case Study of the August 20, 2002 Flare, *Solar Phys.*, *232*, 63–86, doi:10.1007/s11207-005-1581-9, 2005.

khattri, s. k., Grid Generation and Adaptation by Functionals, *ArXiv Mathematics e-prints*, 2006.

Kivelson, M. G., and C. T. Russell, *Introduction to Space Physics*, Introduction to Space Physics, Edited by Margaret G. Kivelson and Christopher T. Russell, pp. 586. ISBN 0521451043. Cambridge, UK: Cambridge University Press, April 1995., 1995.

Klimchuk, J. A., On Solving the Coronal Heating Problem, *Solar Phys.*, *234*, 41–77, doi:10.1007/s11207-006-0055-z, 2006.

Klimchuk, J. A., S. Patsourakos, and P. J. Cargill, Highly Efficient Modeling of Dynamic Coronal Loops, *ArXiv e-prints*, *710*, 2007.

Kontar, E. P., A. L. MacKinnon, R. A. Schwartz, and J. C. Brown, Compton backscattered and primary X-rays from solar flares: angle dependent Green's function correction for photospheric albedo, *A&A*, *446*, 1157–1163, doi:10.1051/0004-6361:20053672, 2006.

Kosugi, T., et al., The hard X-ray telescope (HXT) for the Solar-A mission, *Solar Phys.*, *136*, 17–36, 1991.

Krauth, W., Introduction To Monte Carlo Algorithms, *ArXiv Condensed Matter e-prints*, 1996.

Laming, J. M., A Unified Picture of the First Ionization Potential and Inverse First Ionization Potential Effects, *ApJ*, *614*, 1063–1072, doi:10.1086/423780, 2004.

Landi, E., and M. Landini, Radiative losses of optically thin coronal plasmas, *A&A*, *347*, 401–408, 1999.

Landi, E., and K. J. H. Phillips, CHIANTI-An Atomic Database for Emission Lines. VIII. Comparison with Solar Flare Spectra from the Solar Maximum Mission Flat Crystal Spectrometer, *ApJS*, *166*, 421–440, doi:10.1086/506180, 2006.

Leach, J., and V. Petrosian, Impulsive phase of solar flares. I - Characteristics of high energy electrons, *ApJ*, *251*, 781–791, doi:10.1086/159521, 1981.

Li, C., Y. H. Tang, Y. Dai, C. Fang, and J.-C. Vial, Flare magnetic reconnection and relativistic particles in the 2003 October 28 event, *A&A*, *472*, 283–286, doi:10.1051/0004-6361:20066966, 2007.

Li, P., A. G. Emslie, and J. T. Mariska, Soft X-ray diagnostics of electron-heated solar flare atmospheres, *ApJ*, *341*, 1075–1081, doi:10.1086/167565, 1989.

Lifshitz, E. M., and L. P. Pitaevskii, *Physical kinetics*, Course of theoretical physics, Oxford: Pergamon Press, 1981, 1981.

Lin, R. P., et al., The Reuven Ramaty High-Energy Solar Spectroscopic Imager (RHESSI), *Solar Phys.*, *210*, 3–32, doi:10.1023/A:1022428818870, 2002.

Lin, R. P., et al., RHESSI Observations of Particle Acceleration and Energy Release in an Intense Solar Gamma-Ray Line Flare, *ApJ*, *595*, L69–L76, doi:10.1086/378932, 2003.

Litvinenko, Y. E., Particle Acceleration in Reconnecting Current Sheets with a Nonzero Magnetic Field, *ApJ*, *462*, 997–+, doi:10.1086/177213, 1996.

Liu, W., Characteristics of Solar Flare Hard X-ray Emissions: Observations and Models, Ph.D. thesis, Stanford University, 2006.

Liu, W., *Solar Flares as Natural Particle Accelerators: A High-energy View from X-ray Observations and Theoretical Models*, Monograph published by VDM Verlag Dr. Müller, Saarbrücken, Germany; ISBN: 978-3-8364-7432-0, 10 chapters, 252 pages, 2008.

MacKinnon, A. L., and I. J. D. Craig, Stochastic simulation of fast particle diffusive transport, *A&A*, *251*, 693–699, 1991.

Mariska, J. T., A. G. Emslie, and P. Li, Numerical simulations of impulsively heated solar flares, *ApJ*, *341*, 1067–1074, doi:10.1086/167564, 1989.

Martens, P. C. H., The generation of proton beams in two-ribbon flares, *ApJ*, *330*, L131–L133, doi:10.1086/185220, 1988.

Martens, P. C. H., A Surprising New Take on Scaling Laws, in preparation, 2008.

Martens, P. C. H., and N. P. M. Kuin, A circuit model for filament eruptions and two-ribbon flares, *SOLPHYS*, *122*, 263–302, 1989.

Martens, P. C. H., C. C. Kankelborg, and T. E. Berger, On the Nature of the "Moss" Observed by TRACE, *ApJ*, *537*, 471–480, doi:10.1086/309000, 2000.

Masuda, S., T. Kosugi, H. Hara, S. Tsuneta, and Y. Ogawara, A Loop-Top Hard X-Ray Source in a Compact Solar Flare as Evidence for Magnetic Reconnection, *Nature*, *371*, 495–+, doi:10.1038/371495a0, 1994.

Matte, J. P., and J. Virmont, Electron heat transport down steep temperature gradients, *Physical Review Letters*, *49*, 1936–1939, 1982.

McClements, K. G., and D. Alexander, Fokker-Planck Modeling of Asymmetric Footpoint Hard X-Ray Emission in Solar Flares, *ApJ*, *619*, 1153–1159, doi:10.1086/426581, 2005.

McClymont, A. N., and R. C. Canfield, Flare loop radiative hydrodynamics. I - Basic methods, *ApJ*, *265*, 483–506, doi:10.1086/160692, 1983.

McMullen, R. A., State of The Loop Model, A Report to the MSU Solar Physics Group, 2002.

Melrose, D. B., Resonant scattering of particles and second phase acceleration in the solar corona, *Solar Phys.*, *37*, 353–365, 1974.

Meyer, J.-P., Solar-stellar outer atmospheres and energetic particles, and galactic cosmic rays, *ApJS*, *57*, 173–204, doi:10.1086/191001, 1985.

Miller, J. A., Electron Acceleration in Solar Flares by Fast Mode Waves: Quasi-linear Theory and Pitch-Angle Scattering, *ApJ*, *491*, 939–+, doi:10.1086/305004, 1997.

Miller, J. A., and J. T. Mariska, Stochastic Particle Acceleration in a Self-Consistent Solar Flare Atmosphere, *AGU Spring Meeting Abstracts*, pp. C2+, 2005.

Miller, J. A., and R. Ramaty, Ion and relativistic electron acceleration by Alfven and whistler turbulence in solar flares, *Solar Phys.*, *113*, 195–200, 1987.

Milligan, R. O., P. T. Gallagher, M. Mathioudakis, D. S. Bloomfield, F. P. Keenan, and R. A. Schwartz, RHESSI and SOHO CDS Observations of Explosive Chromospheric Evaporation, *ApJL*, *638*, L117–L120, doi:10.1086/500555, 2006a.

Milligan, R. O., P. T. Gallagher, M. Mathioudakis, and F. P. Keenan, Observational Evidence of Gentle Chromospheric Evaporation during the Impulsive Phase of a Solar Flare, *ApJL*, *642*, L169–L171, doi:10.1086/504592, 2006b.

Morton, K. W., and D. F. Mayers, *Numerical Solution of Partial Differential Equations*, Cambridge University Press, 1994.

Mulu-Moore, F., A. Winebarger, and H. Warren, Benchmarking 1D Hydrodynamic Codes for Steady State Solutions, *AGU Fall Meeting Abstracts*, pp. A1097+, 2007.

Murthy, K. P. N., Monte Carlo: Basics, *ArXiv Condensed Matter e-prints*, 2001a.

Murthy, K. P. N., Monte Carlo: Basics, *ArXiv Condensed Matter e-prints*, 2001b.

Nitta, N. V., J. Sato, and H. S. Hudson, The Physical Nature of the Loop-Top X-Ray Sources in the Gradual Phase of Solar Flares, *ApJ*, *552*, 821–832, doi:10.1086/320547, 2001.

Odenwald, S., Solar storms, *The Washington Post*, (10), H01, 1999.

Ogawara, Y., T. Takano, T. Kato, T. Kosugi, S. Tsuneta, T. Watanabe, I. Kondo, and Y. Uchida, The Solar-A Mission - an Overview, *Solar Phys.*, *136*, 1–16, doi:10.1007/BF00151692, 1991.

Orwig, L. E., K. J. Frost, and B. R. Dennis, The hard X-ray burst spectrometer on the Solar Maximum Mission, *Solar Phys.*, *65*, 25–37, 1980.

Park, B. T., and V. Petrosian, Fokker-Planck Equations of Stochastic Acceleration: A Study of Numerical Methods, *ApJS*, *103*, 255–+, 1996.

Parks, G. K., *Physics of space plasmas : an introduction*, Physics of space plasmas : an introduction / George K Parks. Boulder, Colo. : Westview Press, Advanced Book Program, c2004., 2004.

Peres, G., and F. Reale, The importance of plasma viscosity on X-ray line diagnostics of solar flares, *A&A*, *267*, 566–576, 1993.

Petrosian, V., Impulsive Solar X-Ray Bursts: Bremsstrahlung Radiation from a Beam of Electrons in the Solar Chromosphere and the Total Energy of Solar Flares, *ApJ*, *186*, 291–304, 1973.

Phillips, K. J. H., *Guide to the Sun*, Guide to the Sun, by Kenneth J. H. Phillips, pp. 400. ISBN 052139788X. Cambridge, UK: Cambridge University Press, March 1995., 1995.

Press, W. H., *Numerical recipes in C++ : the art of scientific computing*, Numerical recipes in C++ : the art of scientific computing by William H. Press. xxviii, 1,002 p. : ill. ; 26 cm. Includes bibliographical references and index. ISBN : 0521750334, 2002.

Priest, E., and T. Forbes, *Magnetic Reconnection*, Magnetic Reconnection, by Eric Priest and Terry Forbes, pp. 612. ISBN 0521481791. Cambridge, UK: Cambridge University Press, June 2000., 2000a.

Priest, E., and T. Forbes, *Magnetic Reconnection*, Magnetic Reconnection, by Eric Priest and Terry Forbes, pp. 612. ISBN 0521481791. Cambridge, UK: Cambridge University Press, June 2000., 2000b.

Ramaty, R., N. Mandzhavidze, B. Kozlovsky, and R. J. Murphy, Solar Atmopheric Abundances and Energy Content in Flare Accelerated Ions from Gamma-Ray Spectroscopy, *ApJ*, *455*, L193+, doi:10.1086/309841, 1995.

Reeves, K. K., H. P. Warren, and T. G. Forbes, Theoretical Predictions of X-Ray and Extreme-UV Flare Emissions Using a Loss-of-Equilibrium Model of Solar Eruptions, *ApJ*, *668*, 1210–1220, doi:10.1086/521291, 2007.

Riley, K., M. Hobson, and S. Bence, *Mathematical Methods for Physics and Engineering: A Comprehensive Guide*, Cambridge University Press, 2002a.

Riley, K., M. Hobson, and S. Bence, *Mathematical Methods for Physics and Engineering: A Comprehensive Guide*, Cambridge University Press, 2002b.

Ripley, B. D., *Stochastic Simulation*, New York: Wiley and Sons, 1987.

Rosner, R., W. H. Tucker, and G. S. Vaiana, Dynamics of the quiescent solar corona, *ApJ*, *220*, 643–645, doi:10.1086/155949, 1978.

Rosner, R., B. C. Low, and T. E. Holzer, Physical processes in the solar corona, in *Physics of the Sun. Volume 2*, vol. 2, pp. 135–180, 1986.

Rybicki, G. B., and A. P. Lightman, *Radiative Processes in Astrophysics*, Radiative Processes in Astrophysics, by George B. Rybicki, Alan P. Lightman, pp. 400. ISBN 0-471-82759-2. Wiley-VCH , June 1986., 1986.

Shih, A. Y., H. S. Hudson, D. M. Smith, and R. P. Lin, Investigation of Ion Acceleration in Small RHESSI Flares, *AGU Fall Meeting Abstracts*, pp. C1+, 2007.

Simnett, G. M., A dominant role for protons at the onset of solar flares, *Solar Phys.*, *106*, 165–183, 1986.

Spitzer, L., and R. Härm, Transport Phenomena in a Completely Ionized Gas, *Physical Review*, *89*, 977–981, doi:10.1103/PhysRev.89.977, 1953.

Strong, K. T., J. L. R. Saba, B. M. Haisch, and J. T. Schmelz (Eds.), *The many faces of the sun : a summary of the results from NASA's Solar Maximum Mission*, 1999.

Sturrock, P. A., *Plasma Physics*, Plasma Physics, 1994.

Sublette, C., The nuclear weapon archive: A guide to nuclear weapons, World Wide Web electronic publication, 2007.

Sui, L., G. D. Holman, and B. R. Dennis, Determination of Low-Energy Cutoffs and Total Energy of Nonthermal Electrons in a Solar Flare on 2002 April 15, *ApJ*, *626*, 1102–1109, doi:10.1086/430086, 2005a.

Sui, L., G. D. Holman, S. M. White, and J. Zhang, Multiwavelength Analysis of a Solar Flare on 2002 April 15, *ApJ*, *633*, 1175–1186, doi:10.1086/462410, 2005b.

Sui, L., G. D. Holman, and B. R. Dennis, Motion of 3-6 keV Nonthermal Sources along the Legs of a Flare Loop, *ApJ*, *645*, L157–L160, doi:10.1086/506325, 2006.

Syrovatskii, S., Formation of current sheets in a plasma with frozen-in strong magnetic field, *Sov. Phys. JETP*, *33*(5), 933–940, 1971.

Tanaka, K., Impact of X-ray observations from the Hinitori satellite on solar flare research, *39*, 1–45, 1987.

Tanaka, Y., Introduction to HINOTORI, *Solar Phys.*, *86*, 3–6, 1983.

Tandberg-Hanssen, E., and A. G. Emslie, *The physics of solar flares*, Cambridge and New York, Cambridge University Press, 1988, 286 p., 1988.

Thompson, A., and B. N. Taylor, The nist guide for the use of the international system of units, World Wide Web electronic publication, 2008.

Thornton, S. T., and J. B. Marion, *Classical Dynamics of Particles and Systems*, Brooks Cole, 1995.

Tsuneta, S., et al., The soft X-ray telescope for the SOLAR-A mission, *Solar Phys.*, *136*, 37–67, 1991.

Veronig, A., B. Vršnak, B. R. Dennis, M. Temmer, A. Hanslmeier, and J. Magdalenić, The Neupert effect and the electron-beam-driven evaporation model, in *Solar Variability: From Core to Outer Frontiers*, *ESA Special Publication*, vol. 506, edited by J. Kuijpers, pp. 367–370, 2002a.

Veronig, A., B. Vršnak, M. Temmer, and A. Hanslmeier, Relative timing of solar flares observed at different wavelengths, *Solar Phys.*, *208*, 297–315, 2002b.

Weisstein, E. W., Uniform distribution, 2009.

White, S. M., R. J. Thomas, J. W. Brosius, and M. R. Kundu, The Absolute Abundance of Iron in the Solar Corona, *ApJ*, *534*, L203–L206, doi:10.1086/312673, 2000.

Wood, P., and T. Neukirch, Electron Acceleration in Reconnecting Current Sheets, *Solar Phys.*, *226*, 73–95, doi:10.1007/s11207-005-5686-y, 2005.

Yokoyama, T., H. Nakajima, K. Shibasaki, V. F. Melnikov, and A. V. Stepanov, Microwave Observations of the Rapid Propagation of Nonthermal Sources in a Solar Flare by the Nobeyama Radioheliograph, *ApJ*, *576*, L87–L90, doi:10.1086/343098, 2002.

Zirker, J. B., *Journey from the center of the sun*, Journal of Cluster Science, 2002.